A DUST FLOW SEPARATOR TYPE ELECTROSTATIC PRECIPITATOR FOR DIESEL ENGINE PARTICULATE MATTER CONTROL

A DUST FLOW SEPARATOR TYPE ELECTROSTATIC PRECIPITATOR FOR DIESEL ENGINE PARTICULATE MATTER CONTROL

By

JOHN W. COLENBRANDER

A Thesis

Submitted to the School of Graduate Studies

in Partial Fulfillment of the requirements

for the Degree of

Master of Applied Science

McMaster University

Hamilton, Ontario

Master of Applied Science   McMaster University

                                   Hamilton, Ontario

TITLE: A dust flow separator type electrostatic precipitator for
diesel engine particulate matter control

AUTHOR: John W. Colenbrander, B.Eng & Soc.

SUPERVISOR: Drs. C. Y. Ching, D. Ewing

NUMBER OF PAGES: 133 pages (i-xiii, 1-120)

ABSTRACT

Increasingly stringent legislation governing the emissions of diesel engine particulate matter (DPM) has required the development of technological improvements to diesel engines, fuels and exhaust treatments. A main focus of diesel particulate matter abatement is on exhaust aftertreatment, that consists of the removal of particulate matter from the exhaust gas after it exits the engine. This is currently accomplished with regenerative diesel particulate traps that are effective at removing DPM, but are costly and introduce a significant pressure drop in the exhaust flow.

The objective of this study was to evaluate the potential of a novel particulate removal system consisting of a particulate flow separator combined with electrostatic precipitators (ESPs). Previous application of this system to natural gas emissions resulted in collection efficiencies larger than 90% with negligible pressure drop.

The ESPs used in the proposed flow separator-ESP were characterized and have collection efficiencies of up to 99% at the flow rates studied. The flow separator-ESP was characterized with a straight inlet section and an expanding inlet section. The collection efficiency of the flow separator-ESP configured with the expanding inlet section was up to 60% for a flow rate of 2.5 kg/hr, that corresponded to laminar flow with Reynolds number of 1100. Collection efficiencies on the order of 20% were obtained for exhaust flow rates of 3.75 kg/hr (Re = 1500) and 5.0 kg/hr (Re = 2100) for both inlet configurations, and 2.5 kg/hr with the straight inlet. The effectiveness of the current design is limited by exhaust flow rate.

The diesel exhaust gas was sampled using a partial flow dilution tunnel developed specifically for this study. The dilution ratio for this system can be estimated to within ±10% using volumetric flow measurements. It was found that changes in the

dilution and sampling velocity ratios for diesel exhaust have some effect on measured particulate matter mass concentrations.

To my Father and Mother.

ACKNOWLEDGMENTS

CONTENTS

LIST OF TABLES

LIST OF FIGURES

xi

CHAPTER 1

INTRODUCTION

Particulate matter (PM) is generally considered to be a suspension of small (5 nm - 100 μm in diameter) solid or liquid particles in air. The term particulate matter is often used interchangeably with terms such as particles or aerosols. Particulate matter has a multitude of sources, both natural (forest fires, wind erosion) and anthropogenic (machining operations such as grinding, combustion), outlined in Table 1.1. The formation of particles, particularly from anthropogenic sources, can be classified as primary or secondary. Primary particles are emitted directly to the atmosphere, while secondary particles are formed in the atmosphere as a result of chemical reactions between different precursor gases, including N_2, O_2, NO_x, CO, SO_x, hydrocarbons, VOCs and NH_3.

The typical size distribution of particulate matter from different sources is shown in Figure 1.1. Particulate matter can be classified in a variety of ways. One common classification is based on its ability to enter the body. Coarse particulate matter with

1

		Primary Particles	Secondary Particles
Natural Sources	Coarse	Windblown soil Volcanic dust Sea salt spray Pollen	
	Fine	Forest fire ash	Chemicals released by vegetation
Anthropogenic Sources	Coarse	Farmland Roads Construction sites Machining operations	
	Fine	Combustion of fossil fuels in electrical power plants, motor vehicles, heating systems, industrial boilers, etc.	Reactions of precursor gases (NO_x, SO_2, VOCs, NH_3, etc.)

Table 1.1: Some natural and anthropogenic sources of primary and secondary particles. *Adapted from Environment Canada (2001a).*

aerodynamic diameter larger than 10 μm does not tend to enter the lungs because of filtration in the nasal passages. Inhalable particulate matter with aerodynamic diameter less than 10 μm enters the lungs. This fraction is termed PM_{10}. The fraction of particulate matter with aerodynamic diameter less than 2.5 μm, often referred to as fine particulate matter, is of greatest concern to health professionals because it can be transferred to the deepest areas of the lung, causing health problems.

The particulate matter in the atmosphere has a number of adverse effects. In particular, particulate matter is known to have adverse health effects and is thought to be responsible for respiratory problems such as asthma, bronchitis, shortness of breath, and painful breathing, leading to hospitalization and premature deaths (HAQI, 1997). Particulate matter also contains carcinogens. The severity of exposure to PM was reported in the Hamilton-Wentworth Air Quality Initiative report (HAQI, 1997), that argued that PM_{10} and sulphates are responsible for 85 premature
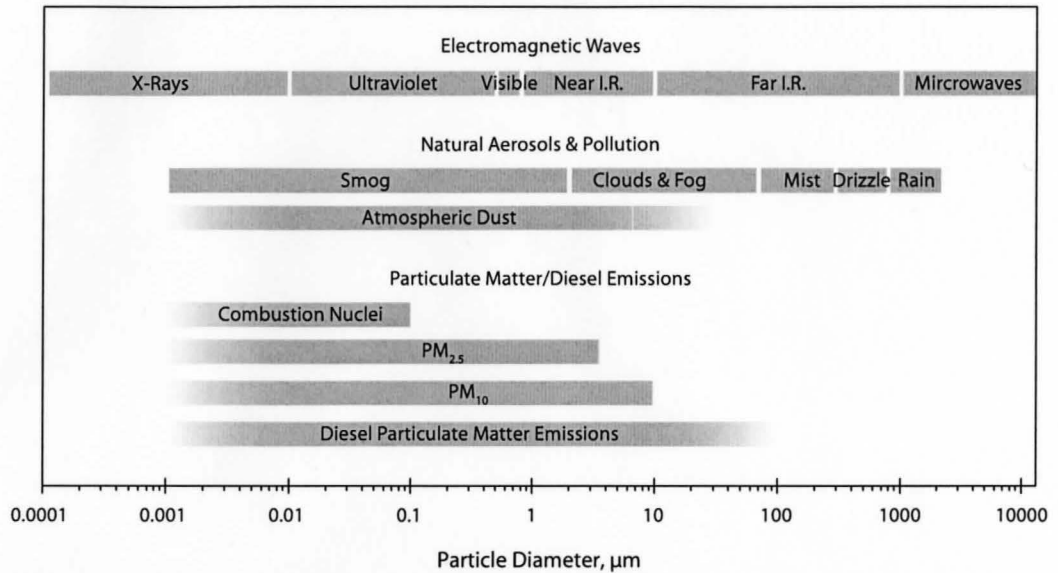
Figure 1.1: Spectrum of particle sizes.

mortalities in the Hamilton-Wentworth region, and 193 additional hospital admissions per year. This corresponded to an estimated 94% of the premature mortalities and 64% of the additional hospital admissions per year for all pollutants examined in their study. Dockery et al. (1993), Samet et al. (2000) and Klemm et al. (2000) also cite evidence linking mortality to increased exposure of respirable particulates. The effect of fine particulate matter on mortality has been shown to be stronger than other atmospheric pollutants, including coarser modes of PM. For example, Klemm et al. (2000) confirmed previous findings showing that a 10 $\mu g/m^3$ increase in two-day exposure to atmospheric particulate matter resulted in an increase in mortality of 1.3% and 0.4% for $PM_{2.5}$ and $PM_{10/15}$, respectively. Gauderman et al. (2004) also found that exposure to atmospheric $PM_{2.5}$ had a strong correlation with retarded lung capacity development in 10 to 18 year old children, and noted that diesel vehicles are largely responsible for the $PM_{2.5}$ in the worst study areas.

3
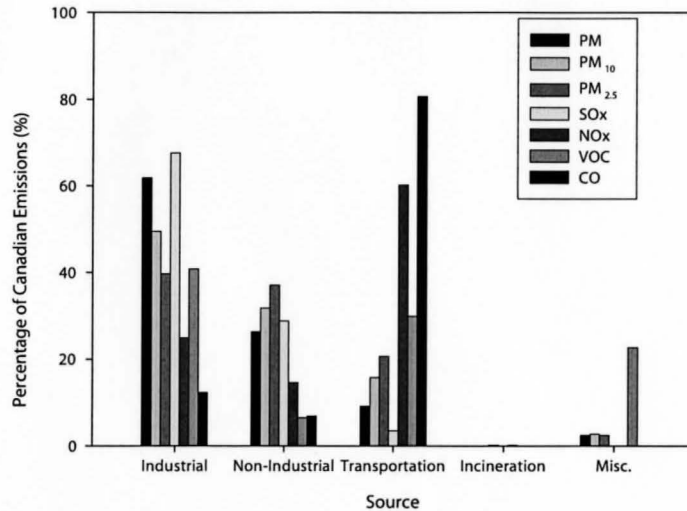
Figure 1.2: Percentage of Canadian pollutant emissions, by source. *Adapted from: Environment Canada (2002)*

The fine particulate matter present in the atmosphere, along with ozone, are also the main components of smog. Smog results in reduced visibility and eye problems. Smog is also associated with soiling and erosion of buildings and monuments, as well as other issues such as climate change and acid rain.

Transportation is a significant source of primary particulate matter. For example, in Canada, transportation results in more emissions than all other sources combined, as illustrated in Figure 1.2. Further, diesel powered vehicles, including heavy-duty trucks, light-duty trucks and other vehicles, rail transport, off-road vehicles, etc, are responsible for over 80% of primary transport-related PM_{10} and $PM_{2.5}$ emissions in Canada, as shown by Figure 1.3. Heavy-duty diesel vehicles alone are responsible for almost half of the DPM emissions. It is also clear from Figures 1.2 and 1.3 that diesel engines used in transportation also emit a large proportion of the PM precursor gases that are a further source of atmospheric PM.

The recognition of the health-related and environmental problems associated

4
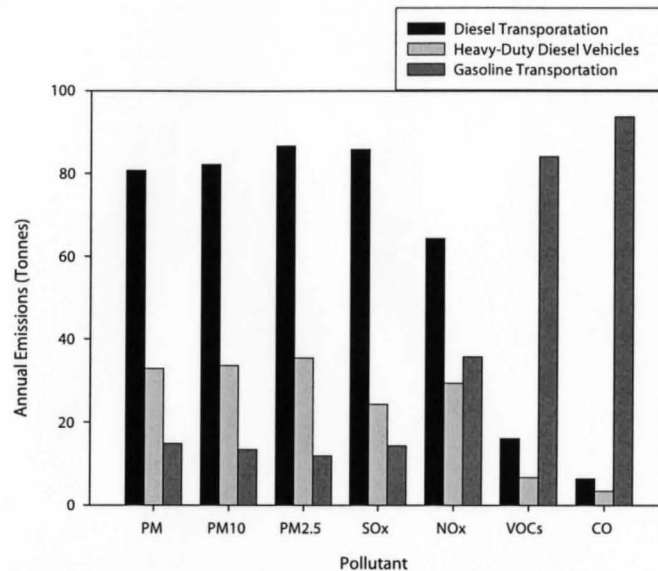
Figure 1.3: Percentage of 1995 Canadian national transportation emissions of various pollutants, by fuel type. *Adapted from: Environment Canada (2001b)*

with diesel particulate matter has motivated significant changes in emissions legislation in recent years. The European Union, the United States, and Japan have created direction-setting standards for the rest of the world. The trends in legislation governing DPM emissions in heavy-duty and light-duty trucks, buses, and passenger cars in these jurisdictions are summarized in Figures 1.4 – 1.7. It is clear that significant technological improvements are necessary to obtain the fivefold reduction in fine PM emissions for passenger vehicles and twenty-fold (or more) reduction for heavy-duty vehicles. Similar emission standards would be expected for stationary and marine sources as well.

The existing technology to reduce the emissions of DPM and precursor gas emissions from automotive diesel engines include exhaust gas recirculation (EGR) for reduction of NO_x, diesel particulate filters/traps for PM abatement, and catalysts for oxidation of hydrocarbons and reduction of NO_x. The most common treatment for
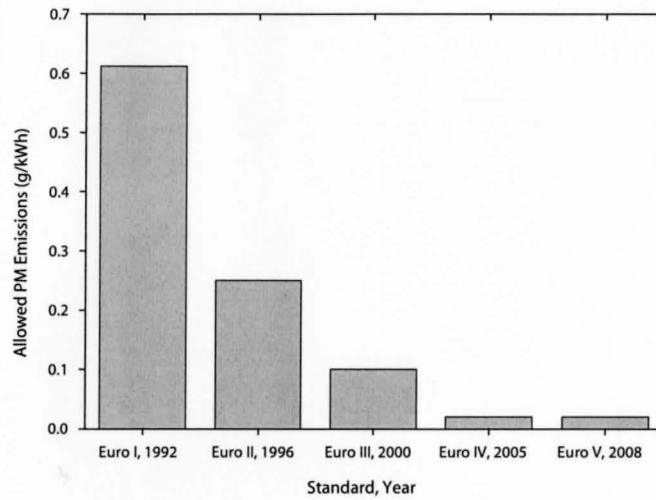
Figure 1.4: PM emissions standards for diesel-powered heavy-duty trucks in the EU.
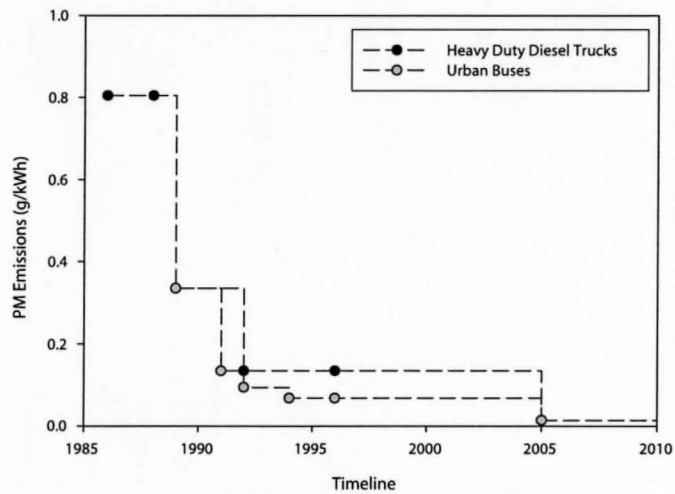
Figure 1.5: PM emissions standards for diesel-powered heavy-duty trucks and urban buses in the US.
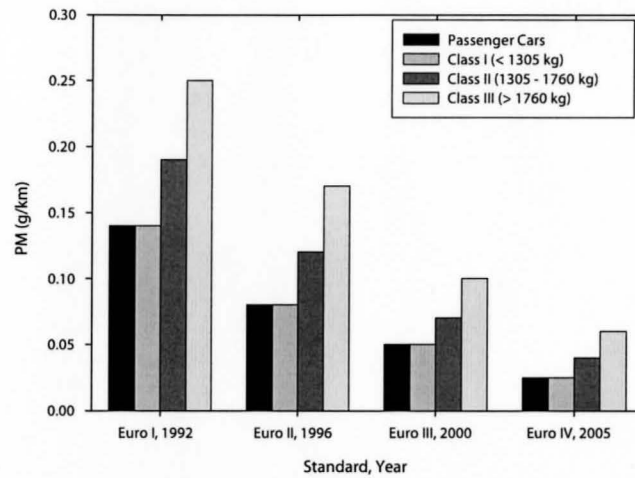
Figure 1.6: PM emissions standards for diesel-powered passenger cars and light-duty trucks (Class I-III) in the EU.
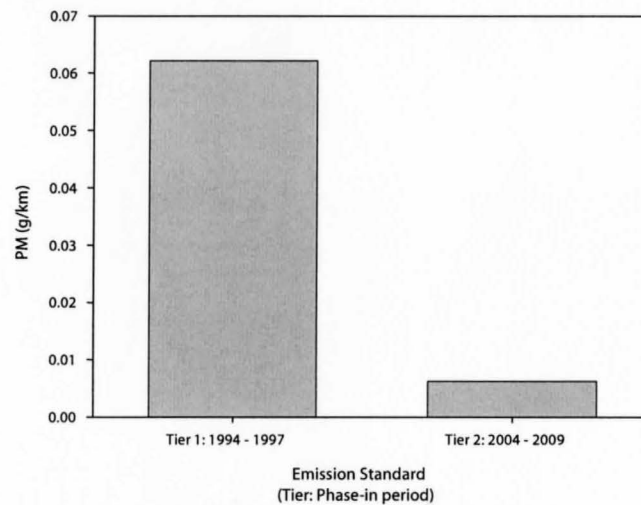
Figure 1.7: PM emissions standards for diesel-powered passenger cars in the US.
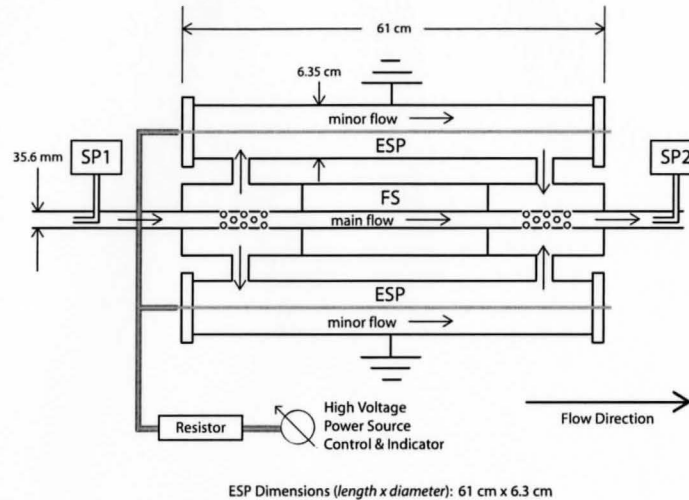
Figure 1.8: The proposed flow-separator type electrostatic precipitator concept for diesel particulate matter abatement.

particulate matter is the particulate filter with regeneration. This type of device is used upstream of other pollution control devices to ensure they operate under PM-free conditions. Particulate filters are quite effective at removing DPM from the exhaust stream (Walker, 2004), but they are generally associated with a high pressure drop (decreasing overall efficiency) and high installation/replacement cost.

The objective of the present work was to develop and characterize a novel PM reducing flow-separator and electrostatic precipitator (FS-ESP) system. A schematic of the proposed FS-ESP device is shown in Figure 1.8. The flow separator divides the flow into a pass-through flow and a highly particulate loaded flow at the perforated separation section. The flow separator uses diffusion and convective forces to concentrate the DPM into the branches. The particulate matter in the highly particulate loaded flow is then collected using ESPs before rejoining the main flow.

The key features of the separator are the inlet geometry and the perforations that allow particulate matter-laden gases to flow to the ESPs. The flow separator was

characterized for two inlet configurations: a straight inlet section and an expanding inlet section, located directly upstream of the perforations. This creates an expansion flow to convect the particulate matter towards the perforations, aiding in particle separation from the main flow.

Electrostatic precipitators (ESPs) are commonly used to remove solid or liquid particulate matter from industrial processes such as blast furnaces and utility boilers (Masuda and Hosokawa, 1995). The collection efficiency of ESPs can easily reach 99% or more, by mass, even for submicron particles (Hall, 1990). ESPs have generally not been considered for treatment of diesel particulate matter because of the size required to reasonably treat the high exhaust gas flow rates as well as problems associated with deposition of particulate matter on the discharge and collection electrodes (Masuda and Moon, 1983). The separator concept maximizes ESP efficiency while minimizing system pressure drop and ESP dimensions typically associated with treatment of a full diesel exhaust flow.

A separator of this type has been successfully used to separate particulate matter from natural gas exhaust streams (Harvel et al., 2004). The device was capable of achieving 97 − 99% particle separation efficiencies, with only 1 − 3% of the flow being diverted to the ESP, at flow rates of 5 − 8.5 m^3/h (normalized to standard conditions). The corresponding Reynolds numbers at the inlet of the flow separator were 1640 − 2800. The overall collection efficiency of the device was reported as 76% (by mass) for the 8.5 m^3/h case, with 30 kV applied to the ESP.

The thesis was organized into five chapters and an appendix. A literature review of topics relevant to this work follows this introductory chapter. The next chapter describes the experimental facilities, then a chapter is dedicated to highlighting results and analysis from this work. The final chapter outlines several conclusions of this work and presents recommendations for future work. The appendix provides

9

an overview of the design and characterization of the micro-dilution tunnel used to quantify particulate matter levels in this work.

CHAPTER 2

LITERATURE REVIEW

This chapter reviews literature related to diesel particulate matter dynamics and control. In the first section, typical diesel engine emissions and interactions are outlined. Next, diesel particulate matter treatment strategies in use and under development are discussed, as well as a brief presentation of some of the flows expected in the flow separator being studied. Particle dynamics are discussed in the context of the diesel particulate matter - exhaust gas flow in the next section. Finally, sampling methods are reviewed, focussing on dilution techniques.

2.1 Diesel Engine Emissions

Diesel engines are common power plants for heavy-duty applications such as trucks and buses, and are enjoying increased use in passenger vehicle applications (e.g. Walker, 2004). The diesel engine offers higher efficiency and durability than spark ignition engines, often resulting in better economy. The products of combustion

from diesel engines and their sources are summarized in Table 2.1. Typical exhaust gas emissions from an early 1990s diesel engine are listed in Table 2.2. One of the major differences between the emissions of diesel and spark ignition engines is that the diesel engine produces much higher PM emissions. The exhaust gases from diesel engines are also more oxidizing, because of higher air-fuel ratios (Adler et al., 1993, Corro, 2002).

Much of the research and development of diesel engines prior to the early 1980s attempted to find generalized relationships between emissions and operating conditions or engine design principles in order to optimize engine performance (see Alkidas and Cole, 1983). More recent studies suggest that the relationship between emissions and specific operating parameters such as the air to fuel ratio is more complex than previously thought and much of the research no longer attempts to characterize the typical diesel engine. For example, data reported by Corro (2002) suggests there is little correlation between the air to fuel ratio and total particulate, hydrocarbon, sulfates (solid), or soot emissions, even on a single engine with all other parameters kept constant.

There is, however, generally a tradeoff between NO_x and particulate matter (Alkidas and Cole, 1983, Yanowitz et al., 2000). Thus conditions that favour NO_x emissions reduction tend to cause an increase in PM emissions, and vice-versa. It is this tradeoff that has led researchers to conclude that it will be necessary to employ various exhaust aftertreatment strategies to effect cleaner tailpipe emissions in standard diesel engines, in conjunction with development of the engine design (Su et al., 2005).

Several engine design parameters and exhaust gas aftertreatment strategies used to reduce emissions from diesel engines are outlined in Table 2.3. It is necessary to consider particulate matter removal strategies together with other pollution control

Emissions	Source
Gaseous emissions	
N_2	
NO/NO_2	Reaction between nitrogen and oxygen in air; minor contribution from nitrogen in fuel (cylinder)
CO/CO_2	Incomplete combustion
H_2	
SO_2/SO_3	Oxidized organic sulfur in fuel (cylinder)
HC (C_2 - C_{15})	Unburnt fuel cylinder
Oxygenates	
Organic nitrogen and sulfur compounds	
Liquid Emissions	
H_2O	
H_2SO_4	
HC (C_2 - C_{15})	Unburnt fuel (cylinder)
Oxygenates	Unburnt fuel (cylinder)
Polyaromatics	
Solid Emissions	
Soot	Oxygen deficient combustion regions (nuclei); Coagulation (cylinder/exhaust line)
Metals	Engine wear (cylinder)
Inorganic compounds	
Sulfates	Further oxidized SO_2 (exhaust line)
Solid hydrocarbons	

Table 2.1: A summary of diesel engine exhaust components and their formation mechanisms/sources (Corro, 2002)

technologies, as the dynamics of exhaust properties are highly interdependent on each other. The engine can be optimized using these techniques to produce emissions suitable for a given pollution control strategy. The pollution control system must then be optimized to treat particulate matter, so as to meet tailpipe emissions requirements.

Exhaust Gas Component	Units	At Idle	At Maximum Output
Nitrous oxides (NO_x)	ppm	$50 - 200$	$600 - 2500$
Hydrocarbons	ppm C_1	$50 - 500$	< 50
Carbon monoxide	ppm	$100 - 450$	$350 - 2000$
Carbon dioxide	Vol. %	< 3.5	$12 - 16$
Water vapour	Vol. %	2 - 4	< 11
Oxygen	Vol. %	18	$2 - 11$
Nitrogen, etc.	Vol. %	residual	residual
Exhaust gas temperature	°C	100 - 200	550 - 750

Table 2.2: Typical composition of diesel exhaust gas. Source: Bauer et al., 2000

2.1.1   Diesel Engine Particulate Matter Emissions

Diesel particulate matter is classified into three distinct size groupings, as shown in Figure 2.1. The nuclei mode is a solid, spherical (5 – 50 nm diameter), carbonaceous core. These solid carbon particles form in fuel-rich regions of the combustion flame, through pyrolysis of the fuel and lubricant. Oxidation of the carbon particles at the high temperatures encountered in the cylinder reduces their size. These nuclei particles undergo processes of surface growth, where gas-phase molecules become attached to nuclei and transform into solids (Heywood, 1988). The competition between growth mechanisms and the size reduction by oxidation determines the size distribution of the nuclei mode particles. The majority of the nuclei mode particles emitted at the tailpipe are formed during cooling or dilution, by homogeneous nucleation of precursor gases in the exhaust line, to form hydrocarbon or sulfate nanoparticles (Kittelson, 1998).

Accumulation mode particles are between 0.1 and 1 μm in diameter and are formed by agglomeration of the smaller carbonaceous nuclei mode particles. The components of a typical accumulation mode particle are shown in Figure 2.2. These form in a chain-like structure that can be described as being fractal in shape (Wentzel et al., 2003). Agglomeration occurs because the particulate matter is surrounded by

14

Pollution Control Technology	Target	Comments	Example
Engine Measures			
Combustion chamber design	Fuel economy, NO_x, PM, HC	Direct injection; divided combustion chamber	Kidoguchi et al. (2003), Liu and Zhang (2004)
Fuel injection timing	NO_x, HC	Emissions highly dependant on injection timing.	Alkidas and Cole (1983), Liu and Zhang (2004)
Fuel injection/mixing	PM, HC	Increased mixing of fuel and air results in lower emissions	Bermúdez et al. (2005)
Excess air	PM, CO, HC	Excess air factor (λ) should be $1.1 - 1.2$	Alkidas and Cole (1983), Jones et al. (2004)
Intake air temperature	NO_x, PM, HC	Increased NO_x, PM levels, decreased HC levels with increased charge temperature.	Alkidas and Cole (1983), Ladommatos et al. (1998)
Exhaust Gas Aftertreatment			
Oxidation catalyst	HC, CO, NO_x	Hydrocarbons and PM are burned using O_2 from exhaust gas	Corro (2002)
Particle trap	PM	Very high PM collection efficiency; some gaseous pollutant effects.	Lin (2002)
EGR	NO_x	Reduce oxygen availability for oxidation of N_2 to NO_x, up to 70% NO_x reduction; up to 150% PM penalty.	Ladommatos et al. (1998), Abd-Ala (2002), Zheng et al. (2004)

Table 2.3: Pollution control strategies currently in use.
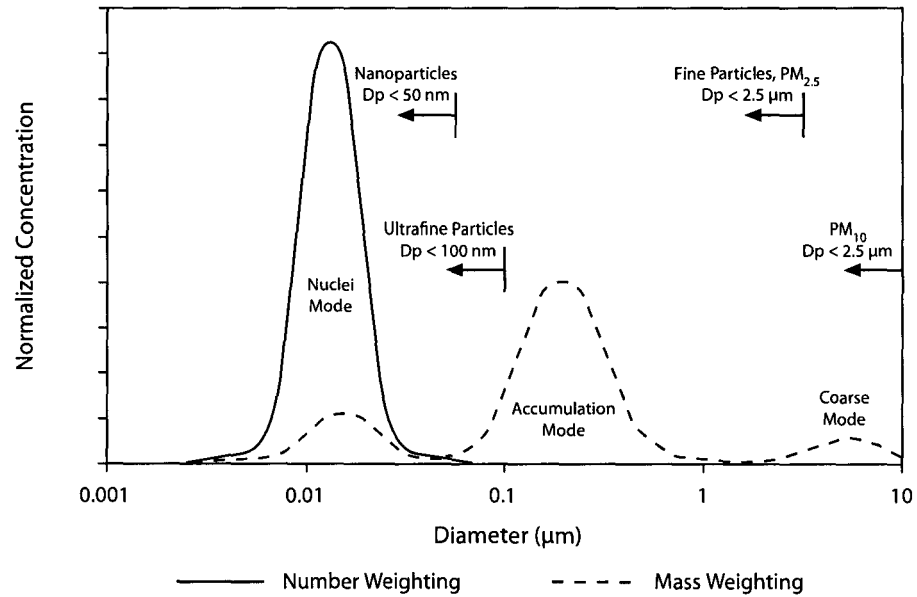
Figure 2.1: Diesel particulate matter size distributions. Adopted from Kittelson et al. (1999)

a hydrocarbon and sulfate layer, that acts to bind the individual particles together when they collide.

The coarse mode of particulate matter is typically associated with particles that are re-entrained from exhaust line walls, etc, and have significantly larger diameters (1 - 10 μm). The definitions of PM_{10} and $PM_{2.5}$ as well as the conventional fine, ultrafine and nanoparticle size designations are also illustrated in Figure 2.1.
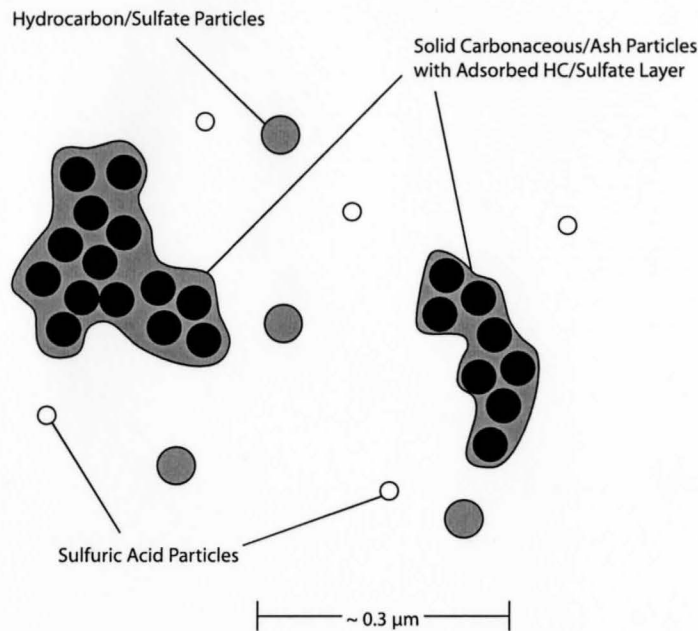
Figure 2.2: The structure of particulate matter in diesel engine exhaust. Adopted from Kittelson et al. (1999)

2.2 Particulate Matter Removal

The removal of particulate matter from its carrier gas is desirable in many industrial and environmental applications. Figure 2.3 illustrates several methods for separation of the particulate phase from the carrier gas phase, including the settling chamber, the baffle chamber, the impactor, the baghouse filter, the wet scrubber, the centrifugal collector, and the electrostatic precipitator. A brief discussion of these methods is included here, with a more in-depth discussion of the techniques appropriate for treatment of combustion exhaust gases. A discussion on aerosol dynamics is presented at the end of this chapter for reference.

The settling chamber, baffle chamber and cyclone separator are all inertial separators (Mody and Jakhete, 1989). They separate the particulate phase from the

17
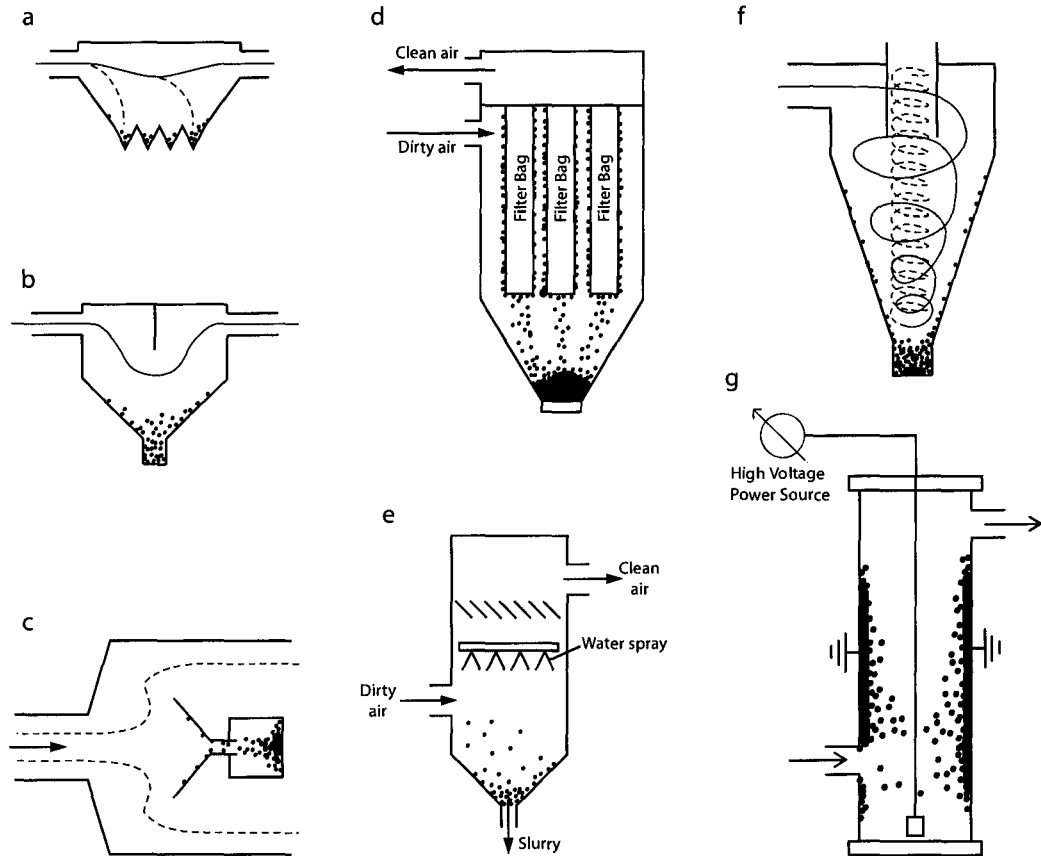
Figure 2.3: Several common dust collection devices: (a) Settling chamber, (b) Baffle chamber, (c) Impactor, (d) Baghouse filter, (e) Wet scrubber, (f) Centrifugal collector, and (g) Electrostatic precipitator.

carrier gas using gravitational, inertial and centrifugal forces. The solid phase is deposited in a location where it can no longer be entrained into the gas phase, then transported to a hopper for storage and removal.

The settling chamber is a simple device that retards the carrier gas flow in a chamber that is significantly larger in cross-section than the conveying duct. This allows the particulate phase to settle into the hopper area because the gravitational force on the particles is larger than the convective force. Thus the settling chamber

is suitable only for larger, heavier particles.

The baffle chamber can be much smaller than the settling chamber because it takes advantage of the inertia of the particles. One or more baffles cause the gas to abruptly change direction, causing the particulate matter to cross the fluid streamlines and collect in the hopper. The impactor and virtual impactor operate on the same principle, but are generally used to classify particles by size (Gotoh and Masuda, 2001).

The cyclone separator separates the solid particulate matter from the gaseous carrier phase using centrifugal force, which can be 1000 – 20,000 times the force of gravity (Sutherland, 2005). The gas-particle stream is introduced tangentially into a rotating conical chamber, and the particulate matter is accelerated towards the chamber wall. The clean gas then exits the cyclone separator through the top of the device. The cyclone separator is effective at removing particles larger than several microns in diameter (Friedlander, 1977).

The wet scrubber uses a liquid water spray to increase the mass of the particles in the aerosol stream combined with one of the inertial separation mechanisms described above. A simple wet scrubber is termed the nozzle scrubber, as depicted in Figure 2.3(e). Here the particulate-laden gas enters the scrubber, and rises through a water spray. The particulate matter is effectively enlarged when it comes into contact with the water spray through mechanisms of inertial impaction, interception, diffusion and in some cases, condensation and nucleation (Mody and Jakhete, 1989). The particulate matter then settles to the hopper at the bottom of the scrubber. Lanzerstorfer (2000) notes that the collection efficiency of particles with diameters as small as 0.6 μm is possible in a wet scrubber when the particles and the water spray are charged with opposite polarity.

The baghouse filter is a commonly used name for a system that uses an array

of fabric filters, as illustrated in Figure 2.3(d). The particulate laden gas passes through the filters, which are made of cotton, synthetic or glass-fiber material, and the particulate matter is deposited on the filter surface through the mechanisms of inertial impaction, interception, diffusion and electrostatic forces (Mody and Jakhete, 1989).

These techniques have space and energy requirements that are generally poorly suited to mobile applications. Further, these devices are not best suited to remove the submicron particles typically associated with diesel engine exhaust.

2.2.1   Diesel Particulate Trap

The main DPM treatment technology in use today is the diesel particulate trap, in combination with an oxidation catalyst to aid in regeneration (Walker, 2004). The particulate trap consists of a series of channels with porous walls, made of cordierite or silicon carbide, as shown in Figure 2.4. The particulate matter deposits on the porous walls by impaction, interception and diffusion as it passes through. The pressure drop across the diesel particulate filter increases with time as the soot builds up. Thus, the filters require regeneration, where the soot is oxidized. The particulate matter will oxidize if the exhaust gas temperatures are in the range of 550 – 600 °C, or NO_2 can burn the particulate matter at a temperature of 250 – 300 °C. The NO_2 levels emitted by the engine are small, so a catalyst is often used to convert NO to NO_2. This type of system is commonly called the continuously regenerating trap, or CRT (Walker, 2004). The CRT is appropriate for heavy-duty diesels, since the exhaust temperatures are consistently high enough for PM removal. Typical performance of a CRT system is shown in Table 2.4. There is also significant conversion of hydrocarbons and CO and some reduction of NO_x as a byproduct of the oxidation catalyst.

If the exhaust temperature is too low or there is not enough NO, active regeneration techniques must be been applied. Active regeneration uses the catalyst,

Oxidizing Catalyst   Particulate Filter

Exhaust Flow Direction
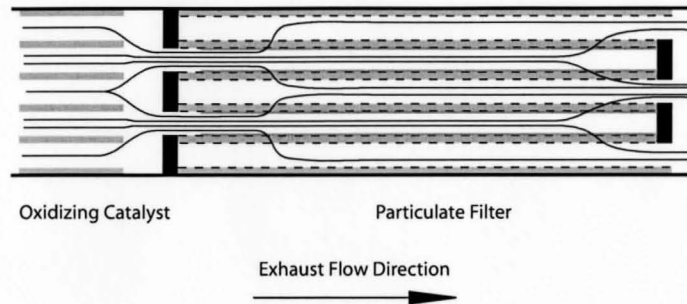
Figure 2.4: Schematic of a diesel particulate filter with oxidation catalyst.

	HC (g/kW·h)	CO (g/kW·h)	NO$_x$ (g/kW·h)	PM (g/kW·h)
Engine Baseline	0.162	0.989	7.018	0.163
Engine + CRT	0.003	0.002	6.874	0.008
Euro IV Limits	0.460	1.500	3.500	0.020

Table 2.4: Performance of the continuously regenerating particle trap on a heavy-duty vehicle (Walker, 2004).

particulate trap, and an engine management system, and in some cases, a fuel-based catalyst (Walker, 2004). In this case, the engine management system changes fuel injection strategy when regeneration is required, increasing the exhaust temperature, and the the CO and hydrocarbon emissions. The CO and hydrocarbons are combusted in the catalyst, resulting in temperatures sufficient to burn the trapped particulate matter. This type of system is most appropriate for light-duty applications such as the passenger car, and has been implemented by auto makers such as Peugeot-Citroen.

Oxidation catalysts are also used to lower CO, gaseous hydrocarbons, and liquid hydrocarbon emissions (Corro, 2002). This type of catalyst can result in a reduction of particulate matter mass emissions, as shown in Table 2.5, because the adsorbed hydrocarbon layer is removed in the catalyst leaving just the carbonaceous particulate.

	CO (g/km)	HC + NO$_x$ (g/km)	NO$_x$ (g/km)	PM (g/km)
Engine Baseline	0.88	0.54	0.37	0.048
Engine + Catalyst	0.50	0.39	0.35	0.030
Euro III Limits	0.64	0.56	0.50	0.05

Table 2.5: Typical performance of a diesel oxidation catalyst on a light-duty vehicle after 80,000 km. (Walker, 2004)

2.2.2 Electrostatic Precipitation

The electrostatic precipitator became a useful particle collection device in the early 1900s after many years of being a laboratory curiosity (Hall, 1990). The collection efficiency of ESPs can easily reach 99% or more, by mass, even for submicron particles (Masuda and Hosokawa, 1995, Hall, 1990). The main components of an ESP are the discharge and collection electrodes, a high voltage power supply, and a cleaning system. In a cylinder type ESP, a tube is used as the collecting electrode, where a central wire is used as the discharge electrode. The collecting electrode is grounded and a high voltage power supply provides potential to the discharge electrode. When the applied voltage reaches the corona onset voltage, V_c, the corona discharge ionizes the gas surrounding the central wire, resulting in current flow between the discharge and collection electrodes. The electric field between the wire and the tube drives the ions towards the collecting surface, resulting in an ionic wind. The current can typically be related to the applied voltage through a quadratic equation of the form (Masuda and Hosokawa, 1995)

$$I = AV(V - V_c). \tag{2.1}$$

A typical electrical operating curve is shown in Figure 2.5. Sparking occurs when the voltage reaches a certain value, V_s, which is the maximum voltage that can be applied. Many other geometries exist.
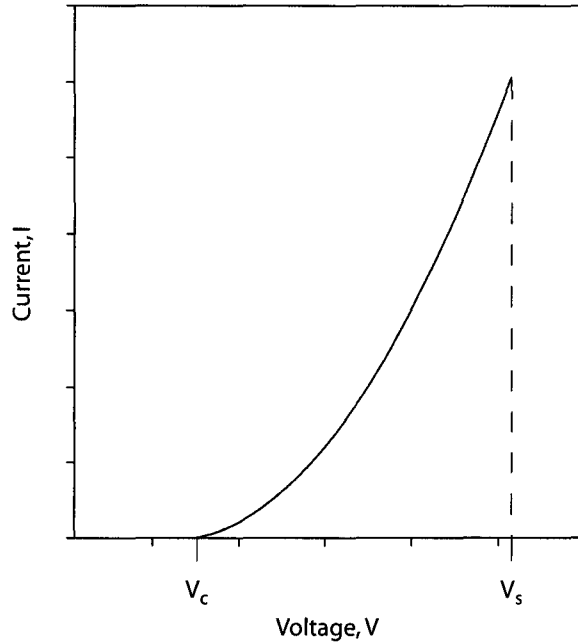
Figure 2.5: Typical ESP current-voltage curve illustrating corona onset voltage (V_c) and sparking voltage (V_s) (Masuda and Hosokawa, 1995).

The current-voltage characteristics of ESPs are principally affected by the ESP design, however the properties of the gas passing through the ESP are also important. An increase in gas density increases the current discharge for a given voltage, with a small decrease of the corona onset voltage (Riehle and Löffler, 1991). An increase in gas density could be achieved by lowering the gas temperature, which is accompanied by an increase in the electrical resistance of the gas. Here it is the change in electrical resistance that affects the discharge characteristics. Zhuang et al. (2000) showed experimentally that increased gas velocity in the ESP tends to increase the corona onset voltage and decrease the discharge current because of the decrease in

ion residence time.

Particle charging in ESPs occurs in the corona discharge field. In the case of negative corona (negative applied voltage), the surrounding gas becomes negatively charged in the region directly surrounding the wire. Both field and diffusion charging contribute to the charge on particles (Masuda and Hosokawa, 1995, Chen and Lai, 2004). The electric field between the two electrodes results in a force applied to the charged particle, and thus the particle takes on the electrostatic velocity, given by Masuda and Hosokawa (1995) as

$$V_{TE} = \frac{qE_{co}C_c}{6\pi\mu_g}. \tag{2.2}$$

Here, q is the charge on the particle, and E_{co} is the intensity of the collection field.

The collection efficiency in percent is given by

$$\eta = (1 - P) \times 100, \tag{2.3}$$

where

$$P = \exp\left(-\frac{A}{Q}\omega_e\right) = \exp\left[-\left(\frac{A}{Q}\omega_k\right)^m\right]. \tag{2.4}$$

These are known as the Deutsch and Matts-Ohnfeldt equations (Hall, 1990). P is the fractional precipitator loss, A is the collecting area, Q is the flow rate of the gas, ω_e is the Deutsch effective particle migration velocity ($\omega_e = (1 - \beta)\omega$, where β is the net loss factor and ω is the theoretical migration velocity), ω_k is the Matts particle migration velocity, and the exponent m depends on particle size distribution (for fly ash, $m = 0.5$, increasing for finer particles). From this relationship, it is clear that as the carrier gas flow rate through the ESP increases, its efficiency tends to decrease.

Corona wind is a secondary flow that can be induced within an ESP. Corona wind occurs when the corona-induced ions transfer momentum to the gas phase (Ma-

suda and Hosokawa, 1995). Chang and Touchard (1999) provide dimensionless ratios that can be used to ascertain the likelihood of EHD induced secondary flows. In particular, the EHD (electrohydrodynamic) number, or conductive electric Rayleigh number, is given by

$$Ehd = \frac{eN_{io}E_oL^3}{\rho_f\nu_f^2} \qquad (2.5)$$

(IEEE-DEIS-EHD Technical Committee, 2003) and the Masuda Number, or Dielectric electric Rayleigh number, is given by

$$Md = \frac{\varepsilon_oE_o^2L^2}{\rho_f\nu_f^2} \qquad (2.6)$$

(IEEE-DEIS-EHD Technical Committee, 2003). Here, ε_o is the dielectric constant in a vacuum, N_{io} is the ionic number density, and L is the characteristic length under consideration. The secondary flows induced in an ESP cannot be neglected when the ratios Ehd/Re^2 and/or Md/Re^2 are greater than one as in these cases the EHD body forces become significant.

In some situations, the high collection efficiencies associated with ESPs are difficult to obtain. For instance, the particle size has a strong influence on migration velocity. The migration velocity is a minimum for particles with diameters in the range of 0.1 to 1.0 μm. Agglomerators have been used in an attempt to mitigate this phenomenon (e.g. Zukeran et al., 2000, Masuda and Moon, 1983). the performance of the ESP can also be reduced by back corona, corona quenching, dust reintrainment, and insulation of the discharge electrode.

As a result, ESPs have not been considered as a major DPM reduction strategy. Masuda and Moon (1983), however, developed a moving belt-type ESP combined with a precharger and parallel-plate collector-type pre-agglomeration system. They achieved high collection efficiencies ($\sim$ 90%) for diesel engine exhaust flow rates typical

of a 2L engine. The system constantly cleaned the collection electrode by circulating it through a rapping section. The concept was not developed for commercial use on vehicles, however.

2.2.3 Dust-Flow Separation in Combustion Exhaust Streams

Recently, Harvel et al. (2004) characterized a flow-separator type electrostatic precipitator for control of particulate matter emissions from natural gas combustion, similar to the device proposed for this study. A schematic of this flow separator-ESP device is shown in Figure 2.6. The flow-separator used in that work separated the flow into two streams, a high flow rate stream with low particulate matter concentration, and a low flow rate stream with high particulate matter concentration. The low flow rate stream passes through a perforated section to an electrostatic precipitator, where the particulate matter is deposited on the grounded collection electrode, and the two gas streams recombine. The mass-averaged size of the natural gas aerosol is typically an order of magnitude less than diesel particulate matter, with similar distribution. The overall collection efficiency of the device was reported as 76% (by mass) for the 8.5 m^3/h case (Re $\approx$ 3100), with 30 kV applied to the ESP.

When the exhaust stream flowed to the perforated section, it was thought that the sudden expansion could cause particle stagnation, eventually migrating to the ESP section by convection and diffusion, with diffusion being the dominant transport mechanism. The device was capable of separating 97 – 99% of the particles by particle number, for flow rates of 5 – 8.5 m^3/h at Reynolds numbers of 1640 – 3100. It was observed by experiment and numerical modeling that only 1 – 3% of the flow was diverted to the ESP leg for these flow rates. This represents a significant phase separation. The Reynolds number ranged from 1640 to 3110 in these experiments. The details of the phase separation in this device were not well understood.

Clearly, the dynamics of the flow at the perforated section is of interest in
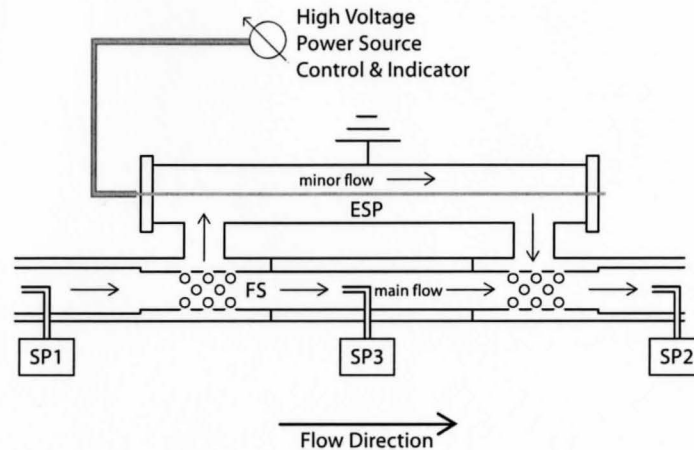
Figure 2.6: FS-ESP used in study by Harvel et al. (2004).

this work. Geometries similar to this type are common in acoustic research, but no literature was found on the flows that develop in this geometry.

Wang (2005) proposed a virtual impactor type dust flow concentrator for use with ESPs to remove diesel particulate matter from the minor flow branch, as shown in Figure 2.7. The exhaust flow enters the virtual impactor and changes direction at the lip, due to the contraction at the concentration probe. A fraction of the flow enters the minor flow leg, while the majority of the flow passes through the major flow leg. During the abrupt change in gas flow direction, the inertia of the particulate matter causes it to cross the gas streamlines and become concentrated in the minor flow. The results presented in this work indicated that 5 – 30 % of the flow in the minor leg carried 1.2 – 2 times the inlet particulate matter mass concentration. The Reynolds number of the flow at the inlet ranged from 2,200 to 25,700, with higher particulate matter mass concentrations observed at the higher Re. Several lip positions were examined with some increase in concentration for deeper lip positions. The effectiveness of this dust flow concentrator was limited because
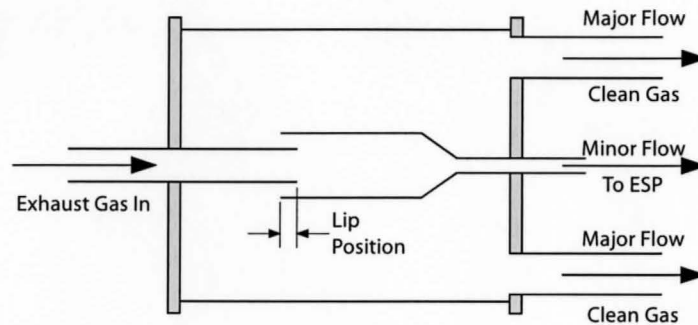
Figure 2.7: Virtual impactor type dust flow concentrator used in the study by Wang (2005).

of the submicron particle size. Higher concentration in the minor flow leg could be possible by increasing the Reynolds number of the inlet flow and hence the inertia of the particulate matter, but at the expense of increased pressure drop of the whole system.

2.3   Diesel Engine Particulate Matter Sampling

The US standard procedure for diesel particulate matter sampling is a gravimetric method, defined by the United States Code of Federal Regulations (40 CFR 86, 2004). In this method, the full engine exhaust is brought to a dilution tunnel, equipped with either a positive displacement pump-constant sampler or a critical flow venturi to transport the diluted exhaust gas to a particulate filter. The PM is measured in terms of mass of PM per volume of exhaust gas, and is determined by calculating the difference in weight between dry PM loaded filters and clean filters. The standard procedure requires that the temperature of the particulate-laden exhaust gas be 52 °C or less. The usefulness of the 40 CFR 86 (2004) method is limited to time averaged measurements of particulate matter mass emissions, and cannot be used to effectively measure transient emissions.
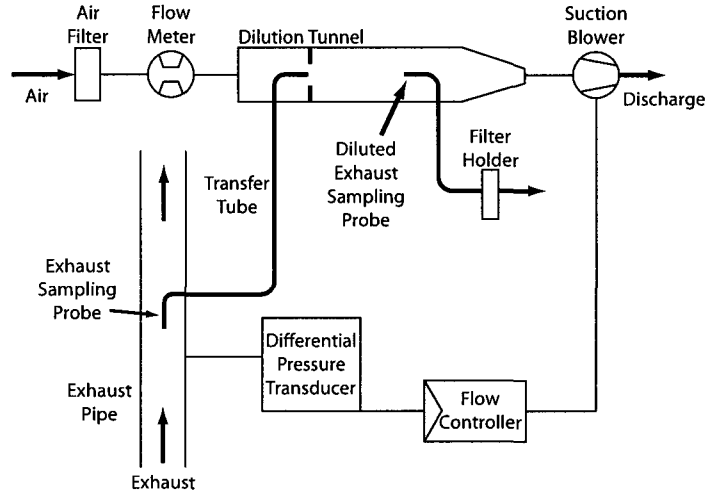
Figure 2.8: Partial Flow Sampling System: Isokinetic system outlined by Vouitsis et al. (2003).

Other sampling methods are in widespread use that address this shortcoming. Exhaust can be sampled from the main exhaust line using a partial flow sampling system that removes and dilutes a partial sample of the full exhaust flow. A schematic of one type of partial flow sampling system is shown in Figure 2.8. In this system, a sampling tube located in the engine exhaust line brings the exhaust gases to the dilution tunnel. A flowmeter controls the amount of filtered air that enters the dilution tunnel that is mixed with the exhaust gases. A second sampling probe is then used to sample the diluted exhaust gases for analysis. Downstream of the tunnel, a suction blower provides the negative pressure to ensure the proper exhaust flow rates, that is controlled using a flow controller.

The dilution ratio and the sampling velocity are two key parameters that must be controlled when using a partial flow sampling system (Vouitsis et al., 2003). The

dilution ratio is given by (e.g Chan et al., 1998)

$$D = V_t/V_s, \qquad (2.7)$$

where V_t is the volumetric flow rate of the diluted mixture, and V_s is the volumetric flow rate of the exhaust sample entering the dilution tunnel. Dilution ratios on the order of 5 to 20 are typically used, but values ranging from 2 to 90 or more have been used, depending on the purpose of the study (Kittelson et al., 1999).

Reichel et al. (1983) observed that the dilution ratio had an effect on the particulate matter mass concentration measured by the partial flow sampling system. They changed the dilution ratio by adjusting both the sampled exhaust flow rate as well as the dilution air flow rate, and found that increased dilution ratios resulted in lower particulate concentrations. Frisch et al. (1979) observed a 40% decrease of particulate matter (by mass) when the dilution air temperature was raised from 15°C to 45°C. Kittelson et al. (1999) concluded that one drawback of the mini-dilution tunnel technique is that dilution of the exhaust gas with room temperature air can result in particle generation and size distribution shifts. This is due mostly to nucleation and condensation during the cooling of the exhaust gases, creating a highly saturated mixture. The soluble organic fraction undergoes homogeneous nucleation and the remaining vapour condensates onto the particles, increasing their size (Kittelson et al., 1999). Coagulation is not a significant factor in the shift in observed PM in the mini-dilution tunnel, because the residence time is too small. Vouitsis et al. (2005) also concluded this by modeling the aerosol dynamics during diesel exhaust dilution. They showed that homogeneous nucleation of the vapour-phase into nuclei mode particles during dilution is suppressed when accumulation mode particles are available as condensation sites. Kittelson et al. (1999) proposed that a two-stage dilution process could alleviate this problem. In the first stage, a hot dilution gas is

used, while in the second stage cold dilution gas is used. This would minimize the opportunity for homogeneous nucleation and condensation of vapour species associated with reduced partial pressures in single-stage cold dilution, while maintaining the lower temperatures required for analysis.

The accurate sampling of exhaust gas requires isokinetic sampling, where the velocity of the undisturbed exhaust line velocity (U_o) is the same as the sampled exhaust gas velocity (U). The velocity ratio is given by

$$N_I = \frac{U_o}{U}.$$
(2.8)

This ensures that a representative sample is carried into the dilution tunnel. Sampling of particulate matter at velocity ratios other than unity results in over- or under-sampling as shown in Figure 2.9. Smaller particles $(d_p < 3 \ \mu m)$ tend to follow the streamlines, while larger ones $(d_p > 3 \ \mu m)$ can cross the streamlines because of their higher momentum. In diesel exhaust, it is mostly the smaller particles that are of interest, because of the characteristic mass and number distributions (see figure 2.1). Thus, when the velocity ratio is greater than one, undersampling occurs because the small particles will be diverted around the sampling probe. Oversampling occurs when the sampling velocity ratio is less than one, because an excess of smaller particles are drawn into the probe. Badzioch (1960) and Watson (1954) address the issue of anisokinetic sampling by proposing corrections for sampling tube orientation and sampling velocity, but these techniques are not typically used in the recent diesel engine emission testing literature.

Other techniques for sampling of particulate matter exist, including a novel dilution system described by *Sierra Instruments* and *Caterpillar Inc* (Ashley, 1993), and the ejector-diluter characterized by Wong et al. (2003), which uses a two-stage (heated and room temperature) dilution technique.
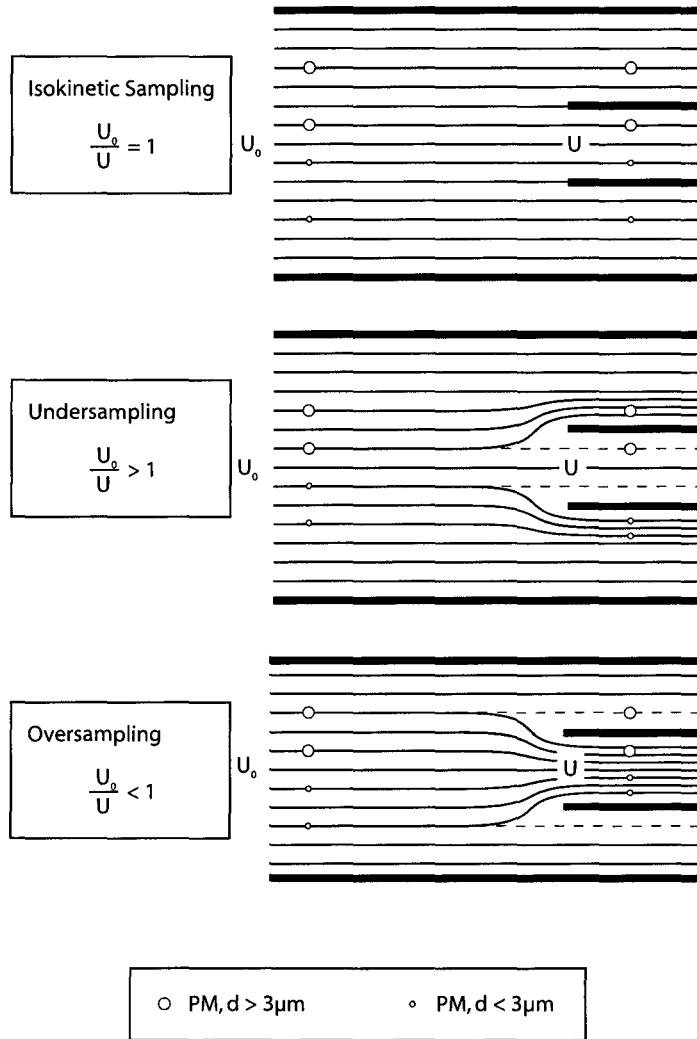
Figure 2.9: Effect of sampling velocity ratio on exhaust gas streamlines and particulate matter sampling.

As an alternative to the particulate filter gravimetric technique, other commonly used mass measurement techniques such as the optical opacity meter allow real-time analysis of mass emissions, including transient mass measurement. Size distributions are often measured using instruments such as the scanning mobility particle sizer (SMPS) combined with the condensation-nucleation particle counter (CNPC). Methods for quantifying diesel particulate matter emissions without the need for dilution have been developed and are under study, such as laser incandescence (Snelling et al., 1999). Adachi (2000) provides an excellent summary of these techniques.

2.4   Aerosol Dynamics

The equations describing the motion of particulate matter are the continuity equation (e.g. Beuthe and Chang, 1995)

$$\nabla \cdot \boldsymbol{J_p} = -\frac{d\,[N_p]}{dt} + \text{source} - \text{sink}, \qquad (2.9)$$

where

$$\boldsymbol{J_p} = N_p \boldsymbol{U_g} \pm B_p N_p \boldsymbol{E} - D_p \nabla N_p - G_p N_p \nabla T_g. \qquad (2.10)$$

Here, $\boldsymbol{J_p}$ is the particle flux density, N_p is the particle density, $\boldsymbol{E}$ is the electric field, D is the diffusion coefficient, $\boldsymbol{U}$ is the carrier gas convection, B_p is the particle's mechanical mobility, G is the thermophoresis coefficient, and T is the absolute temperature, with subscripts p and g referring to the particle and gas phases, respectively. The term on the left hand side of Equation 2.9 represents the net flow of particles across a control volume, while the first term on the right hand side represents an accumulation of particles within the same.

2.4.1   Convection

Particles are convected along with the exhaust gas flow. The drag force on a small particle in the Stokes region (Re < 1) is given by

$$F_D = \frac{3\pi\mu V d}{C_c},$$ (2.11)

where V is the relative velocity of the particle to the gas, and d is the particle diameter. For very small particles, where the diameter is smaller than the mean free path of the carrier gas, the particle experiences less drag force because of 'slip'. This is accounted for by using the Cunningham (or slip) correction factor, C_c. Several forms of the Cunningham correction factor have been proposed, as outlined by Hinds (1982).

Larger particles experience a different drag force, given by

$$F_D = C_D \frac{\pi}{8} \rho_g d^2 V^2.$$ (2.12)

The drag coefficient C_D depends on the Reynolds number. In the Newton's law regime ($Re > 1000$), it is given by

$$C_D \cong 0.44$$ (2.13)

and in the transition regime ($1 < Re < 1000$),

$$C_D = \frac{24}{Re}\left(1 + \frac{Re^{2/3}}{6}\right)$$ (2.14)

applies.

In unsteady or accelerating flows, the relaxation time, given by

$$\tau = mB = \frac{\rho_p d^2 C_c}{18\mu},$$ (2.15)

can be used to determine its' response time. The terminal velocity of a particle under the influence of any force is the product of its mechanical mobility (B) and the external force (F), given by

$$V_{TF} = BF = \tau \frac{F}{m} \tag{2.16}$$

in terms of relaxation time τ (Hinds, 1982). Thus, small particles follow fluid streamlines almost perfectly, while larger particles continue in their original direction for a short while before reacting to the change in direction of streamlines. The mobility of a particle (B) in the Stokes regime is also expressed as

$$B = \frac{V}{F_D} = \frac{1}{3\pi \mu d_p}. \tag{2.17}$$

2.4.2 Diffusion

The diffusion of aerosol particles (J_{diff}) due to a concentration gradient dn/dx is modelled using Fick's law, i.e.

$$J_{diff} = -D\frac{dn}{dx}. \tag{2.18}$$

The diffusion coefficient, D, is typically given by

$$D = kTB = \frac{kTC_c}{3\pi \mu_g d_p}, \tag{2.19}$$

where k is the Boltzmann constant, T is the absolute temperature of the gas, C_c is the Cunningham correction coefficient, μ_g is the gas viscosity, and d_p is the particle diameter (Hinds, 1982).

2.4.3 Thermophoresis

The thermophoretic force on a particle is a result of temperature gradients in the carrier gas. Thermophoretic deposition is enhanced by increasing the temperature dif-

ference between the wall and the carrier gas. Particles migrate towards the wall, and deposit there. Thermophoretic deposition is typically much greater than deposition by diffusion whenever the wall temperature is lower than the carrier gas temperature. Thermophoretic deposition is of concern in the design of several diesel-related technologies, including the design of sampling systems and EGR heat exchangers. The thermophoretic force depends on the Knudsen Number, Kn, given by

$$Kn = \frac{\lambda}{L},$$

(2.20)

where λ is the molecular free path of the gas, and L is a representative length scale (in this case, the particle radius: $L = r_p = d_p/2$). For Kn $\ll$ 1, the gas/particle flow is in the continuum regime, where the thermophoretic velocity can be calculated by (e.g. Messerer et al., 2003, Lin and Tsai, 2003)

$$V_{th} = 2c_oC_s\frac{k^* + c_tN_{Kn}}{(1 + 3c_mN_{Kn})(1 + 2k^* + 2c_tN_{Kn})}.$$

(2.21)

For Kn $\gg$ 1, the gas/particle flow is in the free molecular regime, and the thermophoretic velocity is given by (e.g. Messerer et al., 2003, Lin and Tsai, 2003)

$$V_{th} = -K_{th}\frac{\mu_g\nabla T}{\rho_gT_g},$$

(2.22)

where $K_{th} = 0.55$. ∇T is the temperature gradient near the particle, and T_p is the particle temperature. C_c is the Cunningham correction coefficient, and k^* is the ratio of thermal conductivities of the gas and the particles. Messerer et al. (2003) and Rosner and Khalil (2000) suggest that using $k^* = 1.0$ is reasonable for particles such as diesel PM due to a reduction in thermal conductivity of agglomerate particles with fractal dimensions of 1.7 (i.e. porous and chain-like arrangements). Messerer et al. (2003) used $c_m = 1.146$, $c_s = 1.147$ and $c_t = 2.18$, which are the momentum

exchange, thermal slip and temperature jump coefficients, respectively. The case of $Kn \approx 1$ is considered the transition regime.

2.4.4   Electrophoretic Transport

Electrophoretic transport of particles due to an electric field is given by

$$F_E = neE, \tag{2.23}$$

where n is the number of elementary units of charge on the particle, E is the strength of the electric field, and $e = 1.602 \times 10^{-19}$ coulombs is the charge of a single electron (eg. Hinds, 1982).

The terminal electrostatic velocity of a particle undergoing Stokes flow can be obtained by equating the electrostatic force to the diffusional drag force, resulting in

$$V_{TE} = \frac{neEC_c}{3\pi\mu d_p} = neEB. \tag{2.24}$$

Higher Reynolds number flows ($Re > 1$) are common, however, because the electrophoretic velocity can be much greater than the relative velocity of a particle undergoing convective or diffusional transport. In this situation, the electrophoretic velocity is given by

$$C_D \mathrm{Re}^2 = \frac{8neE\rho_g}{\pi\mu^2}, \tag{2.25}$$

where

$$V_{TE} = \frac{\mu}{\rho_g d} \left[\frac{C_D \mathrm{Re}^2}{24} - 2.3363 \times 10^{-4} \left(C_D \mathrm{Re}^2 \right)^2 + 2.0154 \times 10^{-6} \left(C_D \mathrm{Re}^2 \right)^3 \right]$$
$$- \frac{\mu}{\rho_g d} \left[6.9105 \times 10^{-9} \left(C_D \mathrm{Re}^2 \right)^4 \right] \tag{2.26}$$

is suggested by Hinds (1982) for determination of the particle velocity without knowl-

edge of exact values of C_D or Re.

The electrical mobility (Z), given by

$$Z = \frac{V_{TE}}{E},$$ (2.27)

describes how well a particle will move in an electric field. Electrical and mechanical mobility are related through

$$Z = neB.$$ (2.28)

The electrophoretic force is used in electrostatic precipitators to take advantage of the high electrical mobility of particulate matter. When the electrophoretic force is normal to the deposition surface, particles will migrate towards it and deposit there. Electrophoretic deposition can also be an undesirable effect, however, in situations where particles are highly charged and/or a surface is not grounded.

2.4.5   Nucleation, Condensation and Coagulation

Homogeneous nucleation, or self-nucleation, is the term given to the spontaneous formation of nuclei-mode particles. In diesel exhaust gases, this occurs when solid carbon precipitates from supersaturated combustion gases and when the partial pressure of SO_2 or SO_3 is high enough to form liquid nuclei of H_2SO_4 or solid sulfate nuclei. Condensation occurs if the partial pressure of a vapour phase is great enough to transform it into liquid. This acts to increase the size of particles, as well as to increase its adhesive character. For instance, in diesel exhaust, H_2SO_4 will condense on carbon particles, creating a thin, sticky, sulfate layer. Heterogeneous nucleation is a similar process, which increases the size of nuclei.

Coagulation, or agglomeration, of particles occurs when two particles come into contact with each other. Particles adhere to each other due to van der Walls forces, electrostatic forces, and surface tension. The van der Walls force is a result of the

attraction between dipoles formed in the particles. The electrostatic force between the dipoles acts to fuse the particles together over time. Surface tension keeps particles together when two particles come into contact and the thin liquid film surrounding them fills the capillary space between them. Agglomeration occurs between two solid particles, two liquid particles as well as between solid and liquid particles (e.g. between carbonaceous particulate matter and hydrocarbons). These mechanisms shift the mass and number distributions, and can play a significant role when the bulk temperature or pressure of the gas phase changes.

2.4.6 Deposition and Entrainment

Regardless of the deposition mechanism, once the particles are attached to the wall, it is the van der Walls force, electrostatic force, and in many cases, surface tension, that keep them there. Entrainment, or removal, of particulate matter from the wall surface is largely a function of shear stress at the interface between the deposited layer and the carrier gas. In ESPs, the shear stress can be increased due to the ionic wind created by corona discharge (Zukeran et al., 1999).

CHAPTER 3

EXPERIMENTAL FACILITIES

AND METHODOLOGY

In this chapter, the diesel engine test rig, the micro-dilution tunnel system, and the FS-ESP are discussed. A detailed description of each device is presented, as well as the experimental methodology used to characterize them. Finally, a discussion of the experimental uncertainty and data reduction associated with the experiments is presented.

3.1   Diesel Engine Test Cell

The diesel engine rig used in this project is illustrated in Figure 3.1. A single-cylinder Lombardini 15LD 350 diesel engine, equipped with a 5.5 kW Lombardini generator is used in the test facility. The engine was loaded electrically with a variable resistance load, which is described in detail by Charles (2005). The engine was run

on commercially available diesel fuel.

The engine and load were used as a source of particulate-laden exhaust gases. Ambient air from the laboratory enters the rig, shown in Figure 3.1, and then enters the engine, while fuel is fed to the engine from a graduated cylinder. Exhaust gases leave the engine through insulated 35 mm (1 1/4" nominal) piping. The exhaust gas flow is divided into two branches, one used for testing and the other used to bypass some of the exhaust. The flow rate in each branch is controlled by valves. A venturi flow meter (V1) is installed on the by-pass line to measure the exhaust mass flow rate in this leg. The exhaust in this leg then passes through a heat exchanger before being exhausted to the atmosphere. The flow through the test leg passes a sampling point located upstream (SP1) of the FS-ESP test section. The particulate matter downstream of the flow separator is sampled at SP2. The flow through the FS-ESP is measured using a venturi (V2) downstream of the device. The mass flow rate through each of the venturis was determined from the pressure drop across the venturi expansion section and the exhaust gas temperature. Surge tanks are installed at the air inlet and in the exhaust legs to dampen the pulsations in the flow associated with the single cylinder engine.

Temperature was measured at locations SP1, SP2, V1, V2 and in the micro-dilution tunnel, using 3.175 mm (1/8") *Omega* T-type thermocouples. The temperature data was acquired using a *PCI-DAS-TC* thermocouple data acquisition board at a sampling frequency of 0.2 Hz. The voltage from Validyne DP15TL pressure transducers at V1 and V2 was measured with a *Microstar Boards* IDC 1816 board. The transducers were calibrated using a PCL33 high accuracy pressure calibrator (±0.05% of reading). Pressure data was sampled at 1024 Hz, averaged, and recorded at 0.2 Hz. Table 3.2 summarizes the instrumentation used in this work.
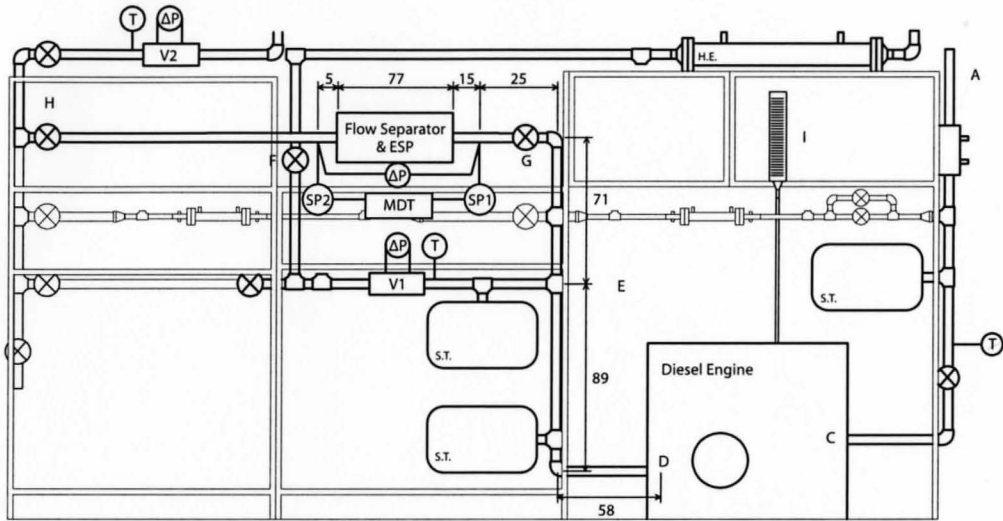
Figure 3.1: Diesel engine rig used in experiments; legend is in Table 3.1. All dimensions in cm.

Symbol	Description
V1, V2	Venturi flow meters
ΔP	Pressure difference
MDT	Micro-dilution tunnel
T	Temperature
H.E.	Heat Exchanger
S.T.	Surge Tank
A	Air inlet
C	Air enters engine
D	Exhaust gases leave engine
E	Exhaust gases split into test and by-pass legs
F	Valve
G	Valve
H	Valve
I	Graduated cylinder containing fuel

Table 3.1: Components of the diesel engine rig shown in Figure 3.1.

Location	Measurement	Instrument	Range	Accuracy
SP1, SP2, V1, V2, MDT	Temperature	OMEGA T-type Thermocouple	250°C - 350°C	±0.9°C
V1	Pressure	Validyne DP15TL Transducer	-6.9 – 6.9 kPa	±0.5% of FS
V2	Pressure	Validyne DP15TL Transducer	-2.2 – 2.2 kPa	±0.5% of FS
SP1, MDT	Pressure	U-Tube manometer	0 – 0.76 m	±2.5 mm
SP1, SP2	DPM Mass Concentration	Environmental Devices Hazdust III	$0.01 - 200$ mg/m^3	±10% of reading
SP1, SP2	Mass Flow rate	Venturi	0 – 45 kg/hr	±1%
MDT	Mass Flow rate	Matheson 605 Rotameter	0 – 50 LPM	±2.5% of reading
MDT	Mass Flow rate	Gilmont 225 Rotameter	0 – 12 LPM	±2% of reading

Table 3.2: Instrumentation used in the present work. (MDT refers to the micro-dilution tunnel)

Component	Dimensions (metric)	Dimensions (imperial)	Material
Primary Sampling Tube	6.35 mm tube × 0.889 mm wall	1/4" tube × 0.035" wall	Stainless Steel
Secondary Sampling Tube	6.35 mm tube × 0.889 mm wall	1/4" tube × 0.035" wall	Stainless Steel
Mixing Chamber	25.4 mm tube × 1.65 mm wall	1" tube × 0.065" wall	Aluminum

Table 3.3: Micro-dilution tunnel dimensions

3.1.1 Micro-Dilution Tunnel

The diesel engine exhaust gas was sampled using a micro-dilution tunnel installed on the diesel engine rig at SP1 and SP2 as shown in Figure 3.2. The micro-dilution tunnel was designed and fabricated specifically for this study. Details of the micro-dilution tunnel and the characterization are given in Appendix B. The sampling tubes located outside of the flow leg and the dilution tunnel were insulated to minimize heat loss. A summary of the key dilution tunnel dimensions is given in Table 3.3.

The particulate matter-laden exhaust flow enters the micro-dilution tunnel from the exhaust line through the primary sampling tube. Dilution air is filtered, then supplied to the dilution tunnel. The flow rate of the dilution air is controlled by a valve integrated into the rotameter housing. Prior to entering the dilution tunnel mixing section, the air must pass through a conditioning section consisting of a series of perforated plates (one radial section and two plates aligned perpendicular to the flow) and mesh screens, and pass over a centrally mounted ferrule. The ferrule acts as a nozzle to provide negative pressure at the primary sampling tube outlet, as well as to enhance mixing of the air and the exhaust flow due to separation of the shear layer.
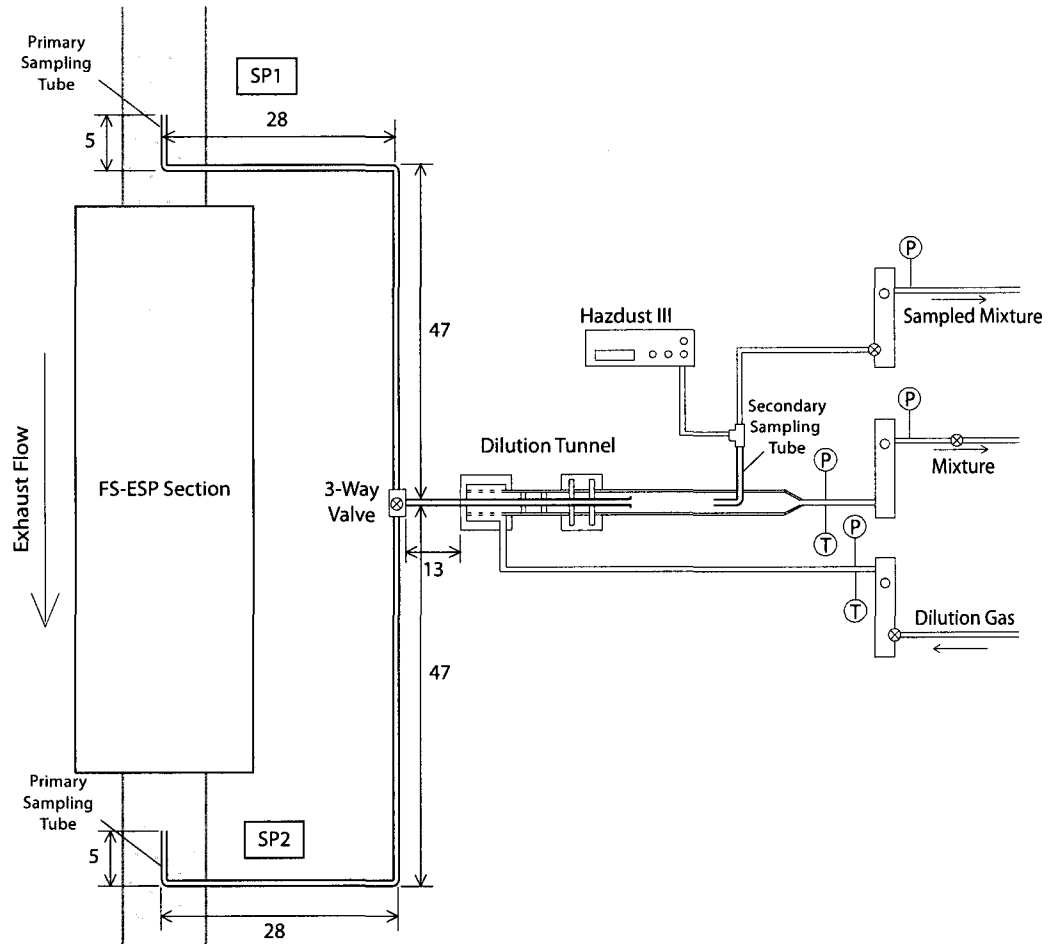
Figure 3.2: Micro-dilution tunnel installed on the rig at SP1 and SP2. All dimensions in cm.

The diluted sample is transferred to an opacity meter (*Haz-Dust III*) for analysis via the secondary sampling probe. The flow rate through the secondary sampling tube is controlled by the valve integrated into the sampled mixture rotameter. The remaining diluted mixture passes through the mixture rotameter, and then to the exhaust line. The mixture flowrate is controlled by a valve located downstream of the rotameter. The line pressure and temperature monitoring was done with T-Type

thermocouples and water manometers at the locations indicated by T and P on the diagram, respectively. The flow rates were corrected for temperature and pressure, although deviation from standard conditions was minor.

The dilution ratio, D, was calculated using the volumetric flow ratio as

$$D = \frac{V_{mixture}}{V_{exhaust}}, \tag{3.1}$$

where $V_{mixture}$ is the diluted mixture volumetric flow rate, i.e. the combined flow rate through the mixture rotameter and the sampled mixture flow meter, and $V_{exhaust}$ is the volumetric flow rate of the exhaust gases passing through the primary sampling tube. The particulate matter mass concentration in the exhaust line (M_{exh}) is related to the particulate matter mass concentration measured in the micro-dilution tunnel (M_{MDT}) by (eg. Vouitsis et al., 2003)

$$M_{exh} = D \cdot M_{MDT}. \tag{3.2}$$

An approximate measure of the uncertainty associated with the dilution ratio calculation was obtained by measuring the dilution ratio using an alternative method. This was done by comparing the volumetric dilution ratio measurement described above to a nonreacting gas concentration measurement. The dilution ratio is defined volumetrically and using nonreacting gas concentrations as

$$D = \frac{V_{mixture}}{V_{exhaust}} = \frac{[CO]_{exhaust}}{[CO]_{mixture}}. \tag{3.3}$$

The micro-dilution tunnel was set up as shown in Figure 3.3, using 1900 ppm CO (with balance of N_2) as simulated exhaust gas, and N_2 as the dilution gas. To measure the gas concentrations, the Eurotron Greenline 6000 was used, capable of measuring CO concentrations with an uncertainty of $\pm 4\%$. The exhaust gas CO concentration
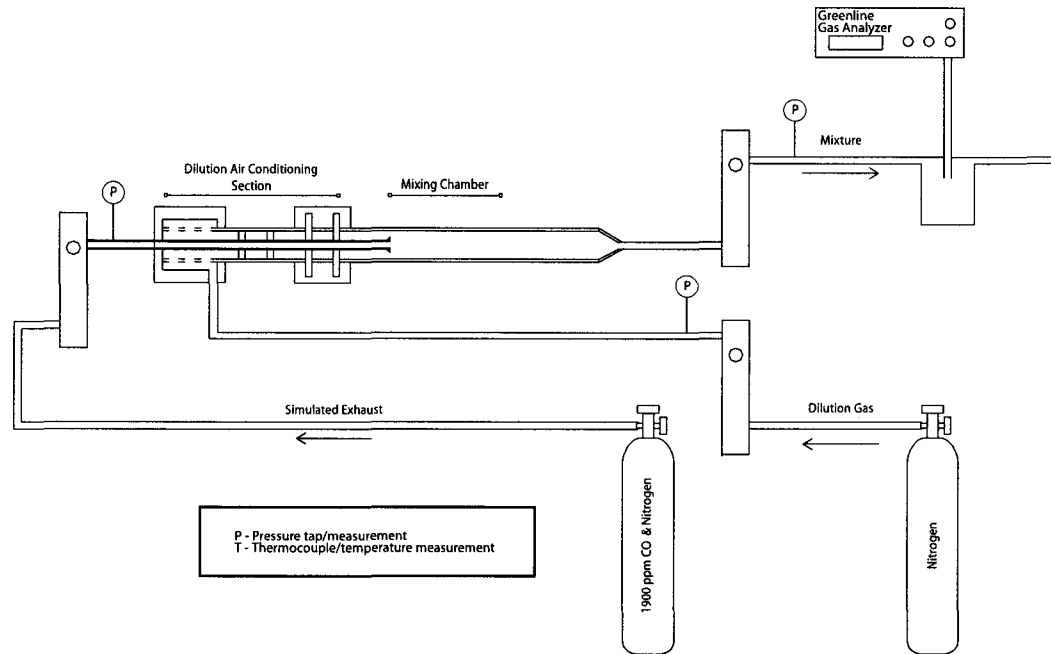
Figure 3.3: Micro-dilution tunnel set up for verification of dilution ratio using CO.

was measured by allowing the simulated exhaust to flow without any dilution gas. The dilution ratio was then controlled by varying the dilution gas flow rate. The dilution ratio was varied from about 10 to 20, and both volumetric and nonreacting gas concentration methods agreed to within 10%, as shown in Figure 3.4. Thus, the uncertainty of the dilution ratio calculation for exhaust flow rates used in this study was on the order of ±10%.
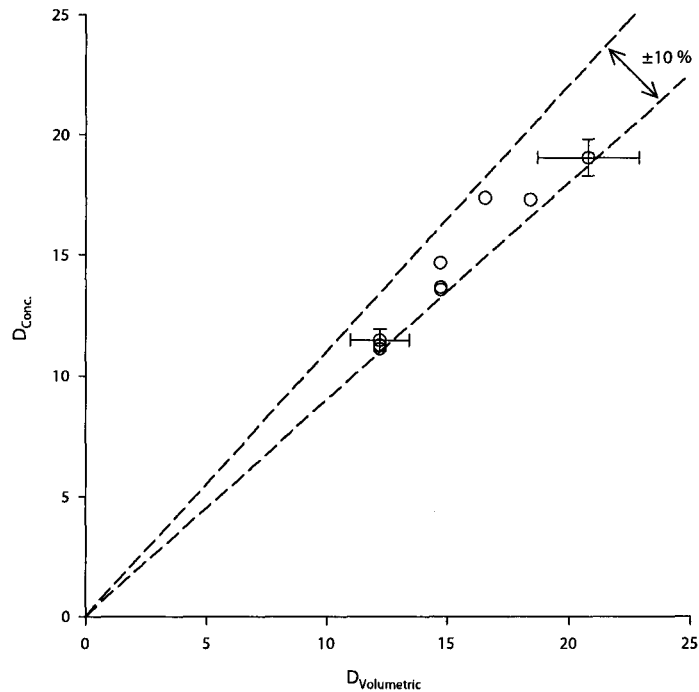
Figure 3.4: Comparison of dilution ratio determined by volumetric and nonreacting gas concentration methods.

3.2 Flow Separator

A schematic of the flow separator and electrostatic precipitator device is shown in Figure 3.5. A fully dimensioned illustration of the flow separator-type ESP is provided in Appendix A. The flow separator consists of a straight section of 1 1/4" (nominal) pipe with an inner diameter of 35.6 mm, with two identical 111 mm long perforated sections. There were 36 holes of 9.52 mm diameter, spaced evenly around the circumference of the pipe, as shown in Figure 3.6. The perforated sections were enclosed in 88 mm diameter pipes approximately 130 mm long. All components were made of stainless steel and grounded.

Branches connected two horizontally and symmetrically oriented electrostatic

ESP Dimensions (*length x diameter*): 61 cm x 6.3 cm
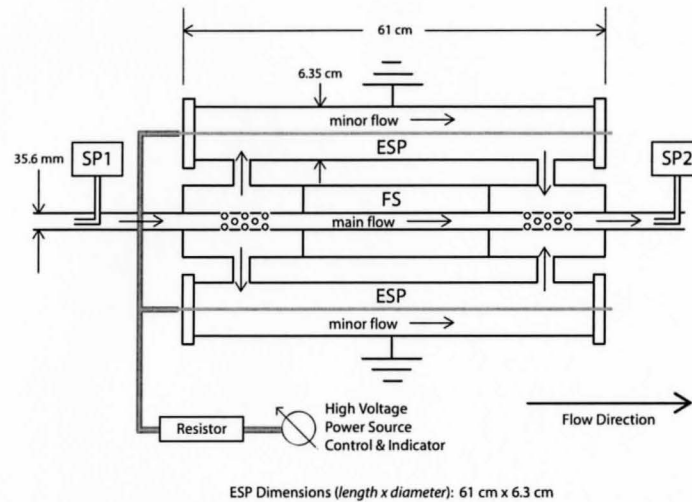
Figure 3.5: Flow-separator type electrostatic precipitator used in experiments

precipitators to the outer pipes. The ESP collection surface was constructed from stainless steel pipe with inner diameter of 6.35 cm inner diameter (2.5" nominal) and length of 61 cm (24"). The discharge electrode was made of 0.89 mm (0.035") diameter stainless steel wire, isolated from the collection electrode by 25.4 mm (1") thick teflon flanges at either end. A spring was used in line with the discharge electrode so that tension could be applied to the electrode. A compression fitting was used to fix the other end of the discharge electrode in place as shown in Figure 3.7. A variable high voltage power supply (Universal Voltronics Corp: $\pm$ 0 – 120 kV, 0 – 10 mA), with a 500 kΩ resistor in series, was used to apply the voltage to the ESPs. The resistor was used to limit the current to the ESPs in case of grounding or excessive sparking.

The flow separator divides the exhaust flow into two streams. The perforations in the main line of the flow separator allow a partial flow of exhaust gases and particulate matter to pass through the electrostatic precipitators. The remaining flow is the bypass flow. After passing through the ESPs, the minor flow rejoins the main flow through holes in the downstream part of the flow separator.

49
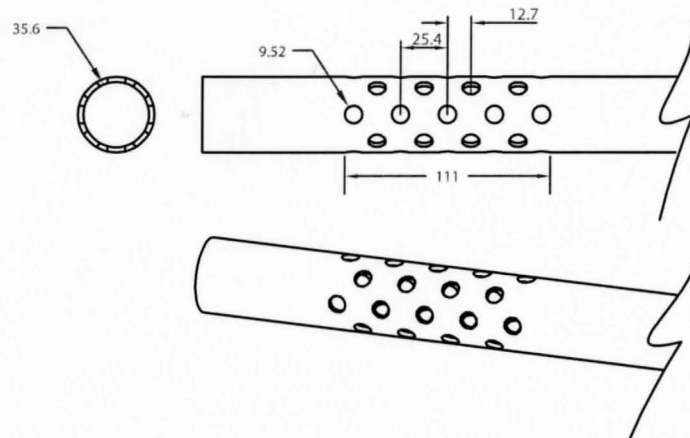
Figure 3.6: Hole spacing in the flow-separator. All dimensions in *mm*.
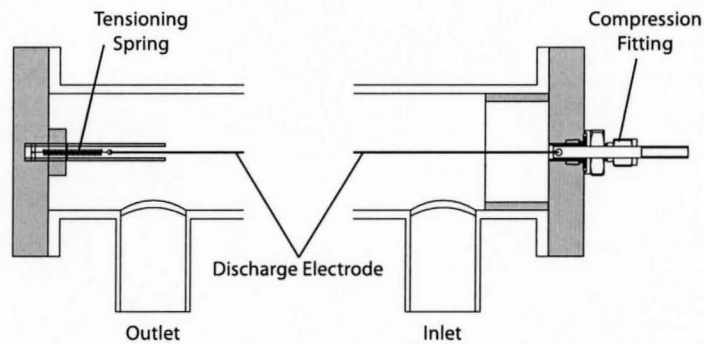
Figure 3.7: Retention and tensioning system for discharge electrode in ESP. Shaded areas are teflon.

Tests were initially performed to characterize the collection efficiency of the ESP by passing the total flow through the ESPs. This was done by removing the flow separator as shown in Figure 3.8(a). The collection efficiency of the FS-ESP system with straight inlet tubes was then characterized for different ESP voltages as shown in Figure 3.8 (b) . Tests were also performed with a modified FS-ESP, where the diameter of the branches connecting the flow separator to the ESPs were increased from 21 mm (3/4" nominal) to 35 mm (1 1/4" nominal), and an insert in the form

of a venturi was added just upstream of the holes in the main inlet pipe, shown in Figure 3.8 (c). A second insert was also added just downstream of the second set of perforations. Both inserts were of the same design, as shown in Figure 3.9, with area contraction ratio of 0.79. The inserts were located immediately upstream and downstream of the respective perforations in the separator, as illustrated in Figure A.2 in Appendix A.

The collection efficiency of the FS-ESP was evaluated by comparing particulate matter mass concentrations upstream (SP1) and downstream (SP2) of the device. The collection efficiency was given by

$$\eta_{ESP} = \frac{M_{SP1} - M_{SP2}}{M_{SP1}},$$

(3.4)

where M_{SP1} is the particulate matter mass concentration upstream of the device (in mg/m^3) and M_{SP2} is the particulate matter mass concentration downstream of the device. When the device is performing normally, this expression should result in positive, nonzero collection efficiencies even when no voltage is applied to the ESPs, due to deposition on the inner surfaces of the flow separator. In the early tests, PM mass concentrations were not measured continuously at the upstream sampling point. In these tests, the relative collection efficiency was evaluated using

$$\eta_{ESP} = \frac{M_{SP2}|_{0kV} - M_{SP2}}{M_{SP2}|_{0kV}},$$

(3.5)

where $M_{SP2}|_{0kV}$ is the particulate matter mass concentration at the downstream sampling location (SP2) with no voltage applied to the ESPs. This relative collection efficiency is a measure of the effect of voltage on the downstream emissions of the device.

Another measure of ESP effectiveness is the particle penetration. It is related

51

to the collection efficiency through the expression

$$\zeta_{ESP} = (1 - \eta_{ESP}) \cdot 100\%. \qquad (3.6)$$

This term is more commonly used in the ESP literature, whereas for particulate traps, the collection efficiency is reported. In the present work, the term collection efficiency will be used, though both measures will be provided in the figures.
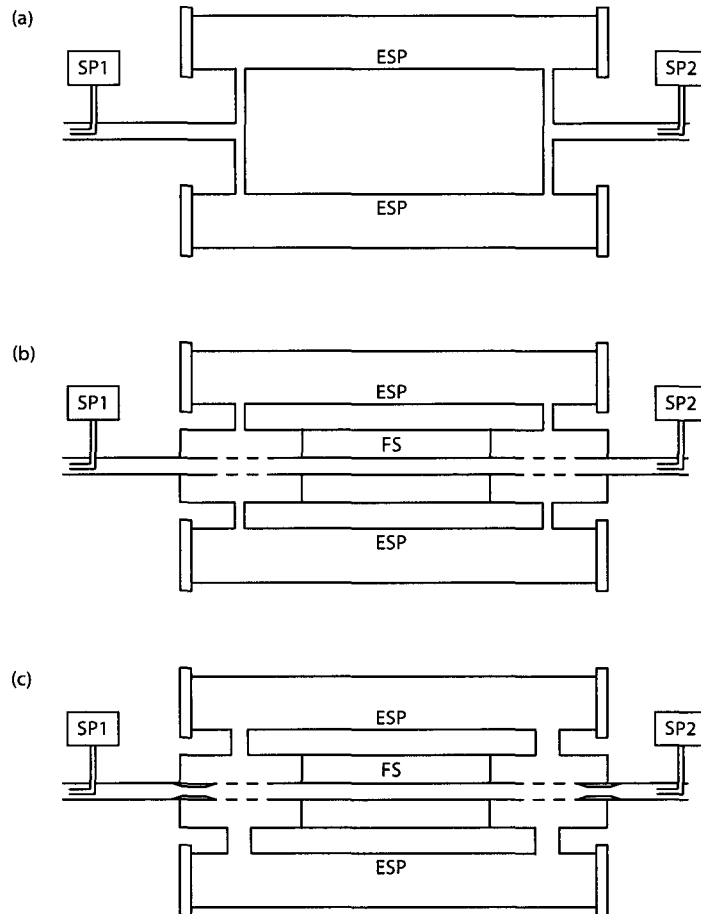
Figure 3.8: Comparison of the FS-ESP configurations tested: (a) ESP Only (3/4"
connecting branches); (b) Straight inlet FS-ESP configuration (3/4" connecting
branches); (c) Modified FS-ESP configuration (1 1/4" connecting branches and ven-
turis). Refer to Figures A.1 and A.2 for detailed dimensions.
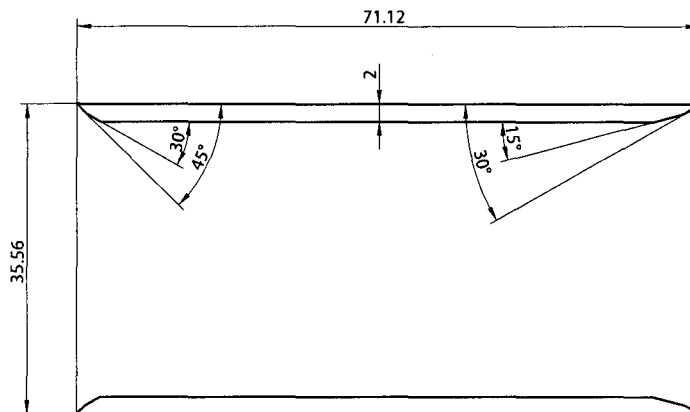
Figure 3.9: Schematic of the insert used for the modified FS-ESP. All measurements in mm.

3.3   Testing Methodology

The optical probe in the Haz-Dust III was cleaned, and then calibrated (zeroed only) prior to each test. The pressure transducers were also zeroed prior to testing. The engine was then started and was typically allowed to warm up for 2-3 minutes before the load was applied. Once the load was applied, the engine and main flow leg were allowed to warm up for an additional 90 minutes, at which point the temperature at V1 was steady. Prior to allowing flow through the test leg, voltage was applied (15 kV) to the ESPs to minimize particulate matter deposition on the discharge electrode. The valves to the test leg were then opened, and the valves were adjusted until the desired flow rate through the test leg was attained. Once the desired flow rate was obtained, the exhaust gas was sampled using the micro-dilution tunnel at the upstream (SP1) and downstream (SP2) sampling points. The test leg flow rate was monitored continuously, and minor adjustments were made to maintain the desired flow rate.

The dilution air flow rate was determined based on the desired dilution ratio, the sampling tube diameter, and the centreline velocity in the exhaust line. This was done by setting the velocity ratio

$$N_I = \frac{U_o}{U} \tag{3.7}$$

as close to unity as possible. The sampled exhaust gas flow rate was estimated by

$$V_{exh} = U_o A_p, \tag{3.8}$$

where A_p is the cross-sectional area of the primary sampling probe and U_o is the velocity of the gas entering the sampling probe. Here, it is assumed that a a negligible difference in exhaust line gas velocity exists across the small area of the sampling tube. The desired dilution air flow rate is then obtained by performing a mass balance on

the system, given by

$$\dot{m}_{exh} = \dot{m}_{total} - \dot{m}_d,$$ (3.9)

where $\dot{m}_{exh}$ is the sampled exhaust gas mass flow rate, $\dot{m}_{total}$ is the complete mixture mass flow rate, and $\dot{m}_d$ is the dilution air mass flow rate.

Velocity profiles were measured at the upstream (SP1) and downstream (SP2) sampling points at the flow rates used in this study to determine the nominal sampling velocity. The velocity profiles at SP1 and SP2 as well as the velocity profiles normalized by the average velocity are shown in Figure 3.10. Both sets of profiles have the appearance of a developing laminar velocity profile. At each sampling location, the normalized velocity profiles collapse well. This allows the use of a constant ratio of centerline (or sampling velocity) to average velocity ratio for each sampling location. The ratio of centerline to average velocity was 1.3 at the upstream sampling location (SP1), and 1.6 at the downstream sampling location (SP2).

Upon completion of a test, the rig was allowed to cool. The sampling lines between the exhaust flow leg and the dilution tunnel were removed and cleaned with detergent and a pipe cleaner. The sampling probes were left in place, and cleaned in the same manner. After each run, the ESPs were removed from the flow separator section. The end caps were removed, and the collection probe was inspected, then cleaned. The discharge electrode was also cleaned using detergent and steel wool. Prior to reassembly, it was ensured that the ESPs were dry, clean, and in good working order. Upon assembly, the ESPs were re-installed on the rig, and a current-voltage curve was obtained for the clean, room temperature case.
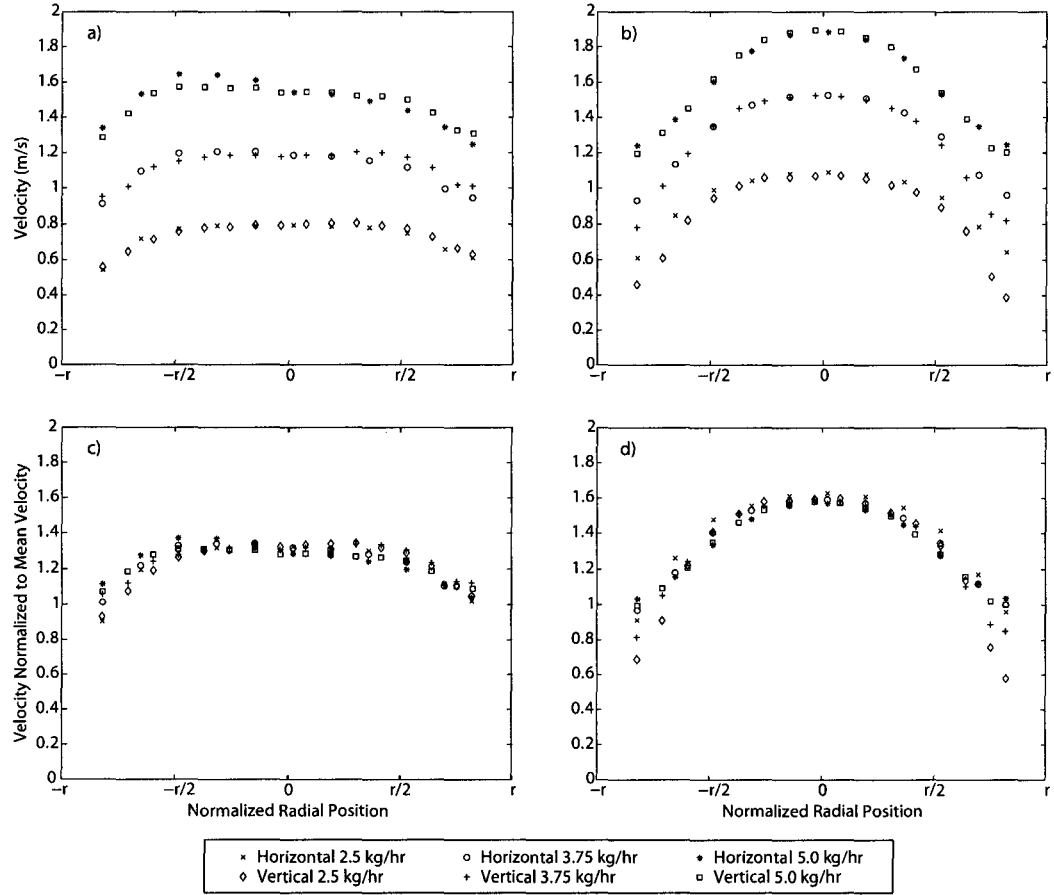
Figure 3.10: Gas-phase velocity profiles at upstream (SP1) and downstream (SP2) locations: a) SP1 velocity; b) SP2 velocity; c) SP1 normalized velocity; and d) SP2 normalized velocity.

3.4   Uncertainty Analysis and Data Reduction

The propagation of uncertainty was analyzed using the approach suggested by Kline and McClintock (1953). For a combination of i independent variables v_i with uncertainty w_i, the combined uncertainty of the result R is described by

$$w_R = \left[\left(\frac{\partial R}{\partial v_1} w_1 \right)^2 + \left(\frac{\partial R}{\partial v_2} w_2 \right)^2 + \cdots + \left(\frac{\partial R}{\partial v_n} w_n \right)^2 \right]^{1/2} . \tag{3.10}$$

Quantity	Range	Uncertainty
Exhaust mass flow rate (kg/hr)	0 – 40	±1%
Dilution ratio	~10	±10%
Particulate matter concentration (mg/m^3)	0 – 200	±12%

Table 3.4: Uncertainties associated with the key parameters measured in the present work.

A summary of the uncertainties associated with the calculations required in these experiments is given in Table 3.4. It was found that the calculation of the dilution ratio from the micro-dilution tunnel flow rates introduced the most uncertainty in the measurements. For a dilution ratio of 10, the reported 2.5% uncertainty in flow measurements resulted in an uncertainty of 34% using this technique. Extreme care was taken in reading the flow rates from the rotameters, and the flow rate was read at several times, in an effort to reduce random uncertainty. While bias error could not be eliminated, the rotameters were calibrated against each other prior to each experiment, and showed agreement to within 2.5%. The dilution ratio is shown to have an uncertainty of approximately ±10% by direct measurement.

The total uncertainty associated with particulate matter concentration in the micro-dilution tunnel, measured using the opacity meter (Haz-Dust III), is ±10% per reading. Random uncertainty was minimized by averaging several (60-200) seconds of data, which was recorded at 1 Hz. The uncertainty associated with the particulate matter mass concentration in the exhaust line was approximately ±12%.

Other constantly monitored parameters during testing include the exhaust flow rate in the test and bypass branches, the voltage supplied to the ESPs, and the current drawn by the ESPs. The venturis used in the test and bypass branches were recently calibrated to within ±1%, as described by Charles (2005). Typical uncertainty of the voltage and current from the high voltage power supply are shown in Table 3.5.

Measured Quantity	Range	Uncertainty	Uncertainty (%)
Voltage	0 – 10 kV	±0.2 kV	±2% of F.S.
Current	0 – 1 mA	±0.02 mA	±2% of F.S.
Current	1 – 3 mA	±0.06 mA	±2% of F.S.
Current	3 – 10 mA	±0.2 mA	±2% of F.S.

Table 3.5: Uncertainty associated with voltage and current measurements.

CHAPTER 4

RESULTS AND DISCUSSION

This chapter outlines the results of experiments performed with the prototype flow separator-type electrostatic precipitator (FS-ESP) system for control of diesel particulate matter. The particulate matter emissions from the diesel engine are characterized in the test leg first. Next, the performance of the electrostatic precipitators are characterized. Finally, the performance of the flow separator is examined in two configurations. The first configuration utilizes straight inlet tubes, while the second incorporates a contraction directly upstream of the perforations in the separator.

4.1   Characteristic Diesel Engine Emissions

The diesel particulate matter mass concentrations present at the sampling point upstream of the separator were quantified for exhaust flow rates of 2.5, 3.75 and 5 kg/hr, for an engine load of 1.5 kW, as shown in Figure 4.1. The particulate matter concentrations increased as the flow rate through the test leg decreased. For
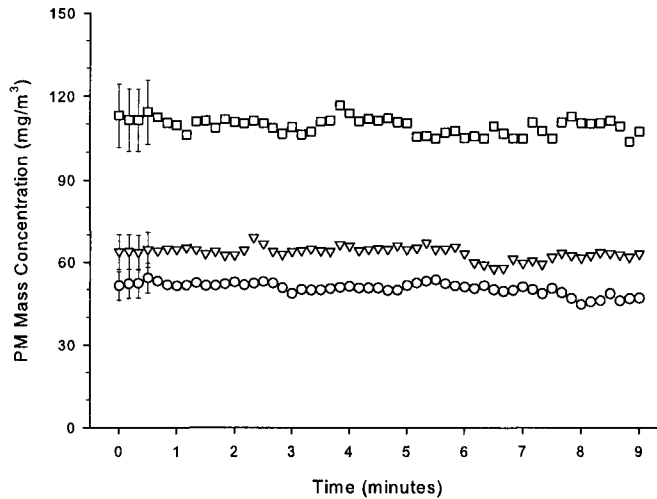
Figure 4.1: PM mass concentrations at SP1 for flow rates used in the present work: 5 kg/hr (○), 3.75 kg/hr (▽), 2.5 kg/hr (□).

the 2.5, 3.75 and 5.0 kg/hr flow rates, the particulate matter concentrations were approximately 110, 65 and 50 mg/m^3 with exhaust temperatures of 120, 130 and 140 °C, respectively. The data in this figure was obtained during a single test run (i.e. without stopping the engine) at a relatively constant temperature for each flow rate. Figure 4.2 shows that at an exhaust flow rate of 5 kg/hr, the mean particulate matter emission level remains relatively constant at about 50 mg/m^3, for a period of about an hour.

The different particulate matter mass concentrations at the different flow rates through the test leg were consistently observed even though engine conditions, and hence the PM concentration from the engine, were not changed. The increased particulate matter concentration measured in the test leg for the lower flow rates was likely due to increased phase separation at the tee, caused by larger particles crossing the gas phase streamlines due to their momentum. It is also probable that increased
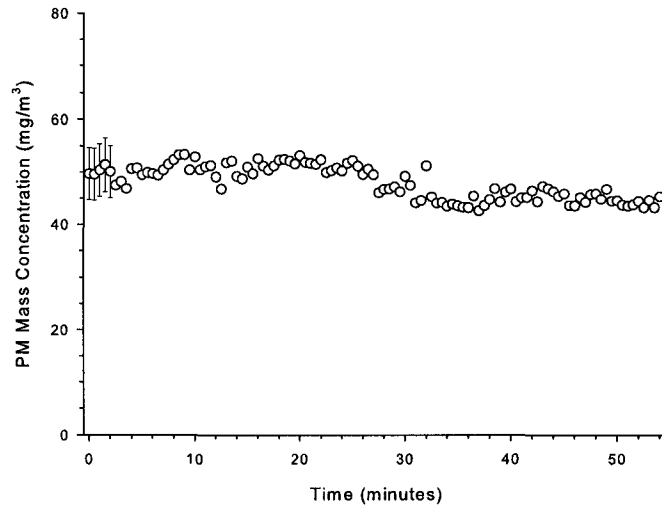
Figure 4.2: Variation of PM mass concentration at SP1 for 5 kg/hr exhaust flow rate.

particulate matter concentrations were observed because of increased condensation of sulphur species on the particulate matter in the exhaust line because the exhaust temperature decreased from 140 to 120 °C as the flow rate was reduced.

A preliminary characterization of the particle size distribution and number density is provided in Appendix C. The mean accumulation mode particle diameter was measured to be on the order of 0.1 μm, which is consistent with the literature.

4.1.1 Effect of Dilution and Sampling Velocity Ratios on Measured Particulate Matter Levels

The effect of dilution ratio on measured particulate matter concentration is shown in Figure 4.3, with a test leg flow rate of 5 kg/hr and engine load of 1.5 kW. The dilution ratio was raised and lowered from approximately 5 to 14 by increasing and decreasing the dilution air flow rate. The measured particulate matter concentration decreases as the dilution ratio is increased, similar to the observations
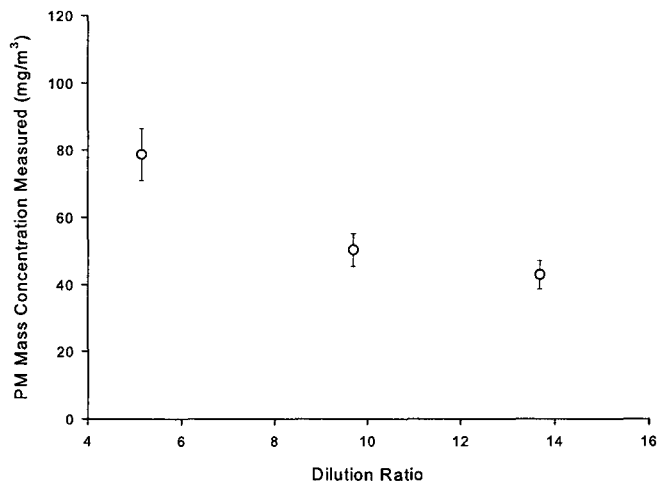
Figure 4.3: Effect of dilution ratio on measured particulate matter mass concentration.

of Reichel et al. (1983) and Frisch et al. (1979). For these three dilution ratios, the actual particulate matter concentration in the exhaust line is the same. The trend of decreasing measured particulate matter concentration with increased dilution ratio is likely explained by the lowering of the partial pressure of the soluble organic fraction (SOF). This results in a reduction of the saturation of the SOF, which adversely affects the rate of condensation of these species onto the existing particulate matter. Thus, at higher dilution ratios in this range, the particulate matter remains lighter, and the measured mass concentration is less. Further, the residence time of the sampled exhaust gases within the micro-dilution tunnel is decreased with increasing dilution ratio (because of the increased flow rate), which leaves less time for the SOF to condense on the existing particulate matter (Kittelson et al., 1999). Since dilution ratios typically range from 2 to 20 in laboratory studies, and this parameter can affect the measured particulate matter concentration, a dilution ratio of 10 was chosen and used in all tests to ensure consistency in this study.
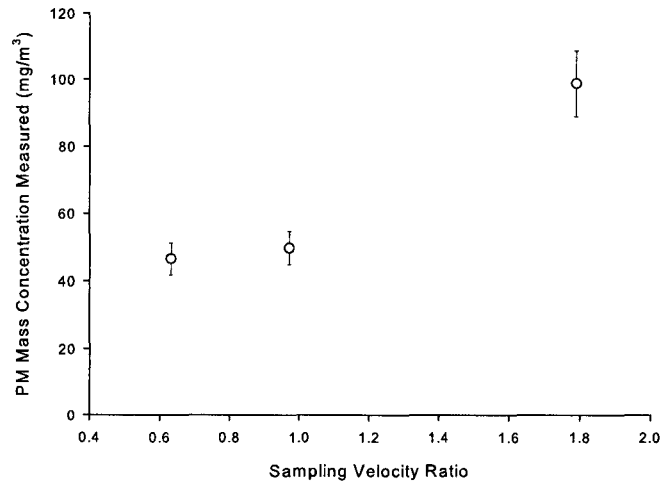
Figure 4.4: Effect of sampling velocity ratio on measured particulate matter mass concentration, with constant dilution ratio.

The effect of sampling velocity ratio ($N_I = U_o/U$) on measured particulate matter concentration is shown in Figure 4.4. This was done to evaluate the importance of sampling isokinetically, that is, with a sampling velocity ratio of unity. As the velocity ratio increases, the average velocity entering the sampling tube decreases, but the particulate matter concentration was observed to rise. This indicates that the larger particulate matter crossed the flow streamlines in the exhaust line to enter the primary sampling tube, causing oversampling of the heavier particulate matter despite undersampling of the exhaust gases. When the velocity ratio was about 0.6, the measured particulate matter concentration was only slightly reduced, but still within the uncertainty of the isokinetic measurement. This slight reduction could be caused by a reduced number of larger particles and an increased number of smaller particles that were drawn into the primary sampling tube. It was concluded from this test that a sampling velocity ratio of unity is desirable.

4.2   Performance of ESP

The time averaged discharge current for the clean electrostatic precipitators under no-flow, ambient conditions, is shown in Figure 4.5. For low applied voltages, there is no current, until the corona onset voltage is reached at approximately 12 kV. Beyond this point, the discharge current increases with applied voltage. Initially, there is a sharp increase in the current beyond the corona onset, and then increases quadratically with applied voltage. The scatter in the data is due to the uncertainty in the power supply voltage setting and current reading. The discharge current is stable until about 24 kV, at which point sparking occurs. Quadratic regression of this curve results in the expression

$$I/L = 0.0256V^2 - 0.318V, \tag{4.1}$$

for voltages between 13 kV and 24 kV, where I is the time averaged current (in mA) for a given applied voltage, V (in kV), consistent with the quadratic form of this equation expected by Equation 2.1.

The electrical operation and particulate matter collection performance of the electrostatic precipitators was characterized next under different applied voltages. For these tests, the ESPs were installed in the test leg so that the entire exhaust passed through the ESPs. The exhaust stream was split just upstream of the ESPs, with approximately half the flow rate passing through each ESP.

The current-voltage relationships of the ESPs with 2.5 and 5 kg/hr of exhaust flow are shown in Figure 4.6. The corona onset voltage was reduced to about 5 kV (2.5 kg/hr) and 6 kV (5.0 kg/hr), and the rate of increase of current with increased voltage was reduced in these cases compared to the room temperature air case. The increased temperature of the exhaust gas compared to the air at room temperature reduces the ionic density of the gas between the ESP electrodes, facilitating corona
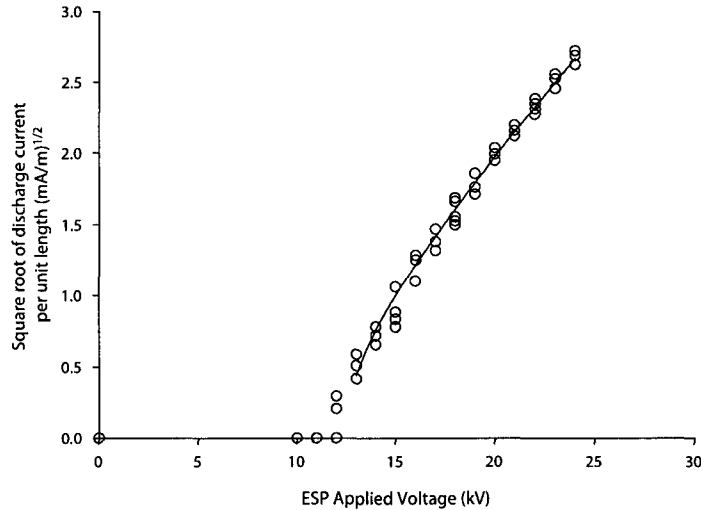
Figure 4.5: Typical clean ESP current-voltage characteristics at room temperature with no flow. (○) measured values; (—) linear regression of data ($I/L = 0.0256V^2 - 0.318V$).

discharge at the lower voltage. The increased flow rate tends to increase the corona onset voltage and reduce the rate of current increase with voltage. These temperature and flow rate effects agree quantitatively with those observed in the literature. In this configuration, operation of the ESPs was not possible above 20 kV due to electrical instabilities caused by uneven discharge and sparking. There was little difference between the current-voltage characteristics at 2.5 and 5.0 kg/hr, except for a slight increase in slope of the curve for the higher flow rate case.

The particulate matter collection performance of the ESPs was characterized by measuring particulate mass concentration at the downstream sampling location (SP2). The change in the particulate matter concentration at the exit of the ESPs is shown in Figure 4.7 for the 2.5 kg/hr exhaust flow rate. The relative collection efficiency of the combined ESPs, determined using Equation 3.5 and $M_{SP2}|_{0kV}$ as the reference value, is also shown in this figure. As the voltage is increased from
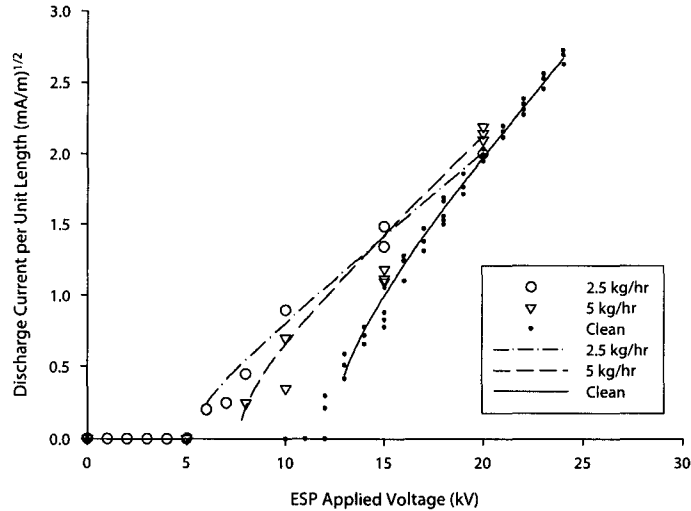
Figure 4.6: Typical ESP current-voltage operating curves for 2.5 and 5.0 kg/hr exhaust flow rates.

0 kV, the downstream particulate matter levels are reduced, even before the ESP draws any power (eg. at voltages where no current is drawn by the ESPs). This is possible because it is the electric field that imparts the electrophoretic force on the particulate matter. The particulate matter has a small charge before entering the ESPs, even without charging by the corona discharge. At the 5 kV corona onset voltage, the particulate matter concentration at the downstream sampling location is on the order of 50 mg/m^3, corresponding to a relative collection efficiency of 60 – 80%. The collection efficiency quickly rises to 99% at approximately 8 kV applied voltage, with only trace levels of particulate matter measured. This increase in collection efficiency is due the combined effects of increased electric field and increased particle charging.

The particulate matter emissions and relative collection efficiency of the combined ESPs for the 5.0 kg/hr exhaust flow rate are shown in Figure 4.8. The particulate matter concentration was reduced to about 35 – 60 mg/m^3 at the corona

onset voltage of approximately 5 kV, corresponding to a relative collection efficiency of about 40%. Increasing the applied voltage from the corona onset voltage resulted in a steady decrease in downstream particulate matter mass concentration, with near-zero particulate matter concentrations corresponding to relative collection efficiencies on the order of 99% at 20 kV applied voltage. The increase of exhaust flow rate from 2.5 to 5.0 kg/hr has the effect of reducing the collection efficiency at a given applied voltage, as well as increasing the required voltage to precipitate nearly all of the particulate matter.

These results demonstrate that the ESPs effectively removed the PM for flow rates of 2.5 kg/hr and 5 kg/hr flow rates, but suggests that the particulate matter collection efficiency will be reduced as the mass flow rate is increased beyond a certain level. This was observed, for example, when the exhaust flow rate was increased to 10 kg/hr through the ESPs. There was electrical instability due to sparking that did not permit operation at this flow rate, even at low voltages. Thus, no data can be reported for the 10 kg/hr flow rate. The degradation in performance with increased flow rate is likely due to a combination of several effects. The decreased residence time within the ESP and the increased particulate matter flow rate both tend to reduce the effectiveness of particle collection in the ESPs. Fluid dynamic effects such as EHD and flow induced vibration of the discharge electrode as well as particulate matter deposition/scrubbing at the inlet section result in electrical instabilities, which also degrade the performance of the ESPs. These mechanisms are affected by EHD induced secondary flows, which may act to improve or degrade the ESP performance. Figure 4.9 shows the relative strength of the EHD forces to the convective forces (Ehd/Re^2, calculated in terms of the collection electrode diameter) as a function of V/d within the ESP. The electric field strength is directly related to the applied voltage. The results show that the EHD induced secondary flows may be significant

68

at the flow rates tested, however it is difficult to ascertain the role they play in terms of collection efficiency improvement or reduction.

The flow of the gas and particle phases in the ESP play a significant role in the performance of the ESPs, though the details of this flow are not known. In an effort to gain some insight into the dynamics within the ESPs in this configuration, maps of the deposition of PM on the collection electrode were made following each experiment. These are included for reference in Appendix D.

Figure 4.7: (a) ESP SP2 particulate matter emissions as a function of applied voltage, and (b) ESP collection efficiency relative to SP2 no-voltage emissions, for the 2.5 kg/hr exhaust flow rate.
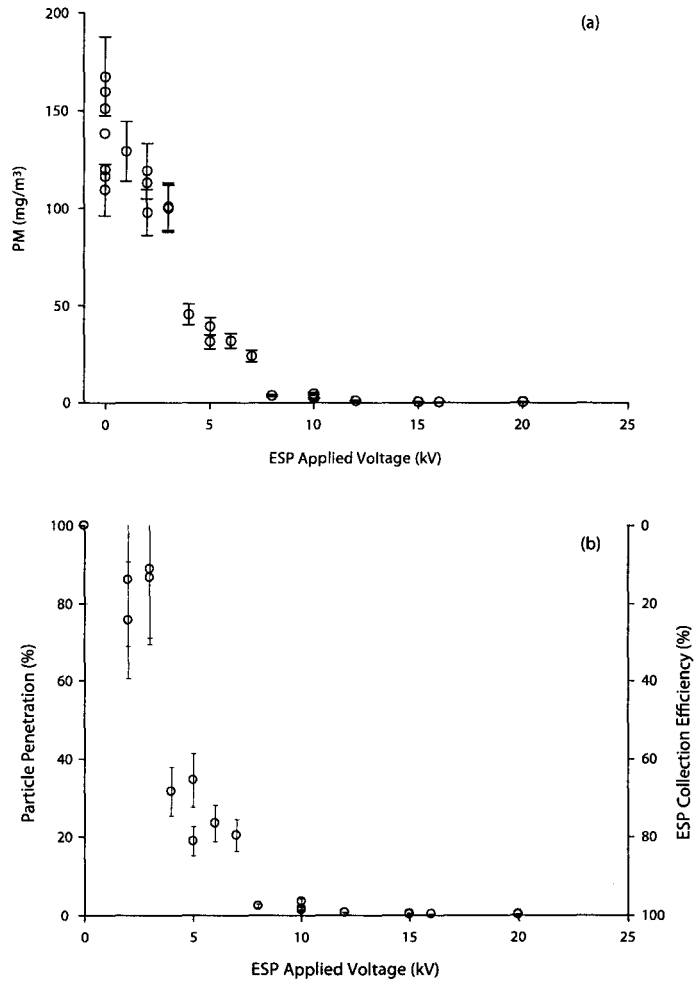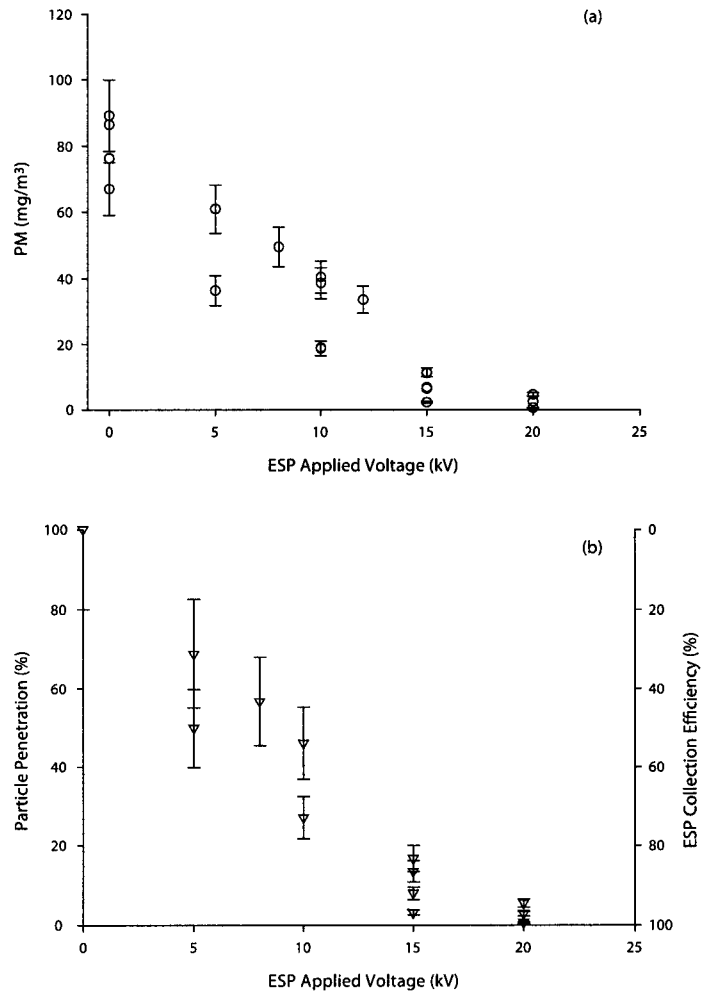
Figure 4.8: (a) ESP SP2 particulate matter emissions as a function of applied voltage, and (b) ESP collection efficiency relative to SP2 no-voltage emissions, for the 5.0 kg/hr exhaust flow rate.
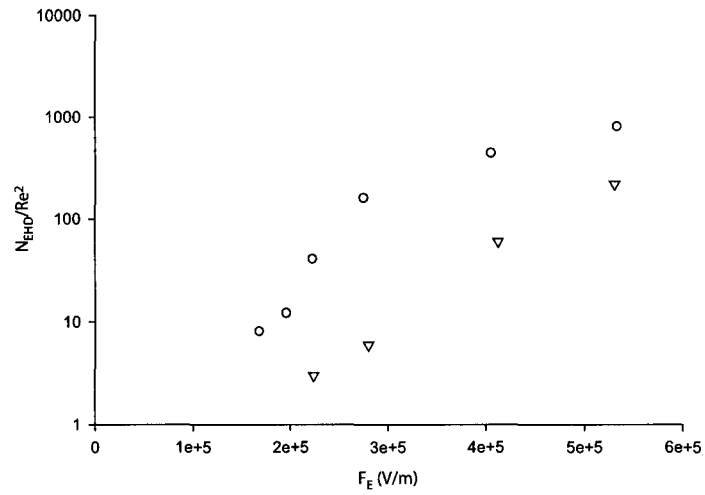
Figure 4.9: Ehd/Re^2 within the ESPs for ($\circ$) 2.5 kg/hr and (∇) 5.0 kg/hr exhaust flow rates.

4.3   Performance of Flow Separator-Type ESP

The flow separator with the straight inlet tube was installed on the test rig and was tested with exhaust flow rates of 2.5 kg/hr and 5.0 kg/hr. The pressure drop across the FS-ESP in this configuration, measured with a water manometer, was less than 25 Pa (0.1" H_2O) for both flow rates. The particulate matter mass collection efficiency of the FS-ESP in this configuration is presented in Figures 4.10 and 4.11 for exhaust flow rates of 2.5 kg/hr and 5 kg/hr, respectively. The relative collection efficiency was computed using the outlet PM levels at 0 kV as the reference value. The collection efficiencies at exhaust flow rates of 2.5 kg/hr were slightly higher than those observed at 5 kg/hr. Neither flow rate resulted in significant collection efficiencies, with the maximum collection efficiency on the order of 30%. Examination of the flow separator used by Harvel et al. (2004) provided some insight as to why there was such a low collection efficiency in this configuration. The major geometric difference between the FS-ESP in that study and the one used here was that there was a contraction just upstream of the perforations. This difference may have had a significant effect on the phase separation, as it was thought that the sudden expansion at the perforated section caused particle stagnation, allowing migration of the particulate matter to the ESP section by diffusion and convection. Accordingly, the flow separator was modified to incorporate a small contraction upstream of the perforations.

The collection efficiency of the modified FS-ESP was examined next. The upstream (SP1) particulate matter concentration was about 120 mg/m^3 in this test. The downstream (SP2) particulate matter concentrations are illustrated in Figure 4.12 for this case, at the ESP voltages tested. In this case, both the absolute and relative collection efficiencies are presented in Figures 4.13 – 4.15 for comparison. The absolute collection efficiency uses the upstream particulate mass concentration (at SP1) as a datum. The relative and absolute collection efficiencies of the modified FS-ESP for
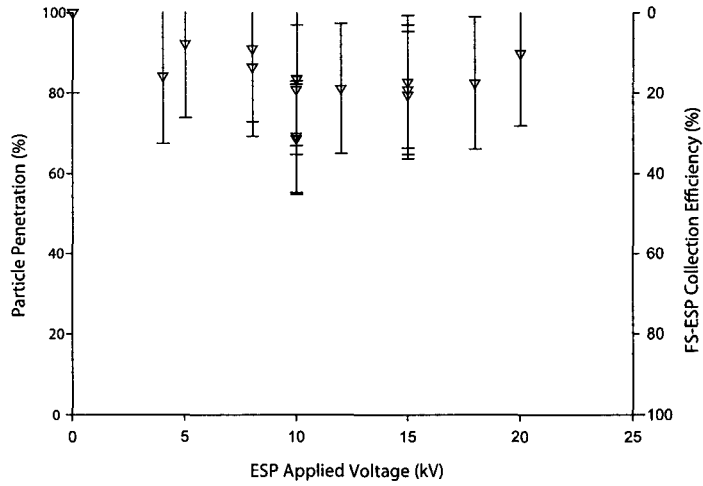
Figure 4.10: FS-ESP with straight inlet relative collection efficiency based on SP2 no-voltage emissions for the 2.5 kg/hr exhaust flow rate.
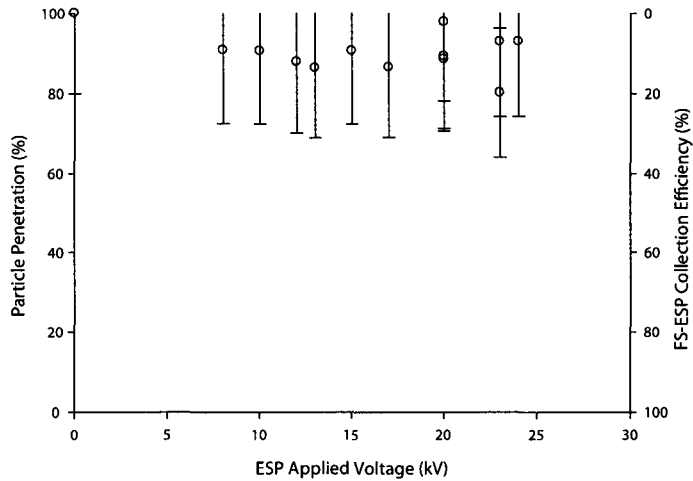
Figure 4.11: FS-ESP with straight inlet relative collection efficiency based on SP2 no-voltage emissions for the 5 kg/hr exhaust flow rate.

74
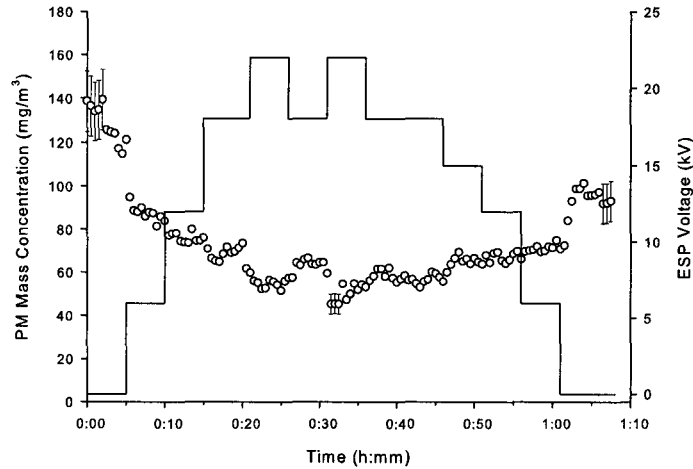
Figure 4.12: Transient PM mass concentration at various ESP voltages, at the down-stream sampling location (FS-ESP with insert, 2.5 kg/hr exhaust flow rate): (o) PM mass concentration, (——) ESP Voltage.

the 2.5 kg/hr exhaust flow rate case are shown in Figure 4.13. The collection efficiencies in this case were improved significantly, with a maximum collection efficiency on the order of 60%, compared to 30% for the straight inlet FS-ESP configuration. This suggests that either 60% of the exhaust flow passed through the ESPs, or that phase separation occurred. The latter is more likely, and will be discussed below. The Reynolds number of the inlet flow, based on the exhaust line diameter and average gas velocity, was approximately 1100. The collection efficiency was observed to increase with applied ESP voltage.

The results for an exhaust flow rate of 3.75 kg/hr are shown in Figure 4.14. In this case, the Reynolds number at the FS-ESP inlet was approximately 1600. This flow rate resulted in low collection efficiencies on the order of 20 %, similar to those obtained with the original FS-ESP configuration at this flow rate. The insert had little or no effect with this increased flow rate. This was also true for a mass flow of 5

Figure 4.13: FS-ESP with insert (a) relative collection efficiency based on SP2 no-voltage emissions, and (b) absolute collection efficiency, for the 2.5 kg/hr exhaust flow rate.

kg/hr, as shown in Figure 4.15. Here, the inlet Reynolds number was approximately 2100. In both the 3.75 kg/hr and 5.0 kg/hr exhaust flow rate cases, there was little correlation between collection efficiency and ESP applied voltage.

Comparing the relative collection efficiency to the absolute collection efficiency (part (a) to part (b) in Figures 4.13 – 4.15) indicates that deposition within the flow separator is negligible compared to the ESP collection efficiency at voltages above the corona onset. Therefore, the use of the relative collection efficiency is adequate for evaluation of this device at moderate to high voltages, even though the absolute collection efficiency is more correct.

The characteristic electrical operating curve of the ESPs is shown in Figure 4.16 for the modified FS-ESP configuration. The electrical operating curves are hardly affected by the flow of the exhaust gases. The corona onset voltage appears to shift to about 9 – 12 kV. The electrical characteristics of the ESPs in the FS-ESP with the straight entrance region were recorded, but malfunction of the current meter required this data to be discarded. The pressure drop across the modified FS-ESP, measured with a water manometer, was also less than 25 Pa (0.1" H_2O) for all flow rates.
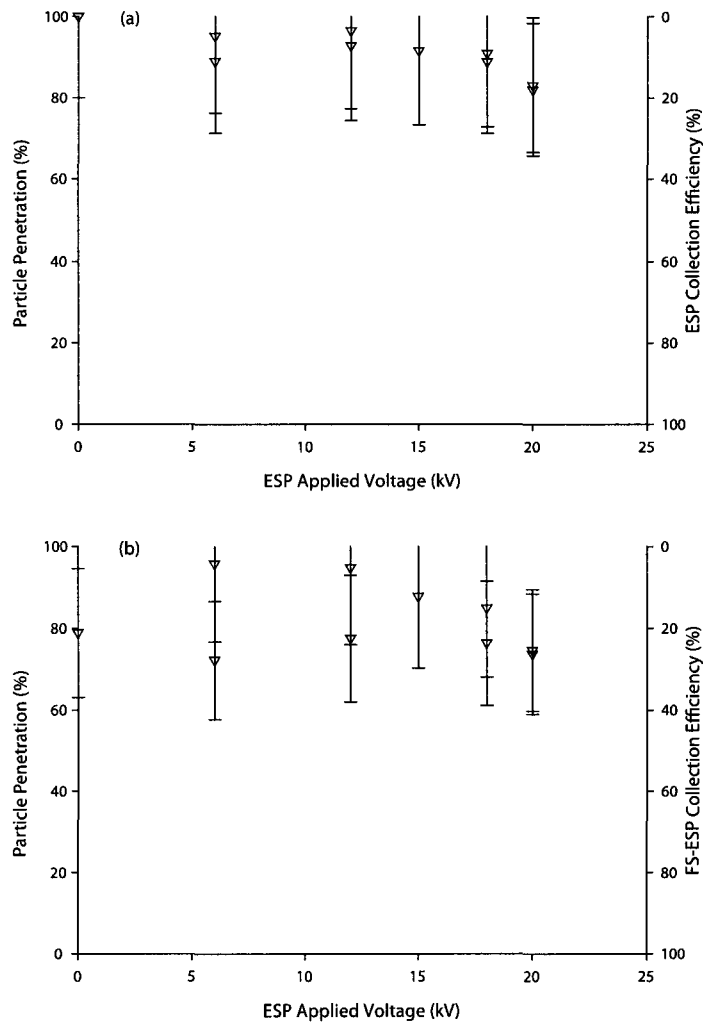
Figure 4.14: FS-ESP with insert (a) relative collection efficiency based on SP2 no-voltage emissions, and (b) absolute collection efficiency, for the 3.75 kg/hr exhaust flow rate.
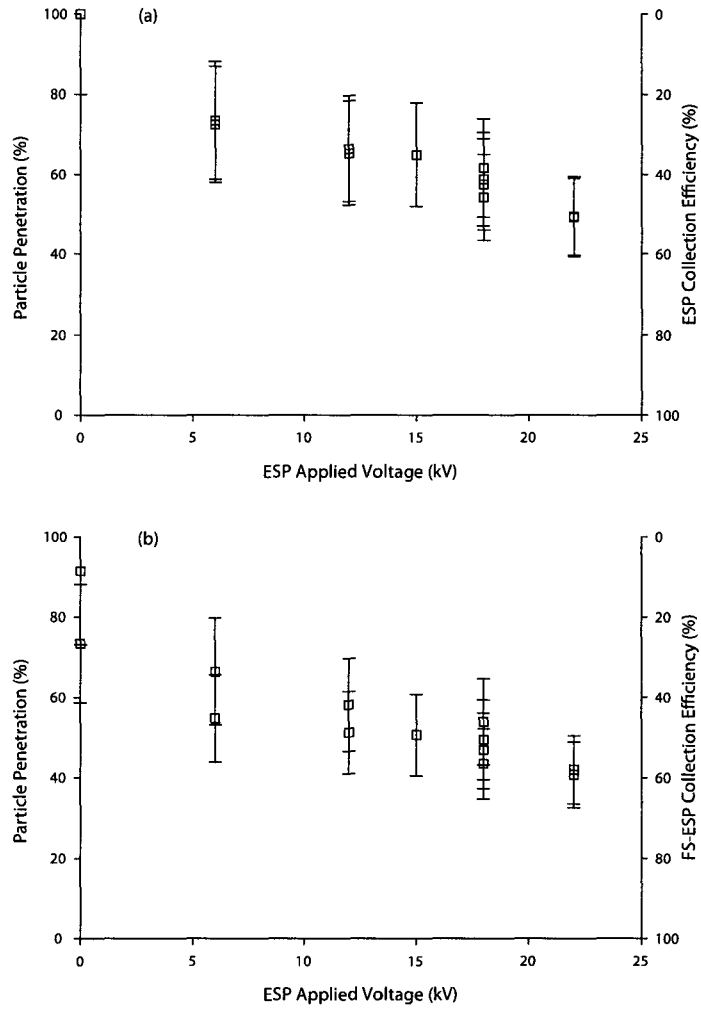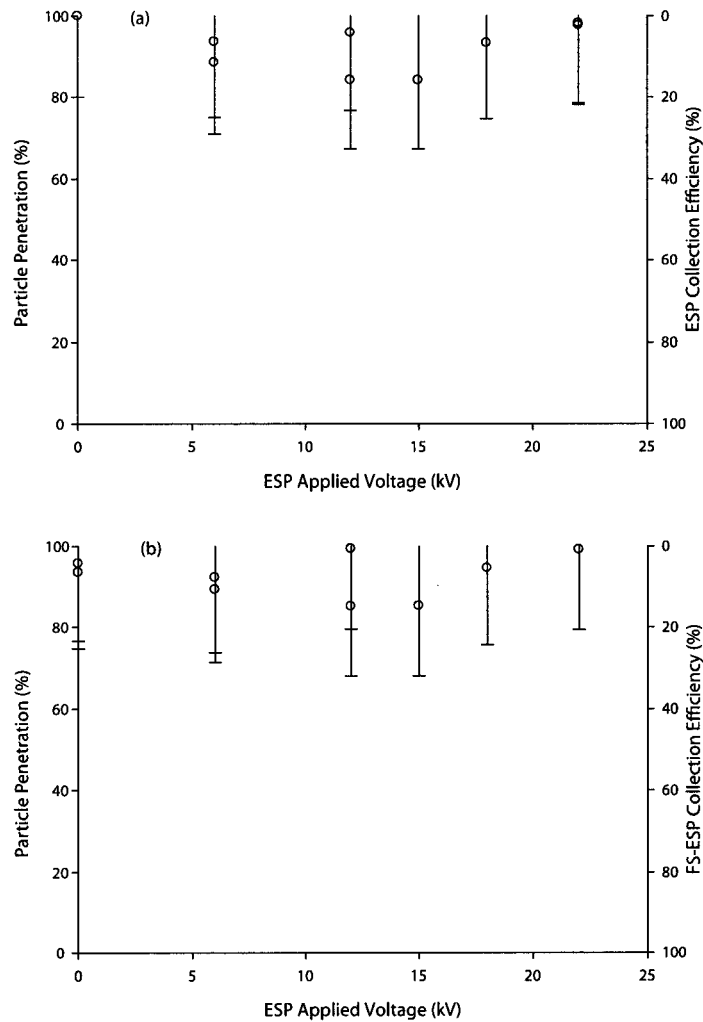
Figure 4.15: FS-ESP with insert (a) relative collection efficiency based on SP2 no-voltage emissions, and (b) absolute collection efficiency, for the 5.0 kg/hr exhaust flow rate.
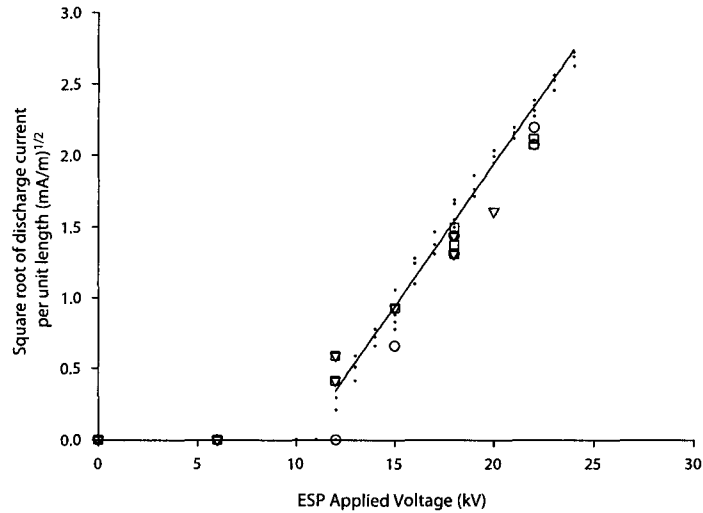
Figure 4.16: Combined ESP I-V characteristics for the clean, no flow, room temperature case ($\cdot$), the 2.5 kg/hr case ($\square$), the 3.75 kg/hr case (∇), and the 5 kg/hr case ($\circ$).

4.4   Discussion

The term 'flow separation' is used to quantify the amount of flow that is diverted through the ESP branches. An analysis of pressure drops associated with each component of the FS-ESP device was performed to estimate the amount of flow separation. Figure 4.17 illustrates the location of each pressure drop component used in the model. Table 4.1 details the major losses associated with friction in the straight pipe sections, with the exception of the flow through the inserts, which are combinations of a contraction, a straight pipe flow, and an expansion flow. Table 4.2 outlines the minor losses associated with bends, contractions and expansions. Correlations presented by Fox and McDonald (1998) were used in these calculations. The major pressure losses associated with flow through the straight, round pipe was modeled using

$$h_l = f \frac{L}{D} \frac{\bar{V}^2}{2},$$ (4.2)
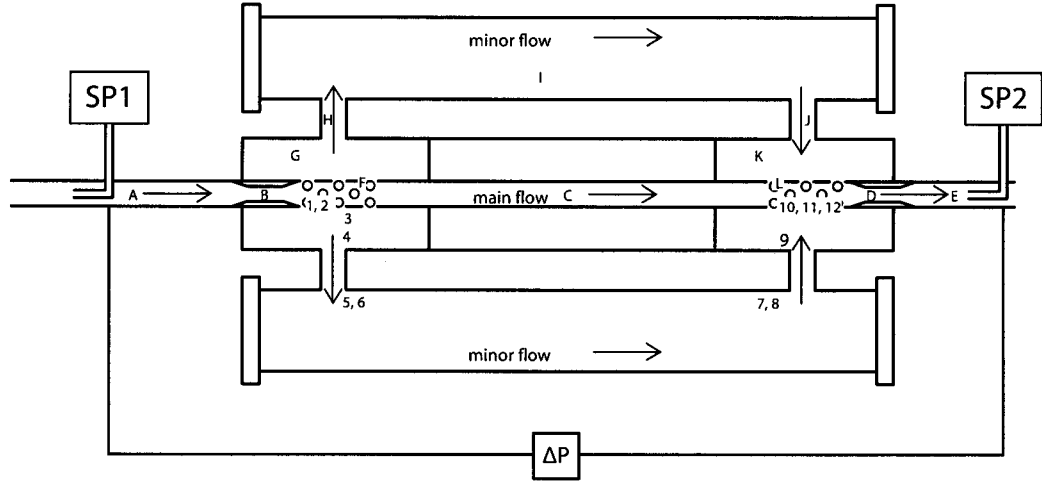
Figure 4.17: Major (A–L) and minor (1–12) losses modeled in FS-ESP system.

where h_l is the head loss, L is the length of the section, $\bar{V}^2$ is the average velocity of the gas in the section, D is the diameter of the section, and f is the friction factor. For laminar flow,

$$f_{\text{laminar}} = \frac{64}{\text{Re}} \tag{4.3}$$

was used, and for turbulent flow, the Blasius correlation was used. Minor losses were modeled using the coefficients presented by Fox and McDonald (1998), of the form

$$h_{l_m} = K\frac{\bar{V}^2}{2} = f\frac{L_e}{D}\frac{\bar{V}^2}{2}, \tag{4.4}$$

where h_{l_m} are the minor head losses, K is the loss coefficient, and L_e is an equivalent length of straight pipe. The head loss is related to the pressure drop using the energy balance,

$$\frac{\Delta P}{\rho} = \sum h_l + \sum h_{l_m}, \tag{4.5}$$

where ΔP is the pressure drop.

h_l	Description
A	Flow through approach section
B	Flow through insert
C	Flow through middle section
D	Flow through downstream insert
E	Flow through end section
F	Flow through upstream perforations
G	Flow through annular chamber
H	Flow through upstream connecting branch
I	Flow through ESP branch
J	Flow through downstream connecting branch
K	Flow through annular chamber
L	Flow through downstream perforations

Table 4.1: Major losses (h_l) in FS-ESP.

h_{lm}	Description	Equivalent length (L_e/d) or Loss factor (k)
1	Miter bend, 90°	$L_e/d = 60$
2	Square-edged entrance	$k = 0.5$
3	Sudden expansion	$k = 1.0$
4	Square-edged entrance	$k = 0.5$
5	Sudden expansion	$k = 1.0$
6	Miter bend, 90°	$L_e/d = 60$
7	Miter bend, 90°	$L_e/d = 60$
8	Square-edged entrance	$k = 0.5$
9	Sudden expansion	$k = 1.0$
10	Square-edged entrance	$k = 0.5$
11	Sudden expansion	$k = 1.0$
12	Miter bend, 90°	$L_e/d = 60$

Table 4.2: Minor losses (h_{lm}) in ESP branch.

The pressure drop in the ESP branches was modeled as

$$h_{\text{ESPBranch}} = \sum_{i=F}^{L} h_l^i + \sum_{i=1}^{12} h_{l_m}^i, \qquad (4.6)$$

where $\sum_{i=F}^{L} h_l^i$ is the sum of the major losses and $\sum_{i=1}^{12} h_{l_m}^i$ is the sum of the minor losses,

using the indices outlined in Tables 4.1 and 4.2. This was balanced with the pressure drop of the central tube by manually adjusting the flow separation ratio.

A pressure drop test was performed by passing clean air through the FS-ESP with the inserts and larger diameter ESP connecting branches. Results from this test are compared with the model results in Figure 4.18. The pressure drop across the FS-ESP was measured to within ± 2.5 Pa using an inclined oil manometer. Quadratic regression of the experimental data results in the curve shown in Figure 4.18(a), which is qualitatively and quantitatively consistent with the model predictions. The model predicts the pressure drop to within $\pm 20\%$ at Reynolds numbers greater than 8000. At lower Re, the accuracy of the prediction is not as good, however, this is likely due to the relatively high uncertainty in the pressure drop measurements at these flow rates. The dimensionless pressure drop, or pressure coefficient ($C_p = \Delta P/(\frac{1}{2}\rho \bar{V}^2)$), is shown in Figure 4.18 (c) and (d) for the experiment and the model, respectively. The predicted C_p is less than the experimental observations, but still the same order of magnitude and following a similar trend. The model did not consider the partial constrictions of the sampling tubes upstream and downstream of the device, and may contribute to the lower values predicted by it. The model is quite rudimentary, however, these results indicate that it may be reasonably used for rough estimations of flow characteristics through the FS-ESP.

Figure 4.19 shows the percentage of exhaust gas that flows through the central bypass tube of the FS-ESP, as predicted by the pressure drop model. It shows that the increased ESP branch diameter (from 21 to 35 mm) allows more flow through the ESPs, but the difference is only on the order of 1% of the mass flow. For the flow rates examined experimentally, about 90 – 93% of the flow remains in the FS-ESP central bypass tube. This means that approximately 3.5 – 5% of the exhaust gases (by mass) pass through each ESP. The model was used to evaluate the pressure drop
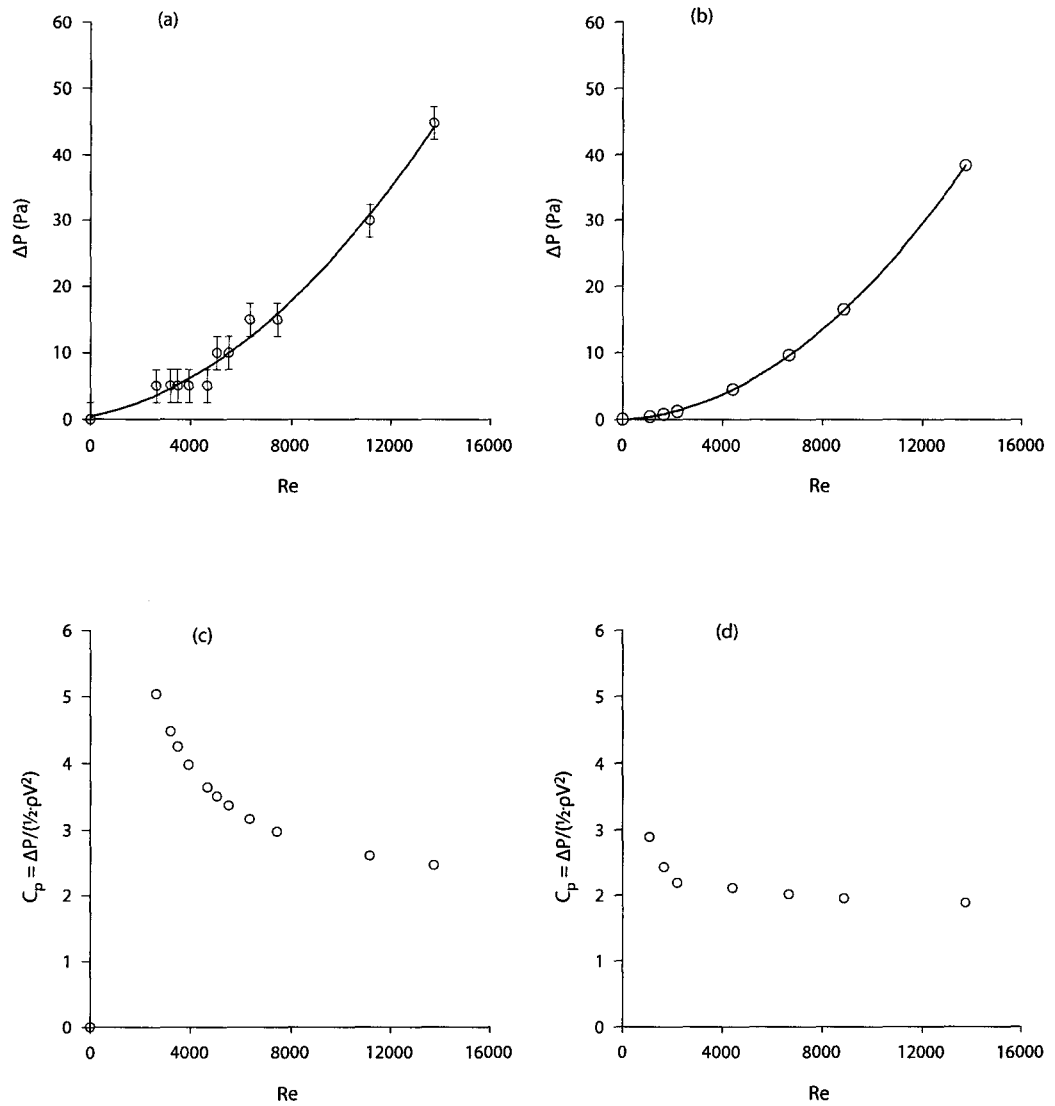
Figure 4.18: Comparison of pressure drop between experiment (a and c) and model (b and d).
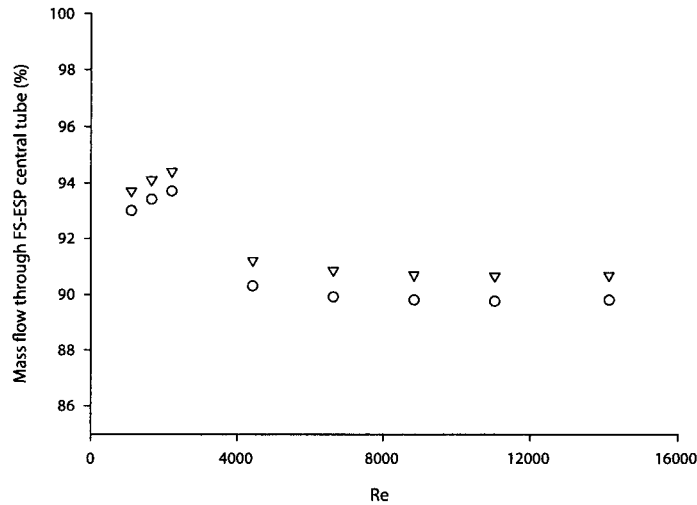
Figure 4.19: Predicted mass flow rate through FS-ESP central pipe with 35 mm branches (∘) and 21 mm branches (∇).

and flow separation for the cases with and without the inserts. The inserts have the effect of increasing the overall pressure drop by approximately 30 – 60% for upstream Reynolds numbers of 1100 – 14000. This model is incapable of elucidating the effect of the upstream insert on the flow separation, if there is any.

As stated above, 3.5 – 5% of the mass flow rate of the exhaust gases is diverted to each of the two ESP branches at the flow rates examined in the present work. Despite the simplifying assumptions used in this technique, this flow separation is similar to the 97 – 98% separation determined by experimental and numerical techniques by Harvel et al. (2004). The observation that the ESP operating curve was hardly affected when gas was allowed to flow through them in the FS-ESP configuration is consistent with the very low flow rates through the ESP branches.

A measure of the effectiveness of the flow separator-ESP device is the amount of separation of the solid, particulate matter phase from the gaseous phase. It was shown that the FS-ESP with the insert was capable of achieving 60% collection efficiency

at an exhaust flow rate of 2.5 kg/hr, indicating that 60% of the particulate mass was separated from the main exhaust flow and convected through the ESPs by 7 − 10% of the gaseous flow. The mechanism of this phase separation is not completely understood, but could perhaps be explained as follows. When the gas stream enters the perforated section, the effective cross section of the passage is increased. Here, the velocity of the gas stream is reduced. In this region of slow-moving, almost stagnant gas, the motion of the particulate matter is no longer dominated by the convective force. The particulate matter then travels towards the perforations by diffusion and thermophoresis, due to the lower particulate matter concentration on the outside of the perforated section, and the lower temperatures in that region. The addition of the insert has the effect of amplifying this effect, because the amount of expansion is enhanced. Increased Reynolds number of the flow at the separator would tend to reduce the effectiveness of this mechanism, because the particulate matter is given more inertia, which tends to drive it in the axial direction. The flow pattern created by the contraction installed upstream of the perforations, and its interaction with the small amount of flow through the perforations, could also play an increased role as the Reynolds number is increased. The length of a recirculation zone formed behind the contraction would tend to increase with Reynolds number, which could act to prevent the particulate matter from passing through the perforations.

In contrast to the results obtained in the present work, the performance of the FS-ESP in the study by Harvel et al. (2004) also had a Reynolds number dependance, but showing improved phase separation with increasing Reynolds number. The Reynolds numbers of the flows in that study were 1640 − 3110 just upstream of the perforations, but the size distribution of the particulate matter was an order of magnitude smaller. The smaller diameter of the aerosol tends to favour the diffusive and thermophoretic transport mechanisms, aiding in phase separation. The

inlet of the separator had a slightly different geometry in that study, which could be responsible for the divergence of these two results.

CHAPTER 5

CONCLUSIONS AND

RECOMMENDATIONS

5.1   Conclusions

Experiments were performed to characterize a particulate matter separator combined with electrostatic precipitators for removal of particulate matter from diesel engine exhaust. Particulate matter mass was measured using a micro-dilution tunnel and an optical mass measurement device. First, the particulate matter mass concentrations were characterized for three test leg flow rates. Next, three configurations of the device were tested on the diesel engine test cell: the electrostatic precipitators without the flow separator, the flow separator with a straight inlet section combined with electrostatic precipitators, and a modified flow separator with electrostatic precipitators. Performance of the devices was evaluated primarily in terms of particulate matter mass collection efficiency. The relative and absolute collection efficiencies were

calculated, where possible.

The particulate matter mass concentrations in the test leg for 2.5, 3.75, and 5.0 kg/hr exhaust flow rates were about 110, 65, and 50 mg/m^3, while the exhaust temperature was 120, 130, and 140 °C, respectively. The different PM concentrations measured in the test leg were likely due to different solid phase separations at the tee where the exhaust is divided, and because of increased condensation of sulphur species on the particulate matter as a result of the decreased exhaust temperature at the lower flow rates.

The collection efficiencies of the ESPs were as high as 99% at exhaust flow rates of 2.5 and 5 kg/hr. The ESP collection efficiency decreased with increased exhaust flow rate at a given ESP applied voltage. The flow separator was installed in order to reduce the exhaust gas flow past the ESPs, while attempting to maintain a highly soot-loaded flow. At exhaust flow rates of 2.5, 3.75 and 5 kg/hr, the collection efficiency of the FS-ESP with the straight inlet did not exceed 30%. Modifications were made to the FS-ESP in order to improve particle separation. Two small inserts with the form of a venturi were installed upstream and downstream of the perforated sections of the separator, and the diameter of the branches leading to the ESPs were increased. The collection efficiency of the modified flow separator was on the order of 60% for the 2.5 kg/hr exhaust flow, at an applied voltage of 22 kV. For the higher exhaust flow rates, the collection efficiencies were only slightly improved over the original configuration.

The pressure drop across the flow separator was less than 25 Pa under all test conditions. Tests passing air through the FS-ESP showed pressure drops on the order of 4 Pa, with a dimensionless pressure drop coefficient of about 5. This is significantly lower than the tens of kPa typically associated with diesel particulate filters, but it is difficult to compare the two devices properly because of the low flow rates tested

in this study.

This same flow separator concept was used successfully in natural gas flows, but does not seem to be as effective in the diesel exhaust flow. In this configuration, this flow separator does not compete with the commonly used diesel particulate filter in terms of particulate collection efficiency, despite improved pressure drop characteristics.

5.2 Recommendations

Continued development of the flow separator characterized in this study for treatment of diesel particulate matter in automotive applications is recommended. The gap in performance between this device and diesel particulate filters is great, however, it may be reduced through design improvements. Further study on the effect of the geometry and spacing of the flow restriction used in the modified FS-ESP is warranted, as well as the number, size and placement of the perforations in the separator.

It is also suggested that the concept be approached from another perspective. Rather than depending on a single flow separator with two or more ESPs for particle collection, this study suggests that because of the low gas flow rates through the ESPs, the exhaust gases should be divided into several separator components that share a single ESP.

Sampling for diesel particulate matter could be improved in further studies. It is recommended that heated sampling lines be used rather than simply insulated tubes. Further, it is recommended that a detailed study on the characteristics of the particulate matter emitted by the engine be performed. Future work on this test cell would benefit from more detailed information such as the size distribution and chemical composition of the diesel particulate matter.

BIBLIOGRAPHY

40 CFR 86 (2004). United states code of federal regulations 40, part 86.

Abd-Ala, G. H. (2002). Using exhaust gas recirculation in internal combustion engines: a review. *Energy Converseion and Management*, 43:1027–1042.

Adachi, M. (2000). Emission measurement techniques for advanced powertrains. *Measurment Science and Technology*, 11:R113–R129.

Adler, U., Bauer, H., Cypra, A., Dinkler, F., Kunne, P., and Roder, J. (1993). *Automotive Handbook*. Robert Bosch GmbH, Stuttgart, 3rd edition.

Alkidas, A. C. and Cole, R. M. (1983). Gaseous and particulate emissions from a single-cylinder divided-chamber diesel engine. In *Worldwide Review of Diesel Combustion Emissions and Analysis P-130*, pages 1–13. Society of Automotive Engineers, Inc., Warrendale, PA.

Ashley, S. (1993). A flexible sampler for diesel exhaust. *Mechanical Engineering*, pages 70–71.

Badzioch, S. (1960). Correction for anisokinetic sampling of gas-borne dust particles. *Journal of the Institute of Fuel*, March:106–110.

Bauer, H., Dietsche, K.-H., Cripin, J., and Dinkler, F., editors (2000). *Automotive Handbook*. Robert Bosch GmbH, Stuttgart, 5th edition.

Bermúdez, V., Payri, R., Salvador, F. J., and Plazas, A. H. (2005). Study of the influence of nozzle seat type on injection rate and spray behaviour. *Proceedings of the Institude of Mechanical Engineers Part D: Journal of Automobile Engineering*, 219:677–689.

Beuthe, T. G. and Chang, J. S. (1995). Gas discharge phenomena. In Chang, J. S., Kelly, A. J., and Crowley, J. M., editors, *Handbook of Electrostatic Processes*, pages 147–193. Marcel Dekker, New York.

Chan, S. H., Sun, J. H., and Low, S. C. (1998). A compact particulate dilution tunnel for the characterization of diesel exhaust. *Proceedings of the Institution of Mechanical Engineers - Part D*, 212:299–310.

Chang, J. S. and Touchard, G. (1999). Flow electrification induced electrohydrodynamic secondary flow. *1999 Conference on Electrical Insulation and Dielectric Phenomena*, pages 798–801.

Charles, F. L. R. (2005). The effect of exhaust mass flow rate and coolant temperature on the performance of exhaust gac recirculation cooling devices. Master's thesis, McMaster University, Hamilton, Ontario.

Chen, F. and Lai, A. C. K. (2004). An Eulerian model for particle deposition under electrostatic and turbulent conditions. *Journal of Aerosol Science*, 35:47–62.

Corro, G. (2002). Sulfur impact on diesel emission control - a review. *Reaction Kinetics and Catalysis Letters*, 75(1):89–106.

Dockery, D. W., Pope, C., Xu, X. P., Spengler, J. D., Ware, J. H., Fay, M. E., Ferris, B. G., and Speizer, F. E. (1993). An association between air pollution and mortality in six us cities. *The New England Journal of Medicine*, 329(24):1753–1759.

Environment Canada (2001a). Precoursor contributions to ambient fine particulate matter in canada. Government publication, Environment Canada; Meteorological Service of Canada.

Environment Canada (2001b). Trucks and air pollution. Technical Report EPS

2/TS/14, Air Pollution Prevention Directorate, Environmental Protection Service, Environment Canada. Gov Pub CA1..EP.108-2001T61.

Environment Canada (2002). National overview - on-site releases of npri pollutants 2002. Government publication, Environment Canada, National Pollutant Release Inventory. Available Online: http://www.ec.gc.ca/pdp/npri/2004N_Overview/2002on_ site_e.cfm.

Fox, R. W. and McDonald, A. T. (1998). *Introduction to Fluid Mechanics*. J. Wiley.

Friedlander, S. K. (1977). *Smoke, dust and haze*. John Wiley and Sons, New York.

Frisch, L. E., Johnson, J. H., and Leddy, D. G. (1979). Effect of fuels and dilution ratio on diesel particulate emissions. In *The Measurement and Control of Diesel Particulate Emissions*, chapter PT-79, pages 245 – 273. Society of Automotive Engineers, Inc., Warrendale, PA.

Gauderman, W. J., Avol, E., Gilliland, F., Vora, H., Thomas, D., Berhane, K., McConnell, R., Kuenzli, N., Lurmann, F., Rappaport, E., Margolis, H., Bates, D., and Peters, J. (2004). The effect of air pollution on lung development from 10 to 18 years of age. *The New England Journal of Medicine*, 351(11):1057–1067.

Gotoh, K. and Masuda, H. (2001). Development of annular-type virtual impactor. *Powder Technology*, 118(1–2):68–78.

Hall, H. J. (1990). History of pulse energization in electrostatic precipitation. *Journal of Electrostatics*, 25:1–22.

HAQI (1997). Human health risk assessment for priority air pollutants. Government Publication CA3ON HW V09, Hamilton-Wentworth Air Quality Initiative (HAQI).

Harvel, G. D., Chang, J. S., Guan, L., Nock, M., Brocilo, D., and Urashima, K. (2004). Dust flow separator type electrostatic precipitator for the dust emission control from gas combustion flue gases. In *4ème Conference SFE*, pages 39–44. Sociéte Française d'Electrostatique, Poitiers, France.

Heywood, J. B. (1988). *Internal combustion fundamentals*. McGraw-Hill, New York.

Hinds, W. C. (1982). *Aerosol Technology*. J. Wiley, New York.

IEEE-DEIS-EHD Technical Committee (2003). Recommended international standard for dimensionless parameters used in electrohydrodynamics. *IEEE Transactions on Dielectrics and Electrical Insulation*, 10(1):3 – 6. Dimensionless parameter;Energy conservation equation;.

Ismail, B. A. (2004). *The Heat Transfer and the soot deposition characteristics in diesel engine exhaust gas recirculation system cooling devices*. PhD thesis, McMaster University, Hamilton, Ontario.

Jones, C. C., Chughtai, A. R., Murugaverl, B., and Smith, D. M. (2004). Effects of air/fuel combustion ratio on the polycyclic aromatic hydrocarbon content of carbonaceous soots from selected fuels. *Carbon*, 42:2471–2484.

Kidoguchi, Y., Sanda, M., and Miwa, K. (2003). Experimental and theoretical optimization of combustion chamber and fuel distribution for the low emission direct-injection diesel engine. *Journal of engineering for gas turbines and power*, 125:351–357.

Kittelson, D. B. (1998). Engines and nanoparticles: A review. *Journal of Aerosol Science*, 29(5/6):575–588.

Kittelson, D. B., Arnold, M., and Watts, Jr, W. F. (1999). Review of diesel particulate matter sampling methods final report. Technical report, University of Minnesota,

Department of Mechanical Engineering, Center for Diesel Research, Minneapolis, MN.

Klemm, R. J., Mason, Jr., R. M., Heilig, C. M., Neas, L. M., and Dockery, D. W. (2000). Is daily mortality associated specifically with fine particles? data reconstruction and replication of analyses. *Journal of the Air & Waste Management Association*, 50:1215–1222.

Kline, S. J. and McClintock, F. A. (1953). Describing uncertainties in single-sample experiments. *Mechanical Engineering*.

Ladommatos, N., Abdelhalim, S. M., and Zhao, H. (1998). Effects of exhaust gac recirculation temperature on diesel engine combustion and emissions. *Proceedings of the Institution of Mechanical Engineers - Part D*, 212:479–500.

Lanzerstorfer, C. (2000). Solid/liquid-gas separation with wet scrubbers and wet electrostatic precipitators: A review. *Filtration and Separation*, 37(5):30–34.

Lin, C. Y. (2002). Reduction of particulate matter and gaseous emission from marine diesel engines using a catalyzed particulate filter. *Ocean Engineering*, 29:1327–1341.

Lin, J. S. and Tsai, C. J. (2003). Thermophoretic deposition efficiency in a cylindrical tube taking into account developing flow at the entrance region. *Journal of Aerosol Science*, 34:569–583.

Liu, R. and Zhang, C. (2004). A numerical study of no_x reduction for a di diesel engine with complex geometry. *Journal of Energy Resources Technology*, 126:13–20.

Masuda, S. and Hosokawa, S. (1995). Electrostatic precipitation. In Chang, J. S., Kelly, A. J., and Crowley, J. M., editors, *Handbook of Electrostatic Processes*, chapter Chapter 21. Marcel Dekker.

Masuda, S. and Moon, J. D. (1983). Electrostatic precipitation of carbon soot from diesel engine exhaust. *IEEE Transactions on Industry Applications*, IA-19(6):1104–1111.

Messerer, A., Niessner, R., and Pöschl, U. (2003). Thermophoretic deposition of soot aerosol particles under experimental conditions relevant for modern diesel engine exhaust gas systems. *Journal of Aerosol Science*, 34:1009–1021.

Mody, V. and Jakhete, R. (1989). *Dust Control Handbook*. William Andrew Publishing/Noyes, Westwood, New Jersey.

Reichel, S., Pischinger, F. F., and Lepperhoff, G. (1983). Influence on particles in diluted diesel engine exhaust gas. In *Worldwide review of diesel combustion emissions and analysis*, pages 187–200. Society of Automotive Engineers, Inc., Warrendale, PA.

Reynolds, A. J. (1974). *Turbulent Flows in Engineering*. J. Wiley.

Riehle, C. and Löffler, F. (1991). The significance of the current-voltage characteristics in geometric-similar parallel plate precipitators. In *Proceedings of the fourth international conference on electrostatic precipitation, 1990*, pages 123–135. International Academic Publishers, Beijing China.

Rosner, D. E. and Khalil, Y. F. (2000). Particle morphology- and Knudsen transition-effects on thermophoretically dominated total mass deposition rates from "coagulation-aged" aerosol population. *Journal of Aerosol Science*, 31(3):273–292.

Samet, J. M., Dominici, F., Curriero, F. C., Coursac, I., and Zeger, S. L. (2000). Fine particulate air pollution and mortality in 20 u.s. cities, 1987-1994. *The New England Journal of Medicine*, 343(24):1742–1749.

Snelling, D. R., Smallwood, G., Sawchuk, R. A., Neill, W. S., Gareau, D., Chippior, W. L., Liu, F., Gülder, O. L., and Bachalo, W. D. (1999). Particulate matter measurements in a diesel engine exhaust by laser-induced incandescence and the standard gravimetric procedure. *SAE Technical Paper Series*, 1999-01-3653.

Su, W. H., Lin, T. J., Zhao, H., and Pei, Y. Q. (2005). Research and development of an advanced combustion system for the direct injection diesel engine. *Proceedings of the Institude of Mechanical Engineers Part D: Journal of Automobile Engineering*, 219:241–252.

Sutherland, K. (2005). Centrifuge focus: solids removal - the options. *Filtration And Separation*, 42(6):16–20.

Vouitsis, E., Ntziachristos, L., and Samaras, Z. (2003). Particulate matter mass measurements for low emitting diesel powered vehicles: what's next? *Progress in Energy and Combustion Science*, 29:635–672.

Vouitsis, E., Ntziachristos, L., and Samaras, Z. (2005). Modelling of diesel exhaust aerosol during laboratory sampling. *Atmospheric Environment*, 39:1335–1345.

Walker, A. P. (2004). Controlling particulate emissions from diesel vehicles. *Topics in Catalysis*, 28(1-4):165–170.

Wang, H. (2005). Development and characterization of a virtual impactor type dust flow concentrator. Master's thesis, Department of Mechanical Engineering, McMaster University, Hamilton, Ontario.

Watson, H. H. (1954). Errors due to anisokinetic sampling of aerosols. *Industrial Hygiene Quarterly*, March:21–25.

Wentzel, M., Gorzawski, H., Naumann, K.-H., Saathoff, H., and Weinbruch, S. (2003).

Transmission electron microscopal and aerosol dynamical characterization of soot aerosols. *Journal of Aerosol Science*, 34:1347–1370.

Wong, C. P., Chan, T. L., and Leung, C. W. (2003). Characterization of diesel exhaust particle number and size distributions using mini-dilution tunnel and ejector-diluter measurement techniques. *Atmospheric Environment*, 37:4435–4446.

Yanowitz, J., McCormick, R. L., and Graboski, M. S. (2000). In-use emissions from heavy-duty diesel vehicles. *Environmental Science and Technology*, 34(5):729–740.

Zheng, M., Reader, G. T., and Hawley, J. G. (2004). Diesel engine exhaust gas recirculation - a review on advanced and novel concepts. *Energy conversion and management*, 45:883–900.

Zhuang, Y., Kim, Y. J., Lee, T. G., and Biswas, P. (2000). Experimental and theoretical studies of ultra-fine particle behavior in electrostatic precipitators. *Journal of Electrostatics*, 48:245–260.

Zukeran, A., Ikeda, Y., Ehara, Y., Ito, T., Takahashi, T., Kawakami, H., and Takamatsu, T. (2000). Agglomeration of particles by ac corona discharge. *Electrical Engineering in Japan*, 130(1):367–372.

Zukeran, A., Ikeda, Y., Ehara, Y., Matsuyama, M., Ito, T., Takahashi, T., Kawakami, H., and Takamatsu, T. (1999). Two-stage-type electrostatic precipitator re-entrainment phenomena under diesel flue gases. *IEEE Transactions on Industry Applications*, 35(2):346–351.

APPENDIX A

FS-ESP Design Details

The form and function of the flow separator type ESP used in the present work has been described in the text. Included in this Appendix are Figures A.1 and A.2, which provide detailed dimensions of the FS-ESP and the location of the venturi shaped insert, respectively. The FS-ESP is symmetric about its central axes. As illustrated in Figure A.2, the upstream insert is located directly upstream of the perforations in the separator.
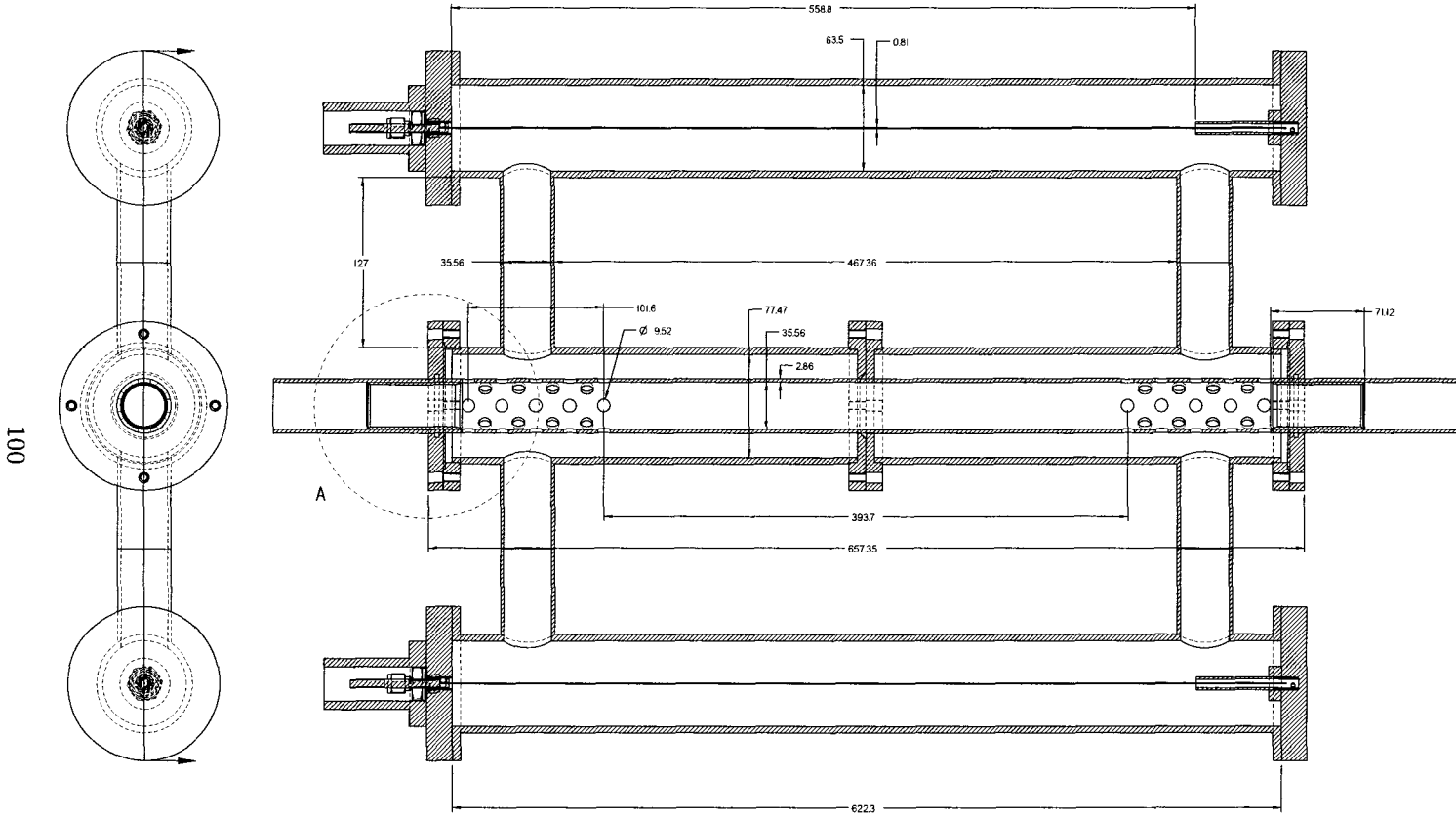
Figure A.1: Detailed dimensions and setup of FS-ESP. All dimensions in mm. See Figure A.2 for Detail A.
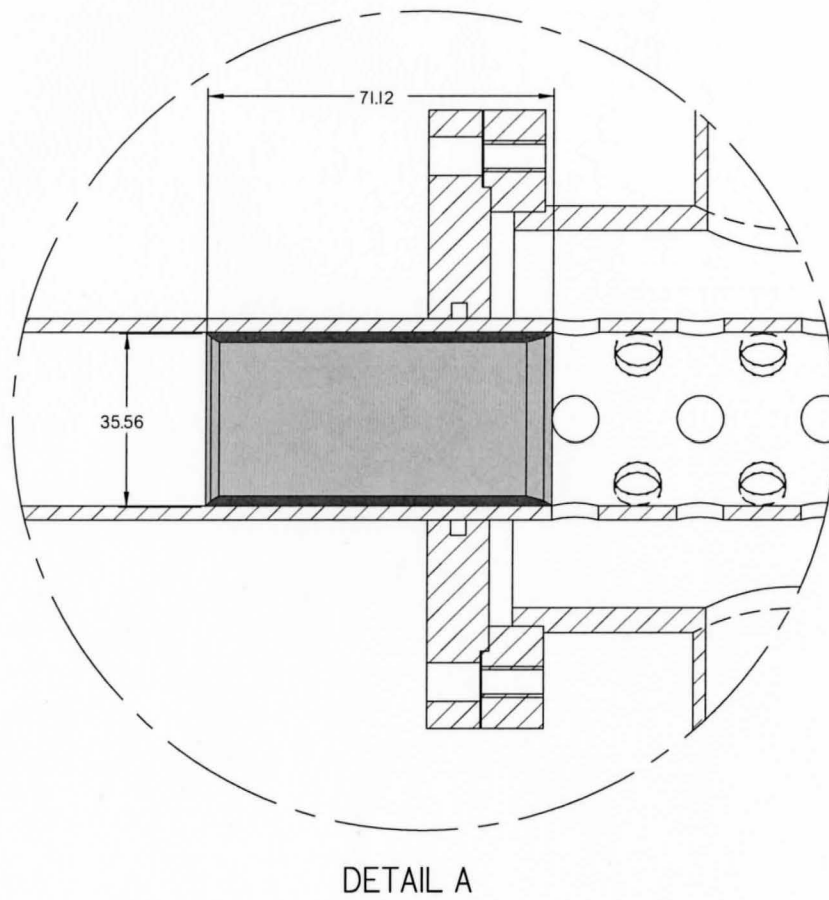
DETAIL A

Figure A.2: Detailed view of the upstream venturi insert showing dimensions and position relative to the flow separator. See Figure A.1 for location of detail.

APPENDIX B

Development and Characterization

of a Micro-Dilution Tunnel for

DPM Measurement

The micro-dilution tunnel concept was introduced in Section 3.1. This chapter details the design and characterization of the micro-dilution tunnel. The micro-dilution tunnel is essentially a confined coaxial jet, with exhaust gases flowing through the central jet and dilution air flowing through the annular jet, as shown in Figure B.1.

The two jets must be concentrically aligned, to ensure unbiased (even) mixing. In the present work, this is evaluated by examining the mean velocity profile obtained from each individual jet, at several downstream cross-sections. Further, the mean velocity, turbulence intensity, and temperature profiles were used to characterize the amount of mixing at different downstream distances.
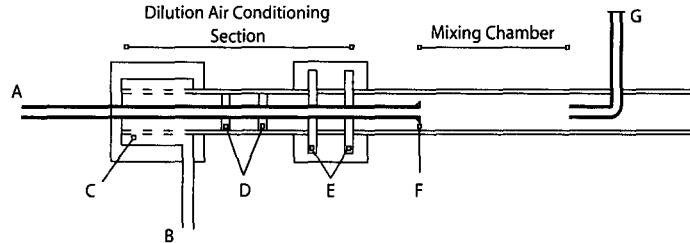
Figure B.1: Micro-dilution tunnel design details

B.1   Micro-Dilution Tunnel Design

A schematic of the micro-dilution tunnel is shown in Figure B.1. The diesel engine exhaust enters the micro-dilution tunnel through the primary sampling tube at A. Dilution gas enters a conditioning section of the dilution tunnel at B. Conditioning of the dilution air consists of a series of perforated plates (radial at C and planar at D) and mesh screens (E). Prior to entering the mixing chamber, the dilution gas passes over a ferrule at F. This creates a low pressure region on the centerline to facilitate the flow of the exhaust gases from the sampling tube, as well as creates a stronger shear layer to aid in mixing. The diluted exhaust is sampled at the secondary sampling tube, G.

B.2   Experimental Methodology

The alignment of the individual jets within the micro-dilution tunnel was evaluated first, by measuring profiles of mean velocity, turbulence intensity, and temperature at several axial locations within the mixing chamber of the micro-dilution tunnel. Tests were performed for several flow rate combinations as summarized in Table B.1, that correspond to dilution air and exhaust flow rates required for sampling of exhaust mass flow rates at 40 kg/hr (high) and 5 kg/hr (low) in the 35 mm (1 1/4" nominal) pipes used on the diesel rig. The dilution ratio for both combinations

	Low Flow	High Flow
Central	90.6 LPM	153 LPM
Annular	10.1 LPM	17 LPM

Table B.1: Low and High Flow rates used in micro-dilution tunnel mixing experiments

was 10.

The flow field was measured by installing a hot wire anemometer into the micro-dilution tunnel such that the end of the probe was located at axial distances of $x/d =$ 0.5, 1.1, 2.5, 5.0, 7.3, 8.8 and 12.1. A schematic of the test rig is shown in Figure B.2. The hot wire used was a DISA model number 55P11 with 4 mm diameter, 30 mm long body, and 1.5 mm long, 0.5 μm diameter wire. It was connected to a DISA Type 56C01 CTA bridge using a 5 m BNC cable. The bridge was connected to the Analog to Digital board on the data acquisition computer. The hot wire was calibrated using an in-house calibration jet. A 15-point curve was obtained, relating flow velocity to voltage, resulting in a fourth order polynomial.

The temperature profiles were measured by replacing the hot wire anemometer with a K-type thermocouple. In these tests, the central jet was heated using an electrical heater, and the annular jet was kept at room temperature. Both instruments were installed on a traverse mechanism with a dial gauge indicating the relative position across the tube to within 0.01 mm. The coordinate system describing the horizontal and vertical traverse position is shown in Figure B.3.

A Labview program was created to record turbulence measurements from the hot wire using the Microstar iDSC. The required sampling frequency was estimated by recording 20 seconds of data from the near field of the central jet at 9600 Hz. This was performed at approximately the center of the 4.6 mm diameter jet, at a Reynolds
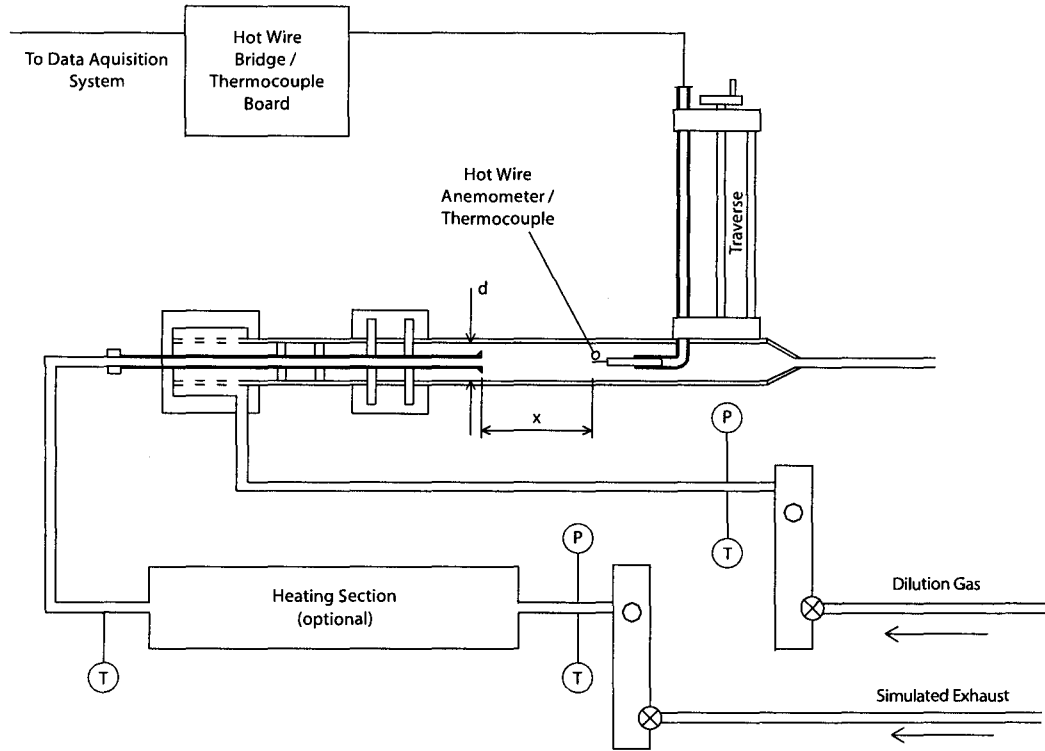
Figure B.2: Micro-dilution tunnel test rig for mean velocity, turbulence intensity, and temperature profiling.

number of approximately 5200. The dissipation, ε, was obtained using

$$\varepsilon \approx 15\nu \overline{\left(\frac{\partial u}{\partial x}\right)^2},$$
(B.1)

with approximations for the fluctuating velocity components using Taylor's hypothesis (eg. Reynolds (1974)),

$$\frac{\partial u}{\partial t} = \frac{u'(t + \Delta t) - u'(t)}{\Delta t}$$
(B.2)

and

$$\frac{\partial u}{\partial x} = \frac{1}{U_m}\frac{\partial u}{\partial t}.$$
(B.3)
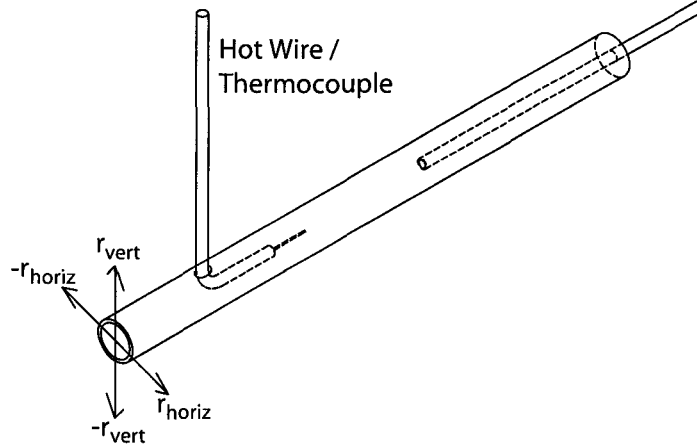
Figure B.3: The coordinate system used to describe the traverse position.

This resulted in $\varepsilon = 16.690$ m^2/s^3, which was used in the expression for the Komologrov timescale:

$$\tau \approx \left(\frac{\nu}{\varepsilon}\right)^{1/2}. \tag{B.4}$$

The Nyquist frequency, assumed to be 2.5 times the frequency of the Komologrov timescale, was determined to be 2637 Hz.

In the experiments, data was sampled at 3200 Hz for 4 seconds, or 12,800 points of continuous data. This was repeated five times in sequence, resulting in 20 seconds of data that was obtained over a period of approximately 35 seconds.

The temperature was measured at each point for a period of 20 seconds. The result was then averaged. The standard thermocouple calibration curve was used, with a stated accuracy of $\pm 0.9°$C.

B.3   Jet Alignment Results

The horizontal and vertical mean velocity profiles for the central jet and the annular jet were measured separately. The profiles were then non-dimensionalized by

the maximum velocity, and are plotted in Figure B.4 for the high-flow case ($V_{central} =$ 17 SLPM and $V_{annular} = 153$ SLPM). The velocity of the annular jet was between 3 and 10 m/s at all axial distances. It can be seen that there is a slight bias on the order of 5 – 10% towards the bottom and right sides for the annular jet. This bias could be attributed to slight misalignment of the jets, or the change in blockage area of the probe holder as it makes the traverse. In the context of the present work, this bias is negligible. The maximum velocity measured in the central jet case was approximately 21 m/s at $x/d = 0.5$. This decayed quickly to about 1 m/s at $x/d = 2.5$ because of the very low flow rate. The central jet was well aligned. Tests beyond $x/d = 2.5$ (central) or $x/d = 7.3$ (annular) and at the lower flow rates were not performed, as the velocities in the dilution chamber would be too low for the hot wire to provide meaningful data.
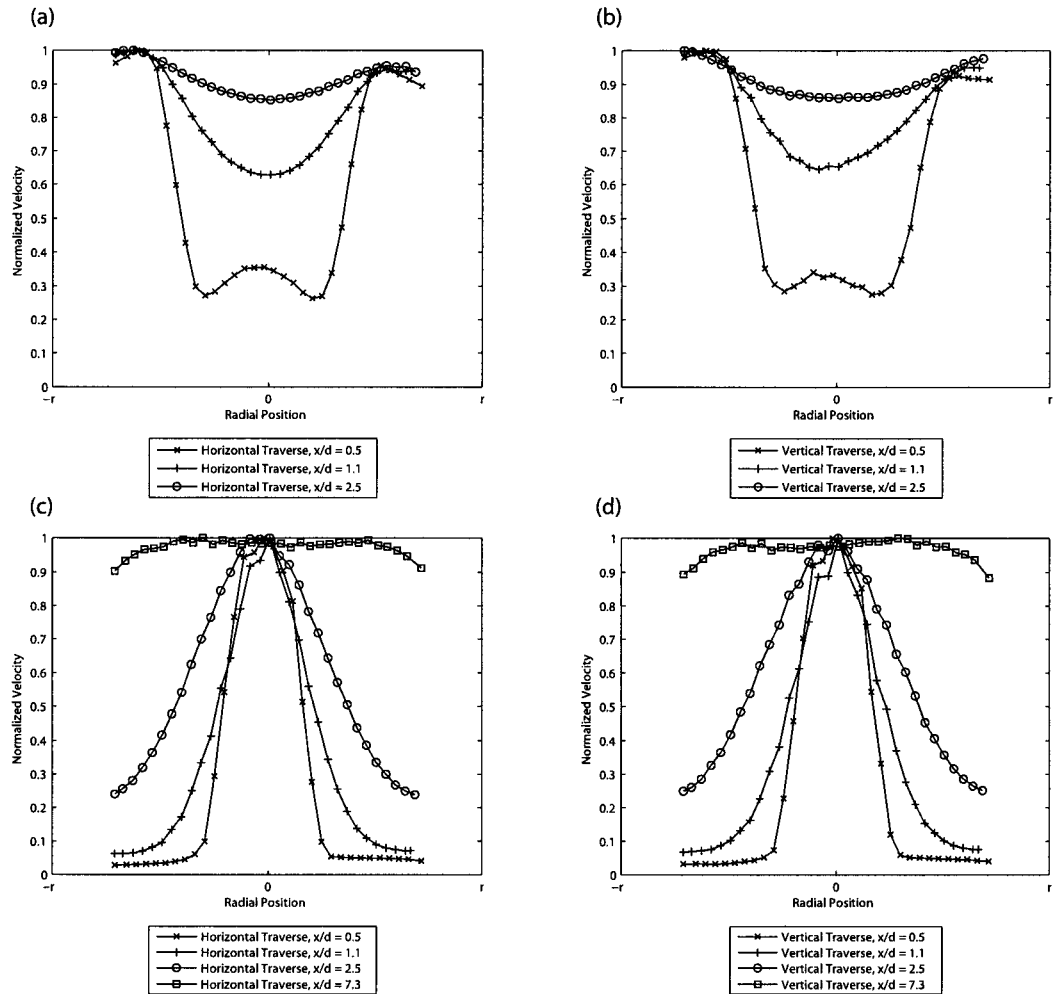
Figure B.4: Mean velocity profiles of individual jets normalized to maximum velocity: (a) Annular jet, horizontal traverse; (b) Annular jet, vertical traverse; (c) Central jet, horizontal traverse, (d) Central jet, vertical traverse

B.4   Jet Mixing Results

Next, the flow development within the micro-dilution tunnel mixing chamber was characterized by obtaining mean velocity, turbulence intensity and temperature profiles at several downstream locations. The coaxial jets were run at the flow rates outlined in Table B.1. The mean velocity and turbulence intensity measurements were obtained using room temperature air, while the temperature profiles were obtained by heating the central jet to about 75 °C (low flow rate) or 115 °C (high flow rate). Summaries of the results are presented in Figures B.5 – B.8.

For both high and low flow rates, the mean velocity profiles become approximately independent of x/D at $x/D \simeq 7.3$. The turbulence intensity profiles confirm that the shear layers have essentially disappeared at this axial distance. The temperature profiles become independent axial distance at 5 downstream diameters. This agrees with Chan et al. (1998), who state that a mixing chamber length of 10 diameters is required for the exhaust gases and particulate matter to be fully mixed in dilution tunnels. A mixing chamber length of $x/D = 10$ was used for the remainder of this work.
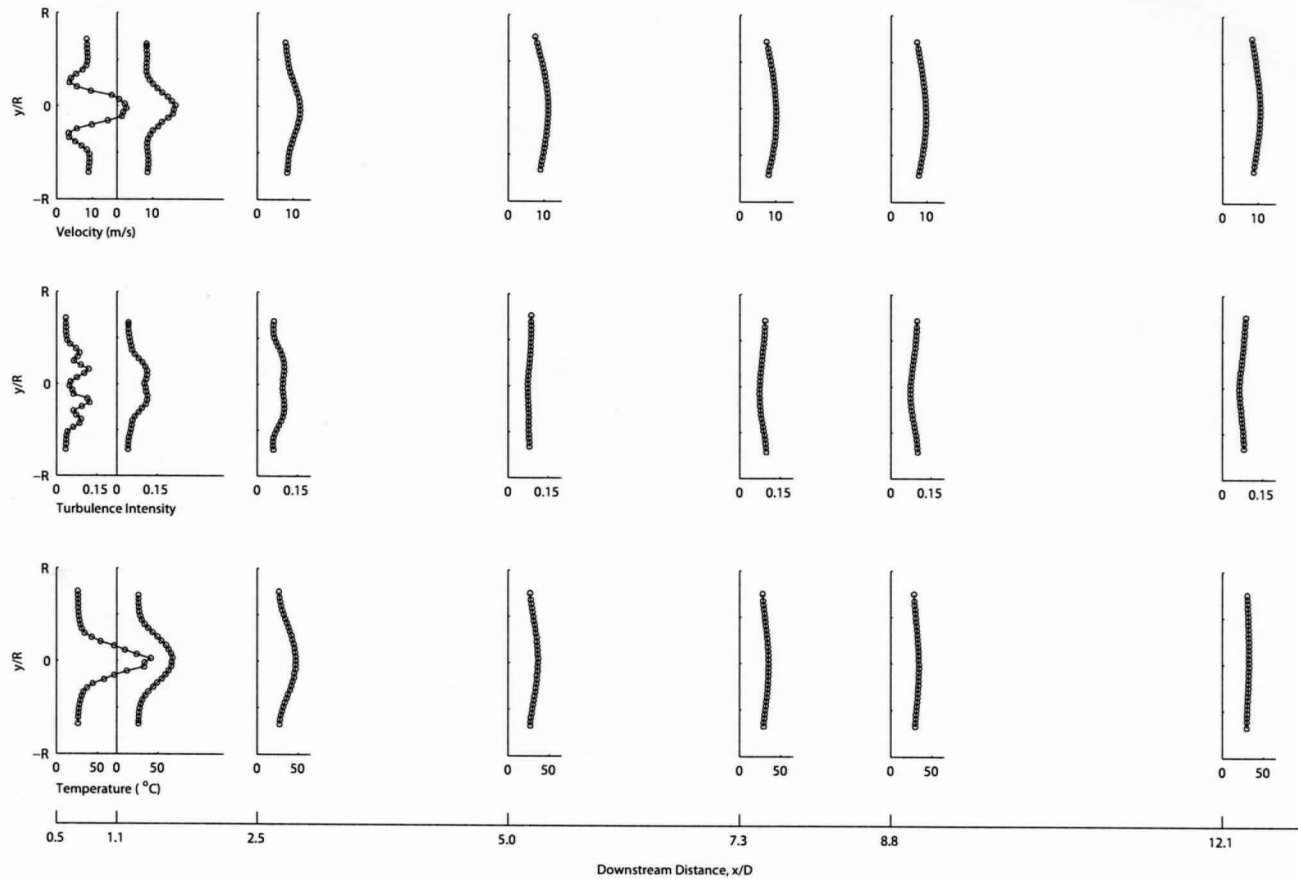
Figure B.5: Evolution of mean velocity, turbulence intensity and temperature profiles in mixing chamber at high flow rates in the horizontal direction.
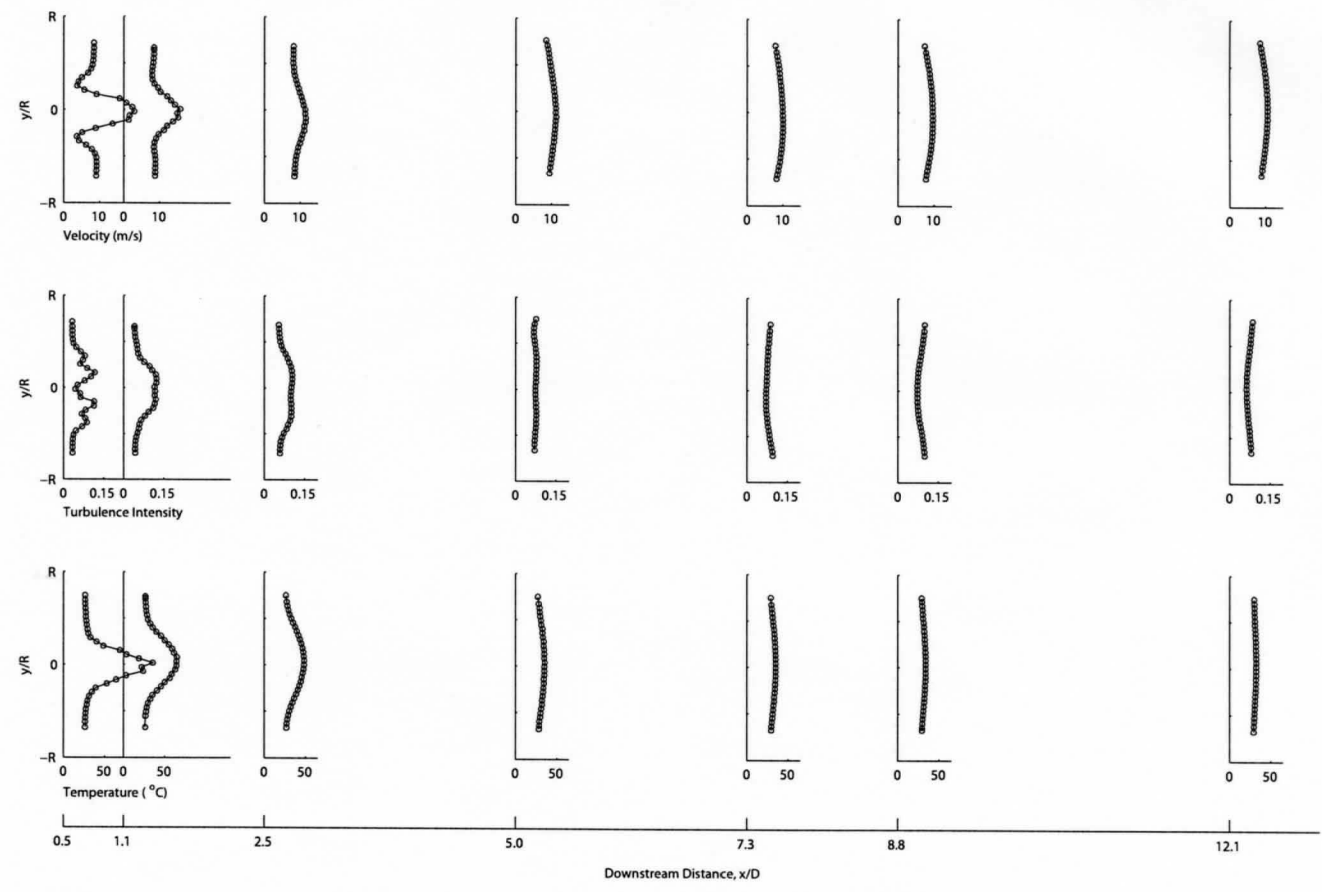
Figure B.6: Evolution of mean velocity, turbulence intensity and temperature profiles in mixing chamber at high flow rates in the vertical direction.
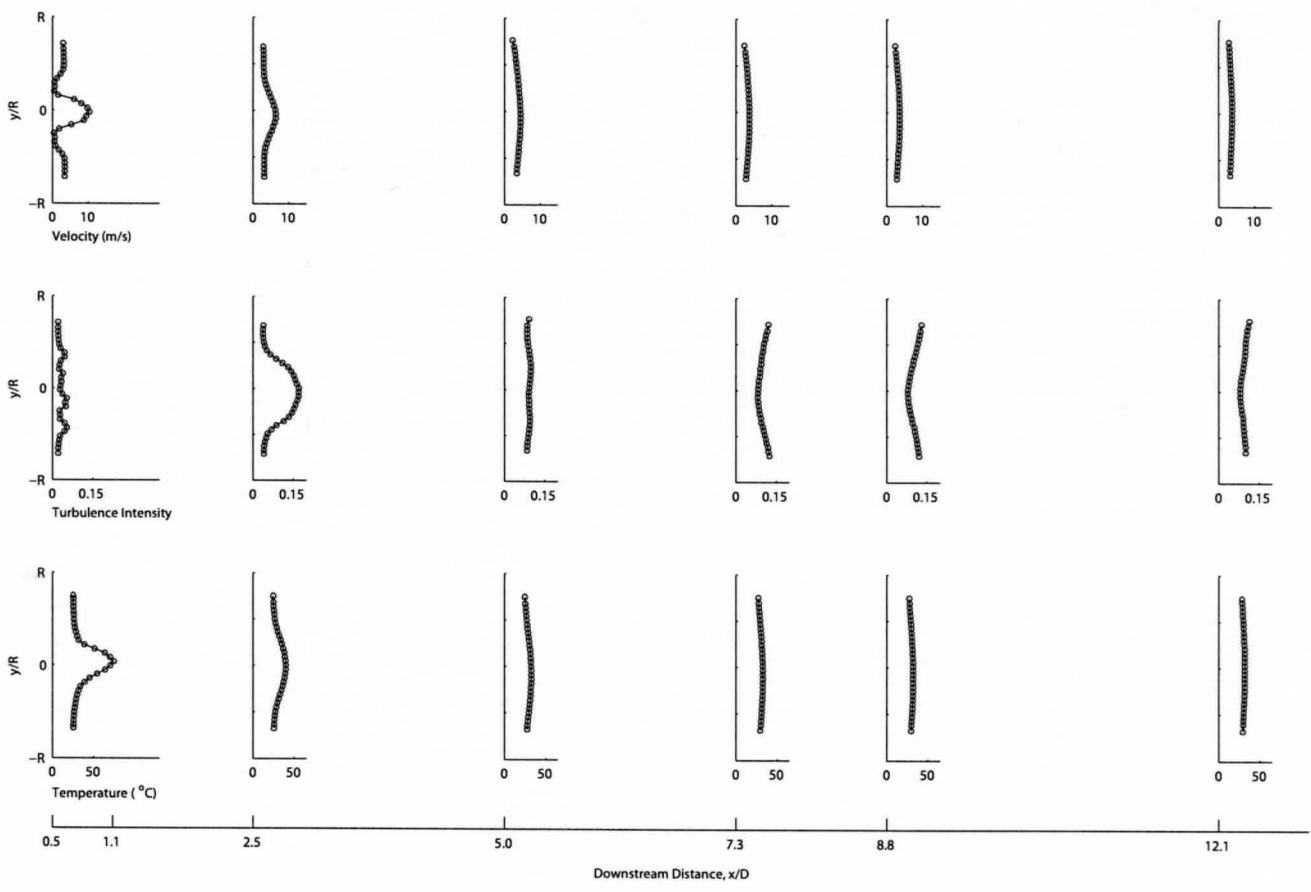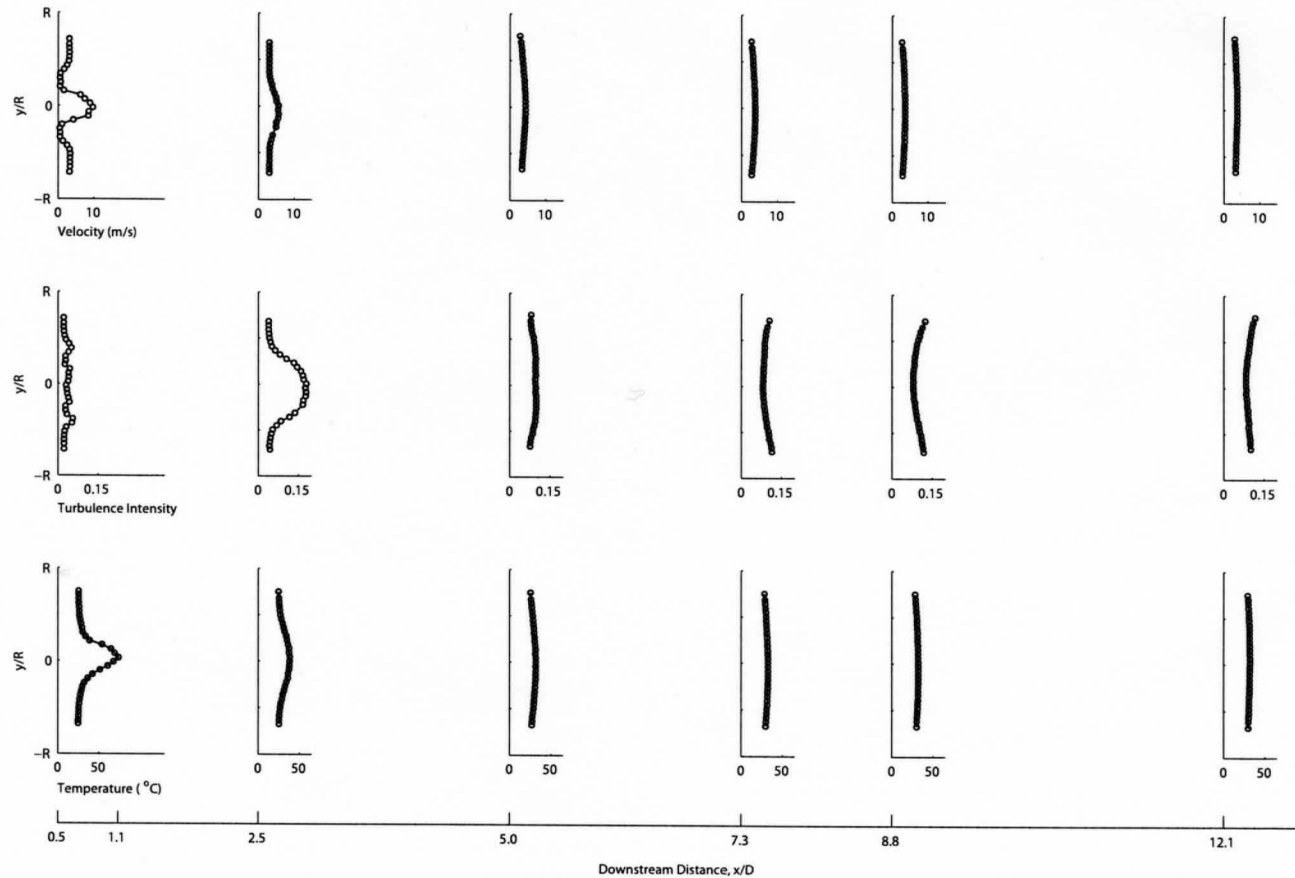
Figure B.7: Evolution of mean velocity, turbulence intensity and temperature profiles in mixing chamber at low flow rates in the horizontal direction.

Figure B.8: Evolution of mean velocity, turbulence intensity and temperature profiles in mixing chamber at low flow rates in the vertical direction.

APPENDIX C

Size and Number Density

Characteristics of Diesel

Particulate Matter

The diesel particle size distribution was measured in the facility used in the present work by Ismail (2004). Measurements are reproduced here and shown in Figure C.1. The measurements were taken at a location located approximately the same distance downstream of the engine as SP1 in the present work, but on another test leg. The exhaust flow rate was 6 kg/hr and engine load was 2.4 kW. The measurements were obtained using a condensation-nucleation particle counter with manually changed particle size cut-off screens. Particles with diameters between 0.132 and 0.162 μm could not be measured with this system. It was found that the total particulate matter number density was on the order of 10^{10} particles/m^3 with a bimodal (or
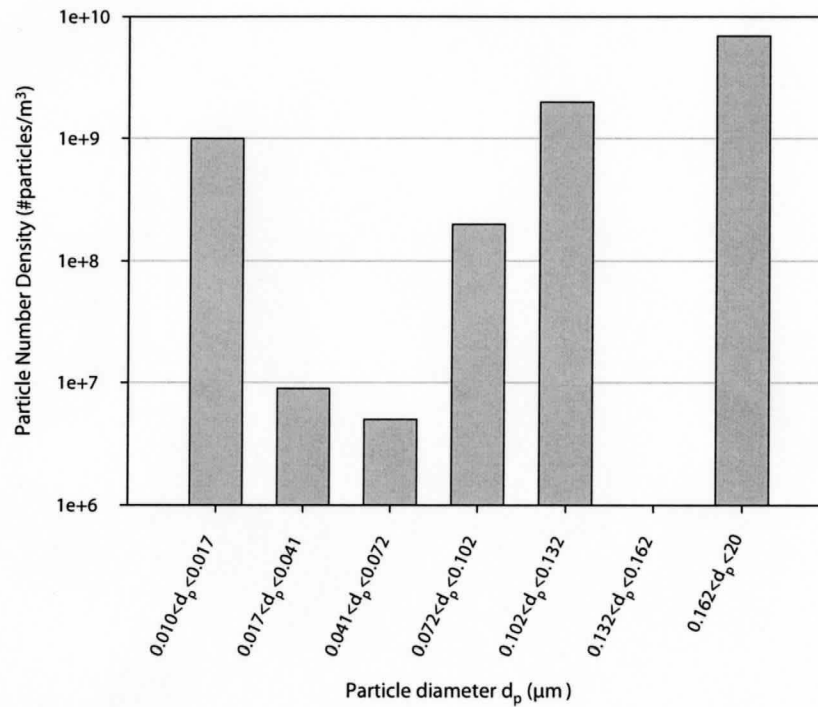
Figure C.1: Measurements of diesel particulate matter size and number density performed by Ismail (2004).

possibly trimodal) distribution with peaks of $0.010 < d_p < 0.017$ μm, $0.102 < d_p < 0.132$ μm and $0.162 < d_p < 20$ μm.

Similar results were obtained by analysis of images obtained by scanning electron microscope (SEM) during the course of the present work. A partial sample of particulate-laden exhaust gas was deposited on a fibreglass filter, dried, and prepared for SEM analysis. Only a small number of SEM images were obtained, with examples of typical images shown in Figure C.2. The size distribution obtained from analysis of these images is shown in Figure C.3, which suggests an accumulation mode with peak particle diameter on the order of 0.1 μm. The coarse mode particles were not included in this size analysis.
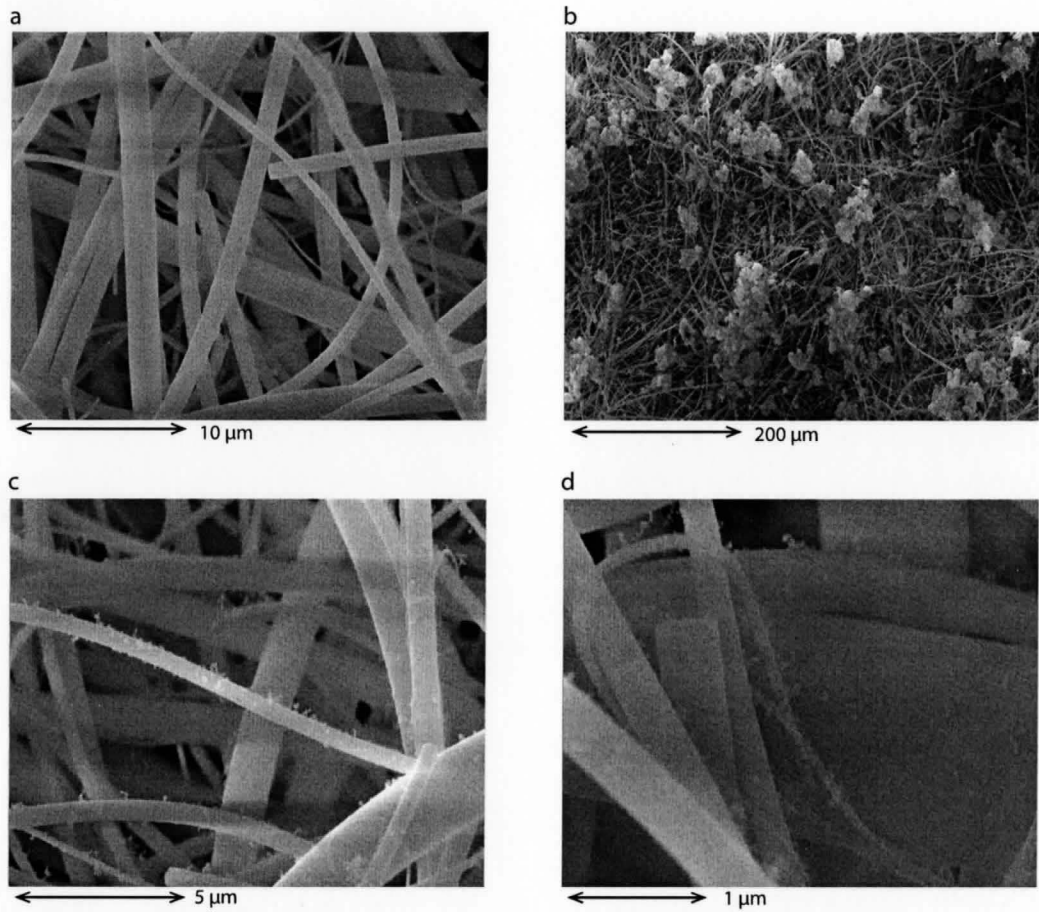
Figure C.2: Typical images from scanning electron microscope: a) Clean filter, b) Coarse mode particles, c) and d) Highly magnified accumulation mode particles.
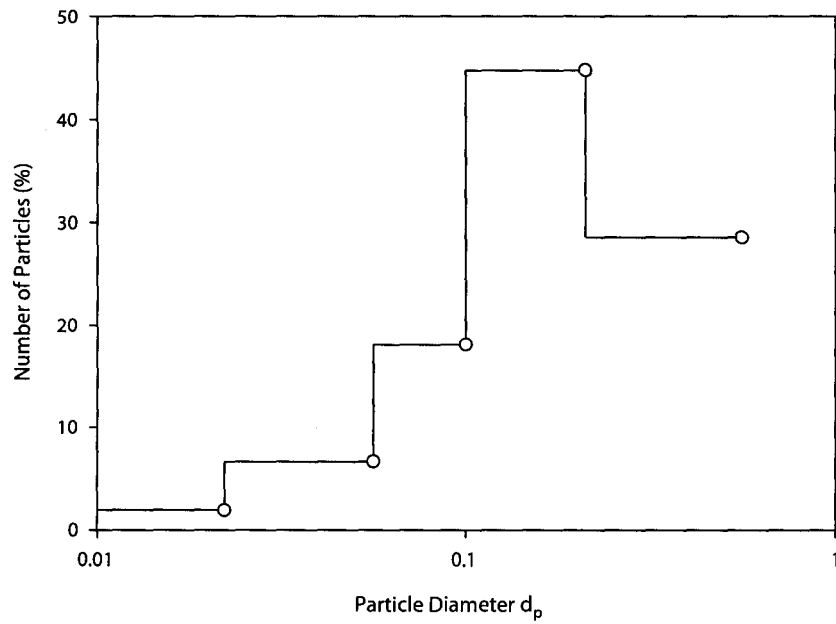
Figure C.3: Measurements of diesel particulate matter size distribution by scanning electron microscope.

APPENDIX D

Particulate Matter Deposition in ESPs

In an effort to understand the dynamics within the ESPs in the ESP-only configuration, maps of the deposition of PM on the collection electrode were made at the end of each experiment. These qualitative maps were created by measurement of the axial and radial size and location of visibly distinct regions of particulate matter deposition within the ESPs.

Figures D.1, D.2 and D.3 show these maps for exhaust flow rates of 2.5 kg/hr, 5 kg/hr and 10 kg/hr, respectively. In the 5 and 10 kg/hr cases, there was a scoured region opposite the inlet tube where the exhaust gases impinged on the wall of the ESP. A thick layer of particulate matter is deposited on the wall adjacent to the scoured area, and it is significantly larger in the 10 kg/hr case. This thick deposition is likely due to the deposit of the soot from the incoming flow on the wall due
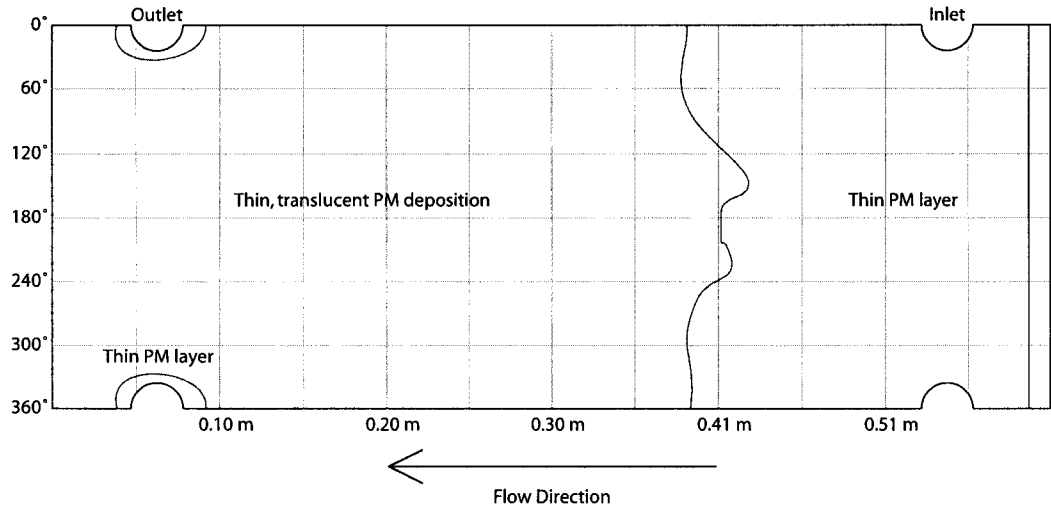
Figure D.1: Relative PM Deposition Inside ESP for 2.5 kg/hr exhaust flow rate.

to turbulent diffusion and thermophoresis, in addition to electrophoresis. The areas of thin, translucent particulate matter deposition on the collection electrode suggest domination of electrophoretic deposition in these regions. This is because it is very homogeneous in both the axial and radial directions, consistent with the radial electrophoretic force applied to the particulate matter. The soot layer was not as thick at the inlet section for the 2.5 kg/hr exhaust flow case and this contributed to the prolonged stable operation of the device. The soot layer at the inlet of the ESPs was thinner in this case, likely because the exhaust jet entering the ESP was not as strong, minimizing the impinging jet effect on the opposite wall as evidenced by the lack of scoured area opposite the inlets. This allowed the particulate laden flow to change direction and flow axially along the ESP. The electrical stability of the ESP is improved because of this homogeneity of deposition, which minimizes areas where sparking may occur.
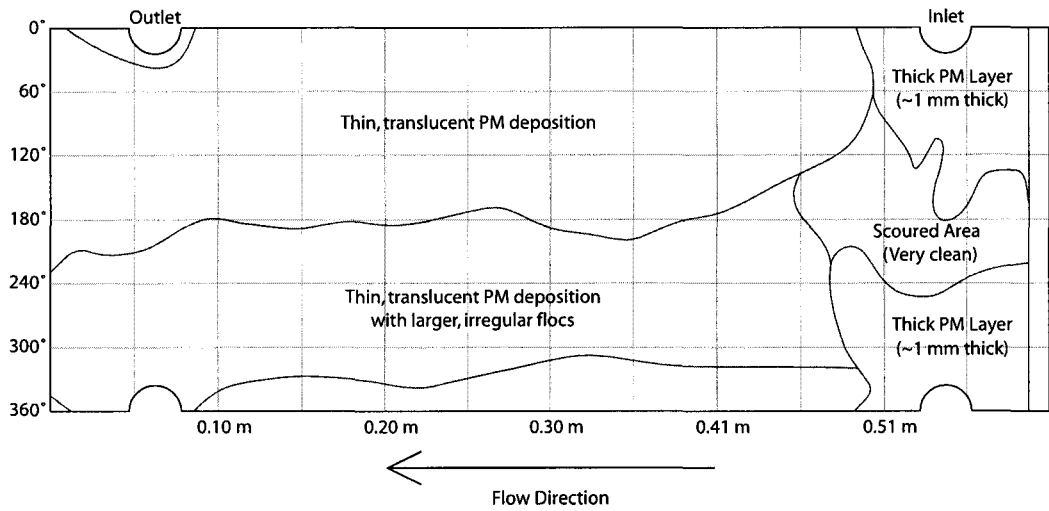
Figure D.2: Relative PM Deposition Inside ESP for 5 kg/hr exhaust flow rate.
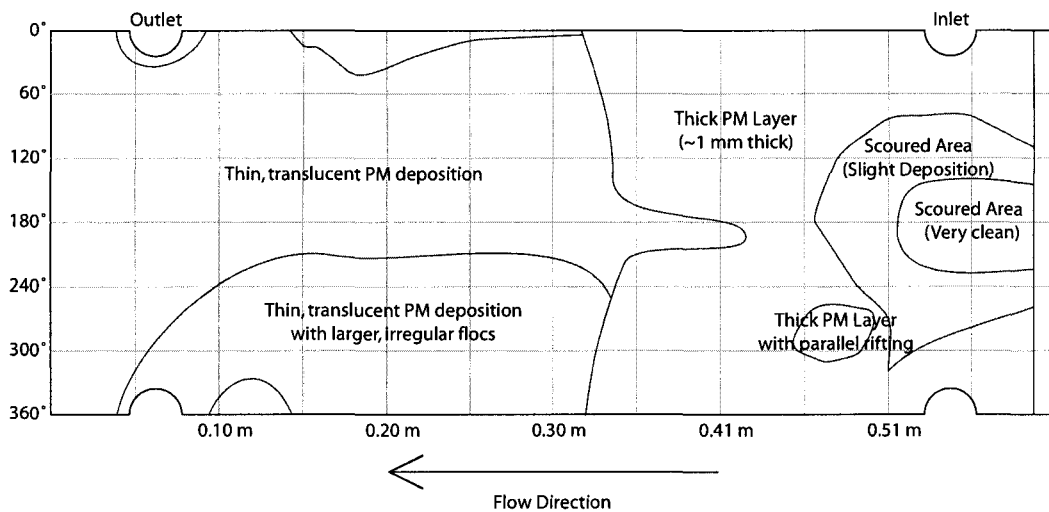

Figure D.3: Relative PM Deposition Inside ESP for 10 kg/hr exhaust flow rate.

120